MICROALGAL SWIMMING IN FLUID ENVIRONMENTS: EXPERIMENTAL AND NUMERICAL INVESTIGATIONS

A Dissertation
SUBMITTED TO THE FACULTY OF
UNIVERSITY OF MINNESOTA
BY

AHAMMED ANWAR CHENGALA

IN PARTIAL FULFILLMENT OF THE REQUIREMENTS
FOR THE DEGREE OF
DOCTOR OF PHILOSOPHY

Miki Hondzo
(Adviser)

October 2013

Acknowledgements

The research presented in this study wouldn't have been possible without the continued support and guidance of my advisor, Miki Hondzo. I would also like to equally thank Jian Sheng for his support and assistance with my thesis. Their genuine enthusiasm and passion for research is contagious and incredibly motivating. I am truly grateful for their confidence in me. Many thanks to Heinz Stefan, Vaughan Voller and Doug Mashek for taking their valuable time off of their schedule and agreeing to serve on my committee.

The assistance with laboratory experiments was made possible by the support of Jim Tucker, Chris Ellis, Mike Plante and Ben Erickson. I would also like to acknowledge the financial support and opportunity I received from the National Center for Earth Surface Dynamics and Minnesota Futures Grant, for which I am truly grateful.

Finally, I would like to thank all my good friends at SAFL. I cherished every bit of spending time at SAFL, my second home!

Dedication

Dedicated to my parents, C Abdulla and Dainabi, my sisters and my brother, Jaffer. And, a very special dedication to my dear wife, Ruhe !

Abstract

The objective of this research was to examine the effects of small-scale fluid motion on the kinetic behavior and some key physiological aspects of *Dunaliella primolecta* Butcher (*D. primolecta / Dunaliella*). *D. primolecta,* a fast growing microalga, is a promising organism for alternative energy production because of its capability to accumulate significant amount of “lipids”, a major prerequisite for commercial production of microalgal oil-derived biofuel. For kinetic response studies of *Dunaliella,* flow visualization and quantification techniques such as Particle Image Velocimetry (PIV) and Digital Holographic microscopy were employed. The two-dimensional PIV results showed that *Dunaliella* were influenced by the fluid flow as soon as the local (or ambient) flow velocities surrounding the cells exceeded the individual (flow subtracted) swimming velocity of *Dunaliella*. Further inspection of the swimming characteristics of *Dunaliella* under shear flow in a three-dimensional holography revealed that *Dunaliella* preferred to swim cross-stream (i.e. also the direction of local vorticity) when the shear flow exceeded a critical value, and this resulted in *Dunaliella* dispersing in a thin two-dimensional horizontal layer. The cell body rotation was absent during this display in shear flow, although the cell body rotation was evident while swimming in stagnant fluid. A physical model was developed that provided a possible explanation for the cell orienting and swimming in the cross-stream direction in a shear flow while cell body remained irrotational. The experimental swimming data also showed good agreement with the computational results. In order to investigate the biochemical composition and

some physiological aspects in *Dunaliella* under different flow conditions, a laboratory bioreactor equipped with speakers was utilized. The fluid flow velocities in the proximity of the cells generated by the speaker bioreactor are observable in natural water ecosystems. The results showed that the flow condition with the highest turbulence investigated favored the growth and lipid accumulation in *Dunaliella*.

Table of Contents

List of Tables

List of Figures

Chapter 1

1 Introduction

1.1 Significance of Research

The need for renewable energy resources is critical in this fast paced world with increasing population and expanding economy. The remaining global reserves of crude oil are continuously declining, with the possibility of running out in approximately 24 to 57 years based on the availability and usage of crude oil today (IEO 2008). It has been reported that the energy demand for transportation worldwide will increase by 45% by the year 2045 (Hirsch et al. 2005). In addition, the concentration of atmospheric CO_2 is continuously increasing which can significantly cause greenhouse gas-mediated climate change and global warming. Biofuels are a possible sustainable alternate solution to the diminishing fossil fuels. Biofuel production can help reduce the adverse effects of frequent oil supply crises, as well as develope long-term replacement for fossil fuels. There are many possible biofuel feedstock, for e.g., biodiesel (a chemically modified natural oil) obtained from soybean, rapeseed, oil palm and Jatropha, but biodiesel derived from microalgae holds great promise as a biofuel feedstock (Fig. 1.1) for producing a fuel that might one day be cost competitive with the petroleum fuels.

Microalgae as a biomass feedstock for biodiesel production have gained considerable recognition in providing positive environmental impacts. Microalgae biofuels are likely to have a much lower impact on the world's food supply than biofuels produced from conventional terrestrial plant crops. When compared with terrestrial plant produced biofuel, microalgal biofuel has a high caloric value, low viscosity and low density, high-lipid content; it can efficiently use CO_2 (responsible for more than 40% of the global carbon fixation), and is suitable in a variety of climates - properties that make microalgae more suitable for biofuel production (Miao et al. 2004).

Oil Source	Biomass (Mt/ha/yr)	Oil Content (% drymass)	Biodiesel (Mt/ha/yr)	Energy Content (boe/1000ha/day)
 Soya	1-2.5	20	0.2-0.5	3-8
 Rapeseed	3	40	1.2	22
 Palmoil	19	20	3.7	63
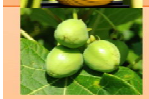 Jatropha	7.5-10	30-50	2.2-5.3	40-100
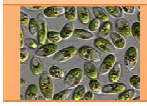 Microalgae	140-255	35-65	50-100	1150-2000

Mt = Metric tons; ha = hectare; boe = barrel of oil equivalents

Fig. 1.1. Comparison of terrestrial oilseed crops and microalgae derived oils for energy production.

1.2 Microalgae

Microalgae are microscopic photosynthetic organisms that are present in both marine and

freshwater environments. Microalgae are the most primitive form of plants. The mechanism of photosynthesis in microalgae is similar to that of higher plants, but they are generally more efficient converters of solar energy because of their simple cellular structure. In addition, because the cells grow in aqueous atmosphere, they have more efficient access to water, CO_2, and other nutrients. The petroleum fuels that drive today's global economy are actually ancient algae. After millions of years of heat and pressure, subterranean pockets of algae were concentrated into energy-rich liquids that could be extracted and processed into a variety of products. But, declining global supplies of oil and increasing concern about the climate-warming effects of fossil fuels are pushing society to look beyond these ancient algae for a sustainable, long-term source of fuel. Currently, microalgae are mostly produced for its high value by products such as natural pigments and health food product (Raja et al. 2008). Even though in the last few years there has been an increase in the number of algal biofuel based companies and production rate has increased, the algae-based fuels are currently too expensive to compete with fossil fuels. For applications such as biofuel production, the cost must be reduced by at least of order of magnitude.

1.3 Chronological Funding for Algae Research

In 1978, the US Department of Energy's (DoE) Office of Fuels Development created the Aquatic Species Program (ASP) to develop transportation fuels from algae with a $25 million grant for a period from 1978 to 1996. This represents the most comprehensive research effort to date on fuels from algae. ASP was successful in demonstrating the

feasibility of algal culture as a source of energy and made significant advances in the technology. These advances were made through strain isolation and characterization of algae, studies of algal physiology and biochemistry, genetic engineering, engineering and process development, and outdoor demonstration-scale algal mass culture (Pienkos and Darzins 2009). While ASP made significant progress over its 18-year existence, in 1996, the DoE shut down the program, concluding that algal biofuels could not compete with fossil fuels in cost. The potential cost of algal oil production was estimated in the $40–$60 per barrel range compared to $20 per barrel for crude oil in 1995 (Sheehan 1998). In the years immediately following ASP and until recently, support for algal biofuels research was rather limited, and as a result little progress was made. In the last few years, however, interest in algae has increased dramatically, and although federal agencies are beginning to show signs that increased support is imminent, many new groups have begun to explore this area in industrial, academic, and national laboratories, largely funded by private investors and industrial sources. Most noticeable among them is, ExxonMobil, which has invested $300 million in 2009 with an agreement with Synthetic Genomes, *"to develop strains which reproduce quickly, produce a high proportion of lipids and effectively withstand environmental and operational conditions."* The funding however was reinstated in 2013. The statement read that the original project did have some value: *"Over the nearly four years working together the companies gained considerable knowledge about the challenges in developing economical and scalable algae biofuels. SGI also made significant strides in understanding algae genetics, growth characteristics, and enhancements to algae to improve algal biomass and lipid*

productivities."

1.4 Algal Culturing Systems

Microalgal cultures can be grown in an open system (such as raceway ponds which can be natural or man-made) or closed system (photobioreactors) for the purpose of biofuel harvest and extraction, although, each of them has its own pros and cons. For raceway ponds, the major advantage is the manufacturing cost as it requires less capital equipment and technique that makes it easy to maintain and operate. The disadvantage comes in quality control, light limitation, biofouling, as well as factors such as evaporation and cross-contamination of cultures, which can drastically reduce the yield from algae. On the other hand, closed systems have better control over algal culture environment and hence relatively better yield, but have to compensate for the cost and complexity to operate.

1.5 Challenges

Large-scale production of biofuels from algae is untenable with existing technology, as it would require the use of too much water, energy, and fertilizer making the cost of production high. To improve matters, an assessment should be conducted of proposed technologies that examine sustainability at all stages of fuel production, including growing or collecting algae and harvesting their oil and converting it into fuels (Sheehan 1998). Some of the major biological, physical and chemical challenges include:

Biological Challenges:

1. **Land:** It will require large, mostly flat tracts of land near sustainable water resources

located in favorable climate conditions.

2. Water: Even though algae can thrive in salt and waste water, as well as fresh water, using large amounts of water for growing algae may be at odds with water needs of population centers, agriculture, and wildlife habitat. Evaporation alone can consume millions of gallons a day from moderately sized operations.

3. Nutrients: The availability and balance of nutrients (many of which are in diminishing supply) dramatically affect the types and productivity of algae populations.

4. Strain Selection: Identifying and maintaining the ideal composition of species in large-scale production of algae is needed to generate a consistent high quality product.

5. Temperature: Specific temperatures must be maintained for specific algal strains to thrive. Weather is inherently unpredictable requiring constant monitoring and expensive heating and cooling equipment to maintain consistent temperatures.

6. Predators and Parasites: Algae ecosystems are extremely vulnerable to invasive species and bacteria as it is nearly impossible to control the introduction of undesirable bacteria, algae strains, algae predators or other microbes that impact the cultivation of algae.

7. Toxins: Maintaining a clean, unpolluted environment is crucial for algal growth. Contamination from outside sources puts the ecosystem at risk of dramatic productivity losses.

Chemical Challenges

8. Extraction: Removing the oil and nutrients from harvested algae is a complex process. Many companies are searching for a “lipid trigger,” or a way to easily turn algae

into single-cellular oil factories. But altering the metabolisms of microorganisms is extremely intricate and is not a feasible approach to attaining the production levels of today's energy industry.

Physical Challenges

9. Pumping: The circulation of water and nutrients throughout the production system is crucial for maintaining algal growth and harvest rates, but it also requires enormous sums of energy and capital.

10. Harvesting: Removing algal biomass from the water culture in high concentrations is a difficult and costly process. Current technologies rely on energy intensive equipment, chemical flocculation, and other methods that can harm the algae and have extremely high operating costs. To economically harvest algae at scale, simpler and more efficient systems must be implemented.

11. Concentrating: Even though algae-laden water looks quite green, it is deceptively dilute. By weight, algae are approximately one part in 3,000. Typical concentrating techniques (microstrainer, centrifuge, filtration, etc.) can only bring this ratio down by an order of magnitude, and these processes are not economical or scalable.

1.6 Overview of Dissertation

Algae survive in aqueous environment and are mostly motile (i.e., able to swim). Despite micro-algae being motile, little distinction is made between the cells and the fluid. Furthermore, accumulation of cells within the fluid can induce hydrodynamic instabilities leading to patterns and flow, which may be of particular relevance to bioreactors. Thus, it

is advantageous to have a greater understanding of the swimming behavior of algae and the flows they generate. However, in order to understand the collective behavior, we need to investigate the hydrodynamics of individual cells.

This dissertation consists of four chapters that provide experimental methodologies and results on the effects of fluid motion on microalga, aimed at optimizing physical growth conditions of algae to maximize algal productivity.

In **Chapter 2**, the kinetic and kinematic response of *Dunaliella* to fluid motion was explored with a 2D PIV set-up. A PIV analysis was performed to obtain the velocities of fluid flows (i.e., fluid not containing cells) characterized by varying the Reynolds number. The experiments were repeated with fluid containing cells for the corresponding Reynolds numbers, and were analyzed using the Particle Tracking Velocimetry (PTV). In order to obtain the average velocities of individual *Dunaliella* cells, the velocities of fluid were subtracted from the velocities of cells with fluid. This chapter gives information regarding cell behavior in flow (i.e., *are they always at the mercy of the flow* ?) and also gave an estimation of the cell swimming velocity in the presence and absence of fluid flow.

In **Chapter 3**, the composition of some key biochemical compounds (e.g. lipids) and physiological (e.g. growth) aspects in *Dunaliella* were measured under stagnant and varying fluid flow conditions. A laboratory scale bioreactor equipped with underwater speakers and fluorescent lights were employed for this study. The flow conditions in the bioreactor were controlled by varying the amplitude and frequency of sound signals of the underwater speakers. The experiments were performed for 15 days in total, in which

the first seven days were considered as the acclimatizing period and the sampling was obtained during the last 8 days. The pH and oxygen concentration of the culture during the experiments were also recorded.

In **Chapter 4**, the swimming strategies of *Dunaliella* in different shear rates were examined using a 3D holographic PIV set-up. The velocities of the cells in three dimensions were obtained. The dispersion of the cells in different shear was also estimated. The migration of active cells was compared with the passive (or dead) cells. A new microscopic channel was also designed to investigate the presence of cell body rotation in cells during swimming in stagnant as well as shear flows.

In **Chapter 5**, a physical model was developed based on the flagella kinetics that proposed a possible mechanism for the swimming pattern observed in chapter 4. An equation predicting the minimum beating frequency for *Dunaliella* to remain irrotational in a shear flow is also proposed. The experimental swimming data including, flagella beating frequency, flagella forces and torques in flow obtained from 3D digital holography were compared with the numerical results. The flow characteristics around the beating flagella while swimming in a stagnant flow are also demonstrated.

In addition to understanding the swimming characteristics of individual cells, the major contribution of this research has been to propose that by changing the physical flow conditions around the cell, the productivity from the cells can be manipulated. The suggested flow conditions can be maintained while culturing cells for the application of cells for biofuel and human nutrition production. The research also proposed a possible mechanism for thin layer formation in oceans as well as a technique to separate live cells

from dead cells in an engineered environment. It is important to note that different strains from a same species could give different results and may need to be studied separately.

Chapter 2

Kinetic Responses of *Dunaliella* in Moving Fluids

Published as: Chengala, A. A., M. Hondzo, D. Troolin, and P. A. Lefebvre. 2010. Kinetic responses of *Dunaliella* in moving fluids. Biotechnol. Bioeng. **107**:65–75, doi: 10.1002/bit.22774.

The objective of this work was to quantify the kinetic behavior of *Dunaliella primolecta* (*D. primolecta*) subjected to controlled fluid flow under laboratory conditions. *In situ* velocities of *D. primolecta* were quantified by micron-resolution particle image velocimetry and particle tracking velocimetry. Experiments were performed under a range of velocity gradients and corresponding energy dissipation levels at microscopic scales similar to the energy dissipation levels of natural aquatic ecosystems. An average velocity of *D. primolecta* in a stagnant fluid was 41 µm/s without a preferential flow direction. In a moving fluid, the population-mean velocities of *D. primolecta* follow a log-normal distribution. The variability of longitudinal velocities was maximal at the highest fluid flow velocity in the channel. Local fluid velocity gradients inhibited the accrual of *D. primolecta* by two fold five days after the initiation of the experiment in comparison to the non-moving fluid control experiment.

2.1 Introduction

Dunaliella is a motile, bi-flagellated, cell-wall-less, unicellular green algae (belonging to the class of Chlorophyceae) whose cell size ranges from 9 to 17µm. *Dunaliella* thrive in media containing extremely wide range of salt concentrations ranging from 0.1 M to 5 M NaCl (Avron 1992), and if grown under proper conditions, *Dunaliella* can accumulate appreciable amount of cartenoids (β-carotene) (Ben-Amotz et al. 1991; Schlipalius 1991), glycerol (Ben-Amotz and Avron 1982; Thakur and Kumar 1998) and lipids (Tornabene et al. 1980; Vanitha et al. 2007). *Dunaliella* is relatively easy to continuously culture in a laboratory and have higher resistance to various environmental conditions compared to other species of algae (Aizawa and Miyachi 1992). According to Ben-Amotz et al., (1991), *Dunaliella* strains are probably the most successful microalgae in mass cultivation, mainly due to their ability to survive in high saline environments characterized by extreme range of ecological adaptability (low temperatures, low pH, high irradiance etc.), which reduces the number of competitors and predators. *Dunaliella* contain lipids and fatty acids as membrane components, storage products, metabolites and sources of energy.

Dunaliella has been found to be one of the richest natural sources of β-carotene (Zhu and Jiang 2008; Raja et al. 2007; Hejazi and Wijffels 2003). Under suitable conditions, *Dunaliella* can accumulate up to 10% of the dry cell weight of β-carotene (Loeblich 1974; Jin and Melis 2003). β-carotene is an orange pigment, which has a wide range of applications in pharmaceutical industry, food, cosmetic, and as a coloring agent. *Dunaliella* contain 9-cis-β-carotene, which is up to ten times stronger at preventing

cancer than ordinary β-carotene (Hieber et al. 2000). Production of β-carotene from natural sources has been of growing concern due to its increasing demand commercially (Lamers et al. 2008). Another major bi-product from *Dunaliella* harvest is glycerol (Thakur et al. 2000; Mishra et al. 2008). Glycerol is a colorless, viscous organic chemical widely used as a feedstock for the production of various chemicals and has found a wide range of applications in the pharmaceutical, medical, cosmetic, leather and textile industries. More than 50% of the dry weight of *Dunaliella* may be glycerol depending on the salt concentrations in the growth medium (Ben-Amotz et al. 1982). Glycerol and β-carotene are the major products of *Dunaliella* suitable for commercial utilization. The commercial cultivation of *Dunaliella* for the production of β-carotene and glycerol throughout the world is now one of the success stories of halophile biotechnology (Ben-Amotz 1980; Borowitzka and Borowitzka 1984), although it is economically less feasible due to the lack of advancement in biotechnological operations (Agarwal, 1990; Hadi et al. 2008).

An increasing demand for an alternative source of fuel for the ever depleting petroleum based fuels has been a widely discussed topic around the globe. It has been reported that the energy demand for transportation worldwide will double by the year 2020 (EIO 1999). Biodiesel obtained from natural sources is a very good alternative for petroleum-based fuels since it is highly bio-degradable, renewable, non-toxic (particulate emissions are low) and carbon neutral. Algal species of *Dunaliella* have been found to have a promising economic potential to produce biodiesel from micro-algae (Gouveia and Oliveria 2009). *D. primolecta* is one of the leading candidates in this endeavor

because of its ability to produce lipids (triglycerides) that are suitable for direct use as an oil feedstock for the production of biodiesel. *D. primolecta* has been reported to have a lipid content of about 23% of its total body weight (Chisti 2007) which makes it very promising for the biodiesel extraction.

The concept of using microalgae for sustainable feedstock production will be beneficial to the society if we are capable of culturing specific algae at large scales. Open ponds with mechanical mixing devices have been the major aquatic system explored for mass culture of microalgae. While the adaptive responses of *Dunaliella* to a variety of environmental conditions including temperature, light, salinity, and nutrient concentrations (Chen and Jiang 2009; Haghjou et al. 2009) have been reported, the kinetic responses of *Dunaliella* to fluid flow has not been investigated. In this study we report the kinetic behavior of *Dunaliella* at the cell scale under a variety of fluid flow conditions. Laboratory measurements were conducted under fluid flow energy dissipation levels reported in shallow lakes, wetlands, and ponds.

2.2 Materials and Methods

2.2.1 Culture Preparation

Strains of *D. primolecta* were obtained from UTEX, the culture collection of algae (University of Texas at Austin, USA), and were grown using the Erdschreiber's medium (Tompkins et al. 1995). Culture was maintained at room temperature under cool white fluorescent light on a C1 platform shaker (New Brunswick Scientific Co., INC, NJ, USA) for a period of 14 days during which *D. primolecta* grow to its full size (~11 μm).

Alternatively, *D. primolecta*, being a good swimmer, culture can be grown without the shaker by mixing them occasionally (twice a day) by hand. After 14 days, a small amount (5 mL) was taken to be used for the experiment.

2.2.2 Experimental Set-up

A micro-particle image velocimetry (micro-PIV) system developed by TSI Inc. (Shoreview, MN, USA) was used for the velocity quantification of *D. primolecta* cells and fluid flow in the experimental channel. The setup consists of an inverted microscope equipped with an epi-fluorescence filter cube, a double frame CCD camera (PIVCAM 14-10), a light-guide, a light source (Pulsed Nd:YAG laser and halogen lamp are used here), and a syringe pump (NE-500 model, New Era Pump Systems, Inc., NY, USA) (Fig. 2.1). A light source illuminates the particles in the flow channel and is imaged through the microscopic objective onto the CCD camera. An optical filter cube consists of a dichromatic mirror and an emission filter and is used to separate the scattered fluorescent light from the illumination light. The dichromatic mirror has a coating that transmits the fluorescent emission wavelengths and reflects the laser wavelength. The working principle consists of illuminating particles in the flow using the light source. The measurement plane is defined by the depth of focus of the microscope objective; in-focus particles are measured and out-of-focus particles with a weak signal are not. Image pairs are captured using the camera separated by a short time interval. The average displacement of a group of particles is mapped by correlation (cross-correlation) of two consecutive images and is processed with analyzing software to obtain the velocity vector map.

The fluid flow channel was placed on the universal stage holder of the microscope. Fluorescent particles were used to seed the flow for the fluid flow analysis. Cultured *D. primolecta* were used as seeding particles for algal analysis. For the non-moving fluid experiment, i.e., stagnant flow, no fluid flow was passed through the syringe pump thereby allowing *D. primolecta* cells to move freely and independently. For moving fluid flow measurements, different flow rates were supplied through the computer-controlled syringe pump. The flow rates were chosen based on the fractions of swimming velocity of *D. primolecta* in stagnant fluid (e.g. 12.5%, 25% etc. of the velocity). The seeded flow images were captured using a 10× objective and algal flow images were captured using a 4× objective of the microscope using the double frame CCD camera with 1376 × 1024 pixel resolution. The field of view for seeded flow was 1.43 mm in the streamwise direction and 1.06 mm in the spanwise direction. For algal flow it was 0.42 mm in the streamwise direction and 0.4 mm in the spanwise direction. A set of 250 double frame image pairs were recorded for both the algal and seeded flow with different flow rates with the timing between each frame (ΔT) adjusted to have a particle displacement of approximately 8 to 10 pixels. Typical value of ΔT for stagnant algal flow was 0.5s and for moving flows (seeded and algal) it varied from 0.15s to 0.55s depending on the flow rate. The recorded images were analyzed using the micro-PIV for fluid flow and Particle Tracking Velocimetry (PTV) for algal flow. For seeded flow, fluorescent particles appeared as white spots on a dark background while for the algal flow, *D. primolecta* cells appeared as dark spots on a bright background. Fig. 2.2A shows a single frame image of *D. primolecta* cells in a stagnant fluid. Sets of three experimental runs were

repeated for each flow rate under identical experimental conditions. Under identical flow rate, no appreciable difference in mean velocities was observed. An independent set of experiments was also conducted by using a halogen lamp as a light source in the flow channel instead of the pulsing laser. The results demonstrated 1% to 2% difference in the velocities of *Dunaliella*. For each experiment, fresh culture of *Dunaliella* was transferred in the experimental channel. *Dunaliella* cells were never exposed longer than 60 seconds to the laser light in the channel for each independent experiment.

2.2.3 Seeding Particles

Fluid in the experimental channel was seeded with 1 µm diameter red dye-impregnated PSL (Polystyrene Latex) fluorescent particles (density of 1.05 g/cc) obtained from TSI (Shoreview, MN) and manufactured by Duke Scientific Corporation, USA. The peak excitation wavelength of the seeding particles is 542 nm and the emission peak is 612 nm. Distilled water mixed with the suspended fluorescent particle solution in the ratio of 10:1 was used as the working fluid. The velocity of the fluorescent seeding particles obtained through micro-PIV was taken as a reference velocity which was subtracted from the observed *Dunaliella* velocities. The net velocities of *Dunaliella* were acquired by PTV in which the fluid was not seeded by fluorescent particles, but rather, the individual cells of *Dunaliella* were visualized as the tracer particles. The *Dunaliella* do not fluoresce, so a fluorescent background was used to image the particles as dark spots on a bright background.

2.2.4 Flow Channel

Fluid flow channel was fabricated using PDMS (polydimethylsiloxane) having a rectangular cross-section with a depth of 0.45 mm and a width of 3.5 mm (Fig. 2.1). The length of the channel approximately measured 35 mm. The fluid in the channel was directed from the inlet of the channel using the syringe pump. The computer-controlled pump enable repeatability of experiments with algae and without algae at a specified fluid flow in the channel. All the measurements were taken at a vertical distance of $1/4^{th}$ the channel depth from the channel bed (~0.1 mm) and middle half of the channel (to avoid wall effects on *Dunaliella* swimming) close to the outlet of the channel after the flow was developed in the channel.

2.2.5 PIV versus PTV Analysis

Instantaneous velocity measurements are obtained for micron scale fluidic devices using micro-PIV analysis (e.g. Santiago et al. 1998; Meinhart et al. 1999). PTV analysis on the other hand, tracks the individual particles in the flow for obtaining instantaneous velocities. The main difference between micro-PIV and PTV analyses lies in the fact that the velocity obtained using micro-PIV is the velocity of all the particles averaged over an interrogation window (an image is broken down into a number of tiles called interrogation windows) where as the velocity obtained using PTV is the velocity of each individual particle in an interrogation window. The density of seeded particles is easily controllable in the interrogation window and hence fluid flow analysis was conducted by micro-PIV. PTV analysis was applied for algal velocity measurements for two reasons: the number density of algae was relatively low, and algae movements are independent, meaning that two algae next to each other can, and often do, move in completely different

directions. Since micro-PIV and PTV generate advective velocity for the fluid flow under observation, the net *Dunaliella* velocity at a specified fluid flow, for varying flow rates (moving flows) were obtained by subtracting the seeded velocity at the corresponding flow rate.

2.2.6 Fluid Flow Analysis

The velocity vectors of fluid flow and algae were obtained using Insight3G software (TSI Inc, Shoreview MN). For fluorescent seeded flow, images were processed using 64×64 pixel interrogation window with a recursive Nyquist grid algorithm, fast Fourier transform (FFT) correlator and bi-linear peak engine. Post-processing was done to remove and replace bad vectors which accounted for less than 5% of the resultant velocity vectors. This micro-PIV analysis was done for all flow rates to obtain seeded fluid flow velocities. For algal flow, all the image intensities were inverted to convert dark spots (*D. primolecta* cells appear as dark spots, Fig. 2.2A) to bright spots. A minimum intensity image was created by scanning each image in the set and obtaining the minimum pixel intensity at every location. This minimum intensity image was then subtracted from every image in the sequence, accentuating the particle images and diminishing the effect of constant sources of illumination such as background intensity, out of focus particles, and noise. This procedure was performed independently for the first and second frames to account for slight differences in the laser illumination. The subtracted images were used for PTV analysis. PTV involves selecting several parameters, namely, the maximum particle displacement between image frame based on *Dunaliella* movement, the intensity threshold value to determine the particles of interest

(this helps to remove some speckles that still remain after background subtraction), the maximum size difference of a tracked particle from one frame to the next, and the minimum and maximum particle size. All the numbers provided for the above descriptions were chosen based on the particular run (flow rate) which varied for different flow rates. The analysis was done for all flow rates to obtain observed *Dunaliella* velocities. For all the flow rates where *Dunaliella* had control over the flow, the observed *Dunaliella* velocities were higher than the seeded flow velocities for the corresponding flow rate. Net *Dunaliella* velocities were obtained by subtracting the seeded velocities from the observed *Dunaliella* velocities.

2.2.7 Flow Measurements

The seeded fluid flow velocities (Fig. 2.3A) and *Dunaliella* (algal) velocities (Fig. 2.3B and Fig. 2.3C) in the x-y plane were obtained from the instantaneous velocity vector maps using micro-PIV and PTV analysis, respectively. For algal flow analysis (Fig. 2.2A), the longitudinal components of velocity include (a) observed *Dunaliella* moving in the x-direction of flow (u^{+}_{obs}), and (b) observed *Dunaliella* moving opposite to the x-direction of flow (u^{-}_{obs}). The perpendicular components of velocity include (a) observed *Dunaliella* moving perpendicular the flow in the positive y-direction (v^{+}_{obs}), and (b) observed *Dunaliella* moving perpendicular to the flow in the negative y-direction (v^{-}_{obs}). For seeded flow analysis, the velocity component includes the longitudinal component of velocity in the flow direction or seeded fluid flow velocity (u_s) and the perpendicular component of velocities was zero since the fluid flow was unidirectional driven by the

syringe pump. The net velocity of *Dunaliella* cells in the longitudinal (x-flow) direction is denoted by u_D and the net velocity of *Dunaliella* cells in the perpendicular (y) direction is denoted by v_D. The value of u_D refers to the positive and negative velocities of *Dunaliella* as cells could move in both (+x and –x) directions. Similarly, The value of v_D refers to the positive and negative velocities of *Dunaliella* as cells could move in both (+y and –y) directions.

The net velocities of *Dunaliella* in the positive x-flow direction (u_D^+) were calculated for all flow rates as

$$u_D^+ = u_{obs}^+ - u_S \tag{1}$$

and the net velocities of *Dunaliella* opposite (negative) to x-flow direction (u_D^-) were calculated for all flow rates as

$$u_D^- = u_{obs}^- \tag{2}$$

Since the seeded flow was uni-directional (only in the positive x-flow direction), the net velocities of *Dunaliella* perpendicular to the flow in the positive y-direction of flow (v_D^+) was calculated for all flow rates as

$$v_D^+ = v_{obs}^+ \tag{3}$$

and the net velocities of *Dunaliella* perpendicular to the flow in the negative y-direction of flow (v_D^-) was calculated for all flow rates as

$$v_D^- = v_{obs}^- \tag{4}$$

Different fluid flow rates (Q) that were pumped through the experimental channel were used to calculate the Reynolds number

$$\mathrm{Re} = \frac{uL}{\nu} \tag{5}$$

where ν is the kinematic viscosity of water (=10^{-6} m^2/s), $u = \frac{Q}{A_c}$ is the cross-sectionally averaged fluid flow velocity or discharge velocity in the channel, $L = 4\frac{A_c}{P_w}$ is the characteristic length, A_c is the channel cross-sectional area perpendicular to the discharge velocity, and P_w is the channel wetted perimeter. The Reynolds number is dimensionless and represents the ratio of inertial and viscous forces in a fluid flow. The energy dissipation rates, □ (x, y) were calculated based on the following equation (Luznik et al. 2007).

$$\varepsilon(x,y) = 4\nu\left[\left(\frac{\partial u}{\partial x}\right)^2 + \left(\frac{\partial v}{\partial y}\right)^2 + \frac{3}{4}\left(\frac{\partial u}{\partial y}\right)^2 + \frac{3}{4}\left(\frac{\partial v}{\partial x}\right)^2 + \frac{\partial u}{\partial x}\frac{\partial v}{\partial y} + \frac{3}{2}\left(\frac{\partial u}{\partial y}\frac{\partial v}{\partial x}\right)\right] \tag{6}$$

2.3 Results

All experiments (PIV and PTV) showing the swimming velocities of *Dunaliella* at different fluid flow conditions are summarized in Table 2.1. The Reynolds number in the channel ranged from Re = 0 in a stagnant (non-moving) fluid to Re = 84.4×10^{-3}. Since Re<<1, fluid flow in the channel was dominated by viscous forces. The seeded fluid flow velocities (u_s) increased with the Reynolds number in the channel. All the rest of velocities with subscript “obs” refer to the observed *Dunaliella* velocities in the

experimental channel. The net velocity of *Dunaliella* in the positive x-flow direction i.e. the observed velocity minus the seeded fluid flow velocity in the flow direction is denoted by u_D^+. The fluid flow energy dissipation rate (ε) over the channel cross-sectional area ranged from 10^{-8} to 10^{-5} m^2/s^3. This dissipation range is customarily reported in shallow lakes, ponds, and streams.

2.3.1 Seeded Flow

The fluid flow rates for the experiment were varied from zero (stagnant) to 16.7×10^{-11} m^3/s. The vector plot of seeded velocity at the highest Reynolds number, Re = 84.4×10^{-3} in the x-y plane is shown in Fig. 2.3A. The plot depicts a unidirectional flow i.e., the velocity in the y-direction is minimal and hence can be neglected. The velocity that is observed at all points in the field of view of the image is almost equal to the mean velocity. Fluid flow close to the channel boundaries was not considered. The mean velocity in the field of view of Fig. 2.3A was taken as the reference seeded velocity and was used to obtain the net velocity of *Dunaliella* in the positive x-direction.

2.3.2 Algal Size and Kinetics

The average size of *D. primolecta* cells observed in the experiment was approximately 11µm for both stagnant as well as moving fluid flow conditions. Fig. 2.2B shows the histogram plot of the diameter of *D. primolecta* cells observed in the stagnant flow. The total number of *D. primolecta* cells observed in the stagnant flow for 250 double frames is around 47000 and these numbers reduced with the increasing fluid flow rate. At the highest Re=84.4×10^{-3}, the total number of *D. primolecta* cells observed for 250 double

frames is around 27000. The swimming average velocity of *Dunaliella* in the flow direction at stagnant condition was observed to be u_D^+ = 41.84 µm/s and opposite to the flow direction, it was u_D^- = 39.23 µm/s (Table 2.1). This shows that on average the *D. primolecta* cells swim approximately 4 times its body length per second in a stagnant fluid. Fig. 2.3B shows the vector plot of the swimming direction of *D. primolecta* cells in a stagnant fluid, Re = 0, and Fig. 2.3C shows the vector plot of swimming direction in a moving fluid at Re = 84.4×10^{-3}. While in a stagnant fluid *D. primolecta* cells move in all directions, in the moving fluid the velocity vectors of *D. primolecta* are mostly aligned in the main fluid flow direction through the channel.

The observed velocity of *D. primolecta* in the positive x-flow direction (u_{obs}^+) normalized with stagnant velocity (u_{stag}) when plotted against Re depicts a constant value ($\frac{u_{obs}^+}{u_{stag}} = 1.1$) for $15\times10^{-3} \geq$ Re ≥ 0 (Fig. 2.4). In this range of Re, *D. primolecta* cells have a control over the fluid flow in the channel. At Re > 15×10^{-3}, *D. primolecta* cells do not have control over the fluid flow and the cells are forced to move in the direction of fluid flow in the channel. A linear increase in the velocity ratio ($\frac{u_{obs}^+}{u_{stag}} = 77\,\mathrm{Re} - 0.05$) is observed for Re > 15×10^{-3}. This result shows that the fluid flow does influence the swimming velocity of *D. primolecta* as it transports *D. primolecta* along the main fluid flow direction.

2.3.3 Scatter Plots

The scatter plot of observed *D. primolecta* cells in the longitudinal direction of flow and observed *D. primolecta* cells in the perpendicular direction to the flow is depicted in Fig. 2.5. It is clearly evident that at Re = 0 (stagnant), *D. primolecta* cells swim in all directions with almost equal velocity depicting a circular shape around the center of mass (0-0). With increase in the Re number the center of mass is swept in the flow direction (e.g. 250-0 at Re = 84.4×10^{-3}). Another interesting observation is the fact that net *D. primolecta* velocities are scattered all over the field of view in the micro-flow channel (around 0-0) at all Re values irrespective of the driving fluid flow velocity (Fig. 2.6) even though at higher Re the net *D. primolecta* cells swim slower than stagnant condition (Re = 0). The scattering in all directions is also evident from the vector plot in Fig. 2.3B, where even though at Re = 84.4×10^{-3} the vector is dominant in the flow direction, there is a comparatively small velocity in the perpendicular direction of flow as well indicating that *D. primolecta* was able to swim away from the prevailing flow direction.

2.3.4 Histogram Plots

Histogram plot of the velocity of net *D. primolecta* cells for the whole population in the x-direction (u_D) for all the flow rates depict a symmetric deviation around the center of mass (Fig. 2.7). The default null hypothesis that the *Dunaliella* velocities originate from a distribution in the normal family was successfully tested at the 5% significance level by using the Matlab software (The MathWorks, Inc., R2008b). The first statistical moments, μ_{u_D}, of normal probability distributions of u_D were plotted versus corresponding Reynolds numbers in Fig. 2.8. The population mean velocities follow a log-normal

distribution with R^2=0.95. Reynolds number at the maximum mean velocity ratio, $\frac{|\mu_{u_D}|}{\mu_{u_{stag}}} = 1 + \frac{a}{\sqrt{2\pi}\, S\, Re} \exp\left\{ -\ln\left(\frac{\left(\frac{Re}{Re_c}\right)^2}{2S^2} \right) \right\}$ was $Re_c=13\times10^{-3}$. This result indicates that fluid flow conditions in the proximity of *D. primolecta* cells mediate mean population velocity in the approximate range of $16\times10^{-3} > Re > 5\times10^{-3}$. Outside of this range, *D. primolecta* velocities were not systematically affected by moving fluid. The second statistical moments, σ_{u_D}, were plotted versus Reynolds number in Fig. 2.9. The plot depicts that the σ_{u_D} decreases in the range of $15x10^{-3} \geq Re \geq 0$ with a minimum close to σ_{u_D} ~30 µm/s at $Re = 15\times10^{-3}$. At $84\times10^{-3} > Re > 15\times10^{-3}$, σ_{u_D} increases up to 80 µm/s at the highest Re. The values of σ_{u_D} are typical for the reported *in situ* velocity measurements of microorganisms (Sheng et al., 2007). The results demonstrate a significant effect of local fluid flow velocities on the variability of *D. primolecta* velocities.

2.4 Discussion

Under field conditions algal cells could be subjected to a variety of fluid motions starting with the large scale eddies, usually determined by the geometry of aquatic environment e.g. water depth, down to smallest eddies on the order of a millimeter where as the kinetic energy is converted into heat by the action of molecular viscosity (Hondzo and Wüest 2009). Our results demonstrate that the kinetics of *Dunaliella* cells is controlled by fluid flow as soon as the fluid flow exceeds the velocity of *Dunaliella* in a stagnant fluid ($u_D \approx$ 40 µm/s). This implies that *Dunaliella* cells will be imbedded in the large range of eddies

that will transport *Dunaliella* cells through a variety of nutrient concentrations and associated photosynthetically active radiation levels in aquatic environments. At the scale of individual *Dunaliella* cell (about 10 µm), the cell is exposed to a velocity gradient that is the ultimate consequence of large scale eddies in aquatic ecosystems. The velocity gradients at the cell scale are determined by energy dissipation level. We employed micro-PIV to systematically change the velocity gradients in the proximity of *Dunaliella* cells. The velocity gradients generated in the channel resulted in the energy dissipation range from $\varepsilon = 10^{-8}$ m^2/s^3 to $\varepsilon = 10^{-5}$ m^2/s^3 (Table 2.1). These energy dissipation rates are commonly observed in the surface layers of shallow lakes and ponds in aquatic ecosystems (Hondzo and Warnaars 2008). This implies that our laboratory measurements should be scalable or transferable to field conditions.

Our experiments demonstrate that small-scale velocity gradients modulate kinematic responses of a motile and bi-flagellated green alga. To what extent the small scale velocity gradients modulate the physiological responses of *Dunaliella* is unknown. In order to facilitate the question, we conducted a preliminary experiment in a 35 L bioreactor with controllable small scale velocity gradients (Warnaars et al. 2006). Two independent experiments under identical nutrients, temperature, and light conditions were conducted under stagnant fluid (Re=0 in this study) and in a moving fluid with $\varepsilon \approx 10^{-7}$ m^2/s^3 ($Re \approx 23.6\times10^{-3}$ in this study). A two fold increase in *D. primolecta* number and chlorophyll-a concentrations were observed in a stagnant fluid in comparison to the moving fluid at day 5 after the initiation of experiment (Fig. 2.10). While small scale velocity gradients facilitate the accrual of unicellular non-motile green algae *Selenastrum*

capricornutum (e.g. Warnaars and Hondzo 2006), the accrual of *D. primolecta* was inhibited by the moving fluid. In order to provide algal cells photosynthetically active radiation in bioreactors, mechanical mixers are often employed. The induced velocity gradients by the mixers will influence the kinetic responses of *Dunaliella* and very likely may have an effect on algal physiology. The experiments reported in this study could be instrumental in the design of efficient bioreactors for the harvest of *Dunaliella*.

Table 2.1. The observed and net *D. primolecta* velocities in longitudinal (x-flow) and perpendicular (y) directions in stagnant (Re = 0) and moving fluids (Re > 0). Note that, $u^{-}_{obs} = u^{-}_{D}, v^{+}_{obs} = v^{+}_{D}, v^{-}_{obs} = v^{-}_{D}$, $u^{+}_{D} = u^{+}_{obs} - u_S$, μ_{u_D} and σ_{u_D} are the statistical moments of normal probability distribution. | | designate an absolute value.

Flow rate	Reynolds number	Energy diss.	Seeded velocity	Obs. vel. +x dir.	Obs. vel. -x dir.	Obs. vel. +y dir.	Obs. vel. –y dir.	Net *Dunaliella* vel. + x dir.	Population statistical moments in x dir.
Q	Re	ε	u_s	u^{+}_{obs}	u^{-}_{obs}	v^{+}_{obs}	v^{-}_{obs}	u^{+}_{D}	$\lvert\mu_{u_D}\rvert \pm \sigma_{u_D}$
(10^{-11})	(10^{-3})	(10^{-8})							
(m^3/s)	(-)	(m^2/s^3)	(µm/s)	(µm/s)	(µm/s)	(µm/s)	(µm/s)	(µm/s)	(µm/s)
stag	0.00	0.00	0.00	41.84	39.23	36.29	35.61	41.84	2.72±52.8
0.5	2.53	1.23	4.63	41.98	36.15	32.18	32.76	37.35	1.20±48.2
0.83	4.22	3.43	11.26	42.24	34.59	28.58	28.8	32.39	2.20±43.2
1.34	6.75	8.77	16.39	42.76	33.10	31.16	31.57	26.37	6.73±44.9
1.67	8.44	13.7	20.60	43.08	32.59	25.81	25.47	22.49	8.44±42.2
1.84	9.28	16.6	24.01	43.93	30.21	24.27	25.79	19.92	10.29±35.2
2.00	10.13	19.7	27.07	44.96	31.81	28.24	28.17	17.89	12.66±38.4
2.17	10.97	23.2	29.22	42.40	26.91	20.96	20.63	13.18	15.08±31.8
2.34	11.82	26.9	35.16	48.02	33.12	30.63	30.64	12.86	15.86±39.7
2.50	12.66	30.8	36.52	47.50	25.66	21.94	22.15	10.98	15.98±33.4
2.67	13.5	35.1	37.23	50.69	35.73	33.35	32.99	13.45	16.62±40.6
2.84	14.35	39.6	43.55	49.34	27.74	18.08	18.20	5.79	13.99±28.1
3.01	15.19	44.4	47.68	50.33	33.91	33.84	33.28	2.65	11.11±44.3
3.17	16.04	54.3	52.90	56.41	29.82	29.67	29.81	3.51	8.82±33.1
3.34	16.88	60.2	53.62	55.20	31.99	38.40	37.06	1.58	6.66±41.4
4.68	23.63	107	67.38	60.84	31.02	37.28	34.93	0.00	3.73±44.9
5.84	29.54	168	89.97	87.14	39.97	29.12	29.69	0.00	1.19±53.1
8.35	42.2	343	134.42	136.68	26.61	37.34	34.01	2.26	2.05±68.7
11.7	59.08	672	184.39	187.86	27.52	34.00	38.27	1.47	2.13±62.4
16.7	84.4	1370	276.36	273.94	53.53	43.46	35.65	0.00	3.87±81.9

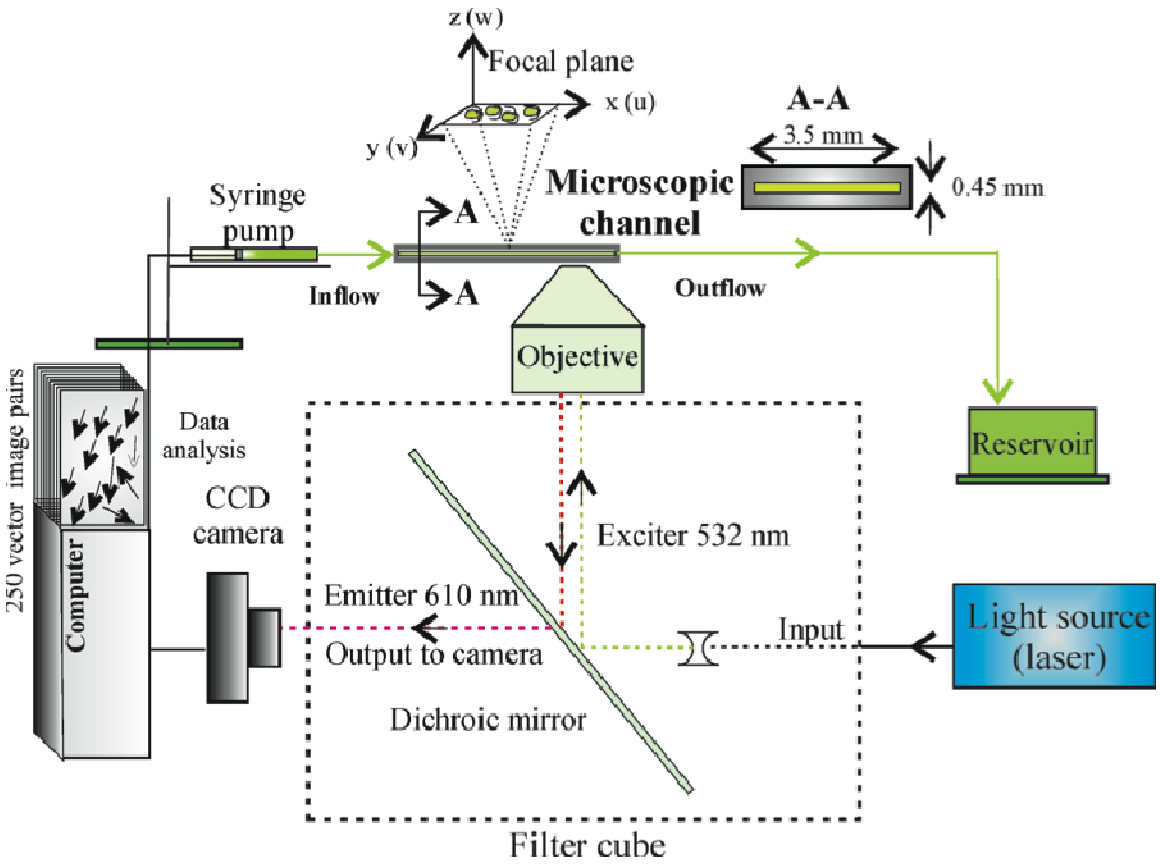

Fig. 2.1. Schematic diagram illustrating the micro-PIV setup.

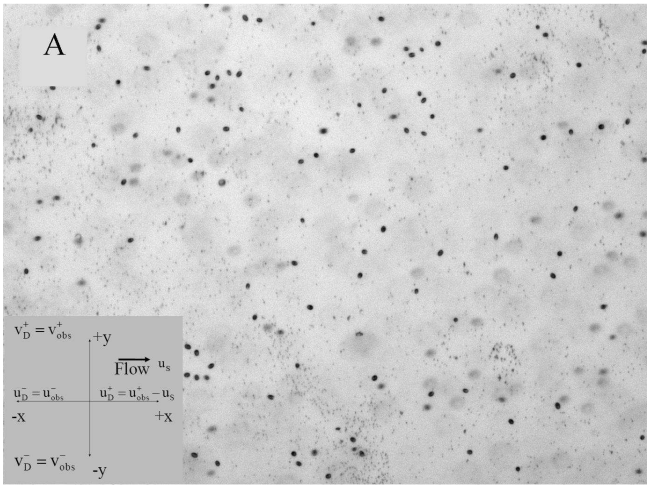

Fig. 2.2. A**:** Shows a single frame image of *D. primolecta* cells in the micro-channel in the stagnant flow condition captured using 4× objective of the microscope. *D. primolecta* cells appear as dark spots against a bright background. The field of view of the capture is 1.45 mm × 1.06 mm and B**:** Shows the histogram plot showing the diameter of *D. primolecta* cells observed in the stagnant flow. An average cell diameter of about 11 µm was observed.

Fig. 2.3. A: Vector plot of fluorescent particles observed at low flow (Re = 8.44×10^{-3}) captured at 10× objective. The field of view is 0.42 mm × 0.4 mm. B: Observed vector plots of *D. primolecta* velocities in stagnant flow condition (Re = 0) and C: in moving fluid (Re = 84.4×10^{-3}) captured using 4× objective of microscope. The field of view is 1.43 mm × 1.06 mm. In the stagnant fluid (B), *D. primolecta* depicted non-preferential velocity direction and the moving fluid (C) was mainly aligned with the stream-wise (downward) fluid flow direction.

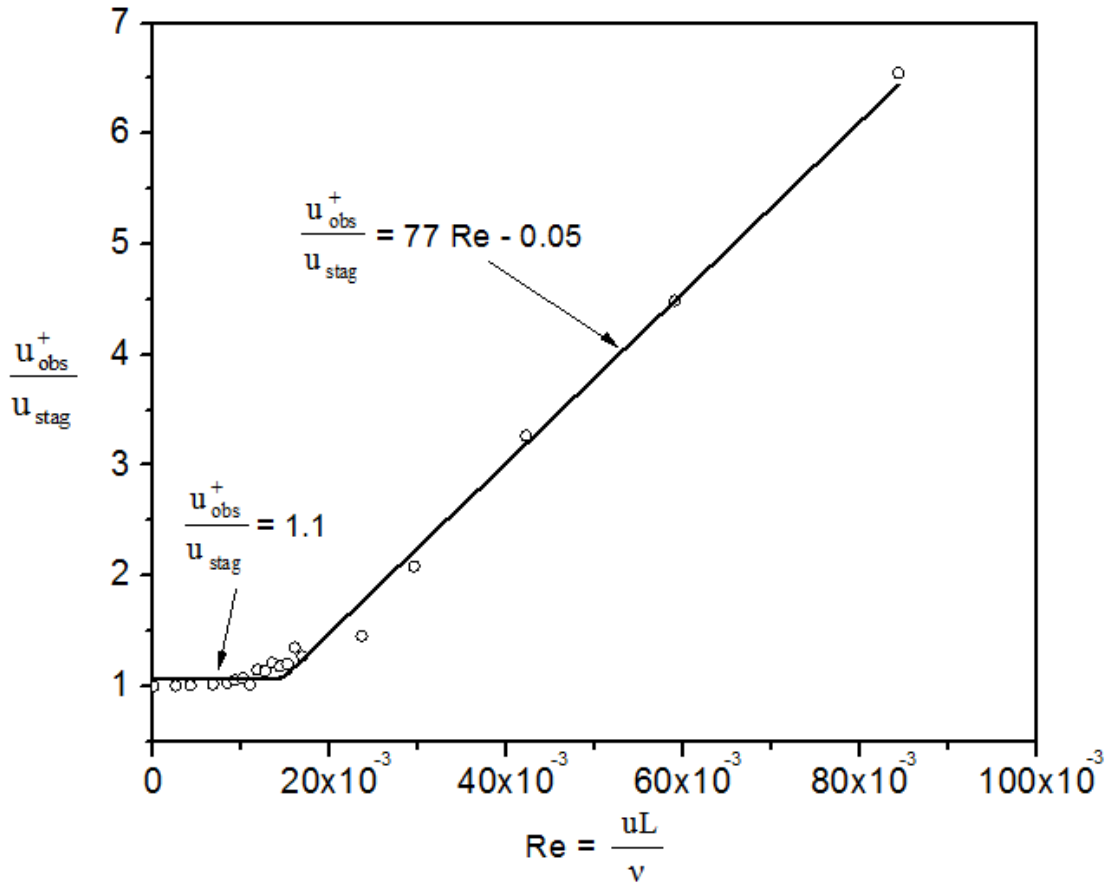

Fig. 2.4. Ratio of velocities of observed *D. primolecta* in the positive x-flow direction (u^{+}_{obs}) and stagnant *Dunaliella* (u_{stag}) versus Reynolds number (Re). The trend shows a constant velocity ratio for $15\times10^{-3} \geq Re \geq 0$ and a linearly increasing velocity ratio for $Re > 15\times10^{-3}$.

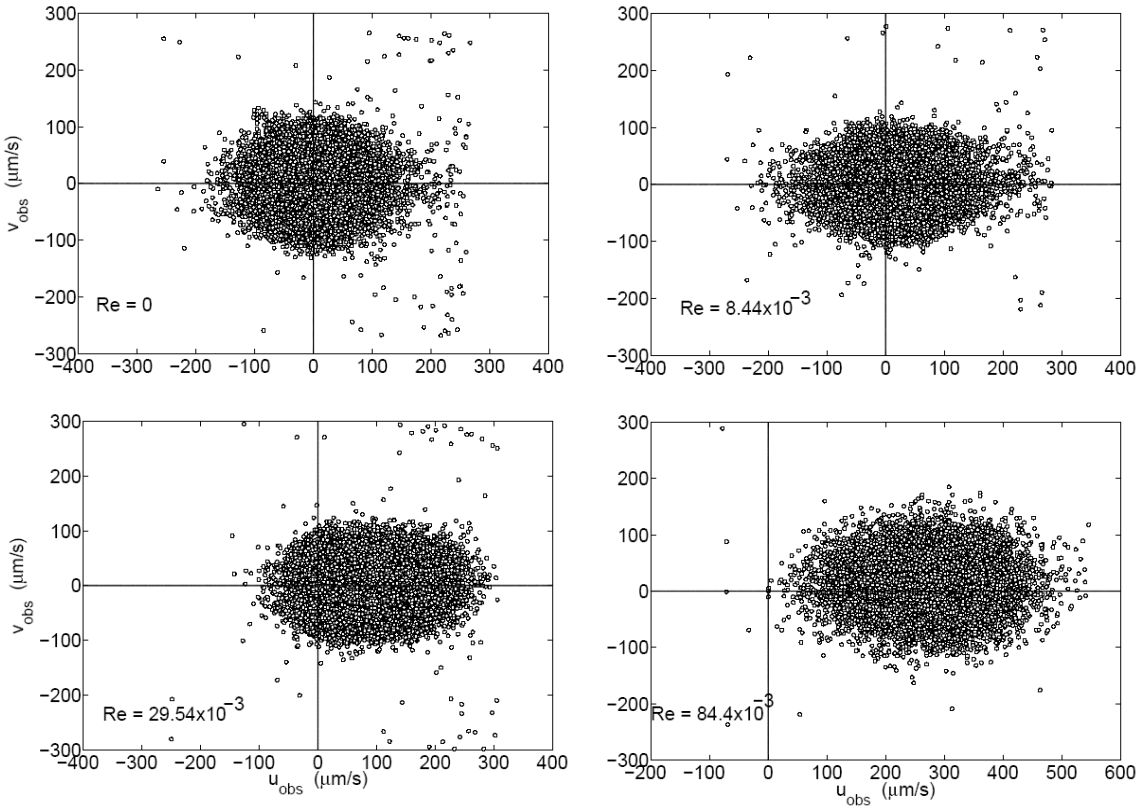

Fig. 2.5. Scatter plot of observed *D. primolecta* velocities in the longitudinal direction (u_{obs}) and observed *Dunaliella* cells in the perpendicular direction (v_{obs}) in the micro-flow channel analyzed using PTV. The u_{obs} is the combined velocity of *D. primolecta* cells and the fluid flow.

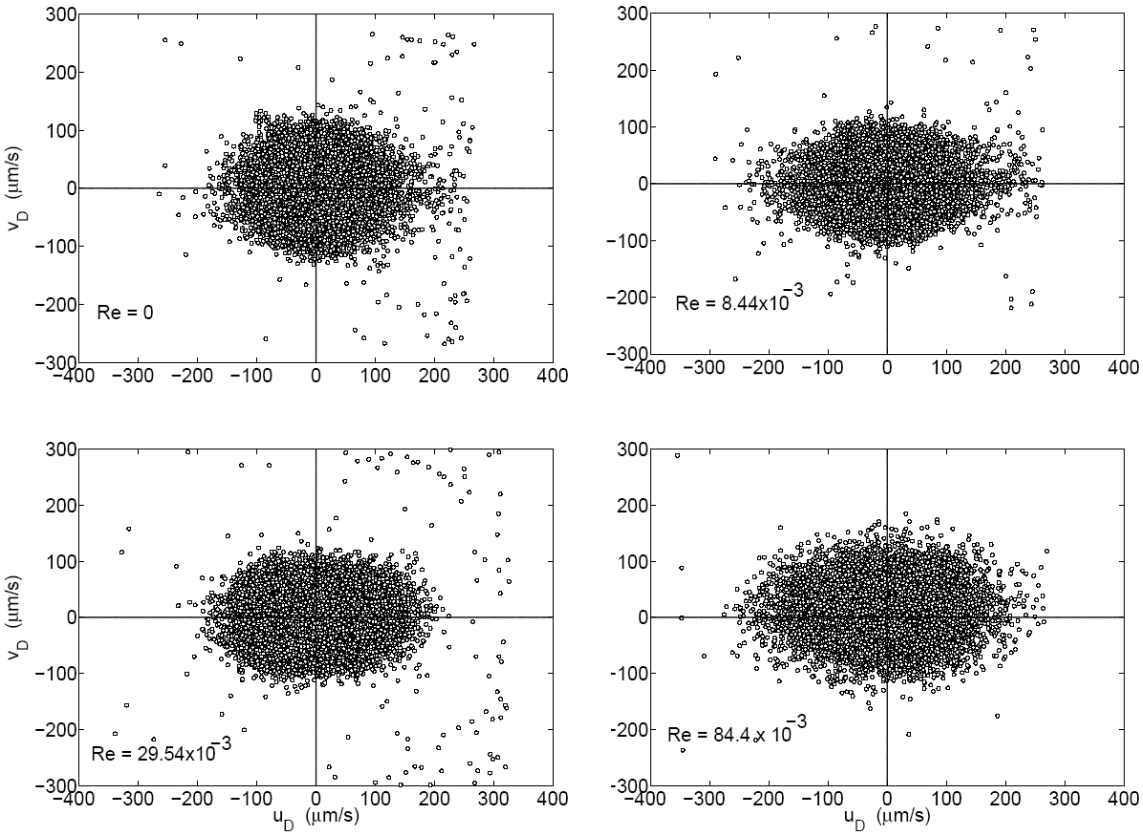

Fig. 2.6. Scatter plot of net *D. primolecta* velocities in the longitudinal flow direction (u_D) and net *D. primolecta* cells perpendicular to the flow direction (v_D) in the micro-flow channel analyzed using PTV. The net *D. primolecta* velocities in the positive x-flow direction (u_D^+) is obtained by subtracting the mean fluid flow velocity (seeded flow) from the observed *D. primolecta* (u_D) velocity in the positive x-flow direction.

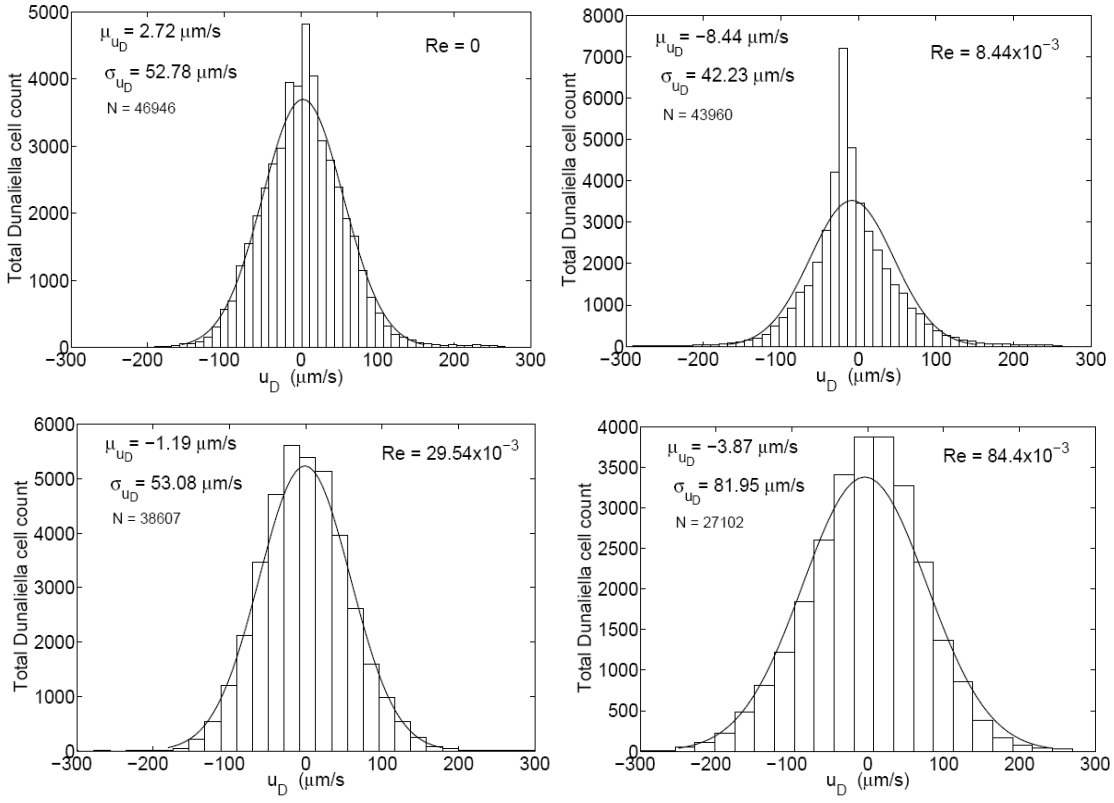

Fig. 2.7. Histogram plots of net *D. primolecta* velocity in the longitudinal flow direction observed in the micro-flow channel for 250 image pairs.

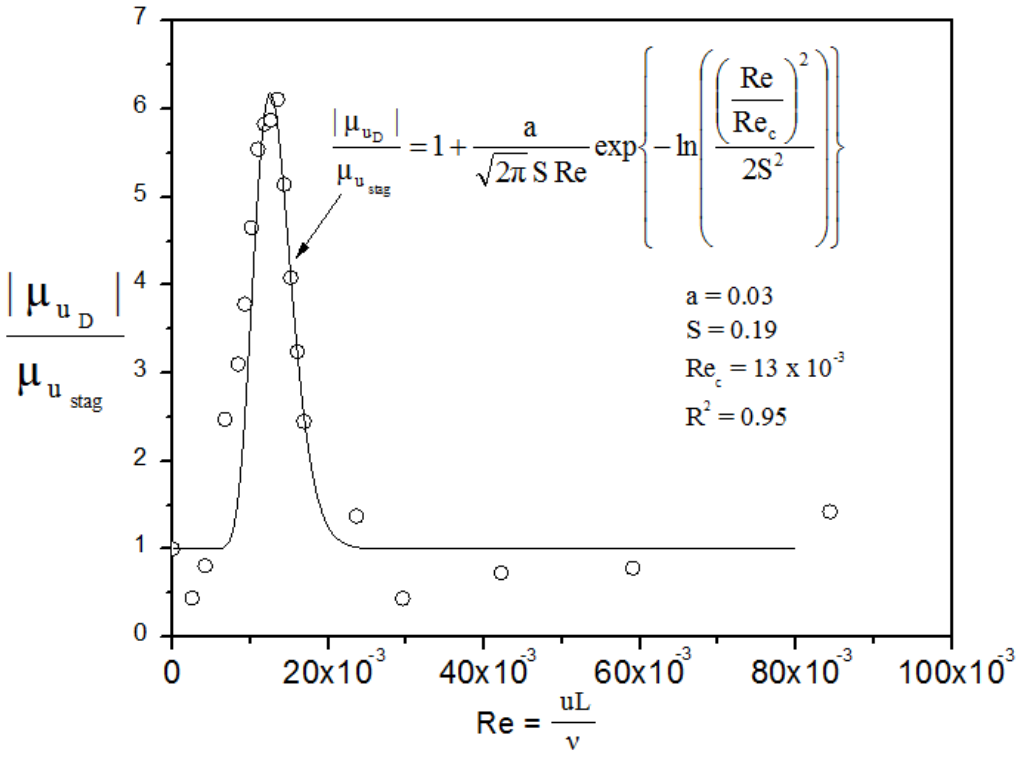

Fig. 2.8. Ratio of velocities of net *D. primolecta* in the positive x-flow direction (u_D^+) and stagnant *Dunaliella* (u_{stag}) versus Reynolds number (Re). The trend shows a linearly decreasing velocity ratio for $15\times10^{-3} \geq Re \geq 0$ and a constant velocity ratio for $Re > 15\times10^{-3}$.

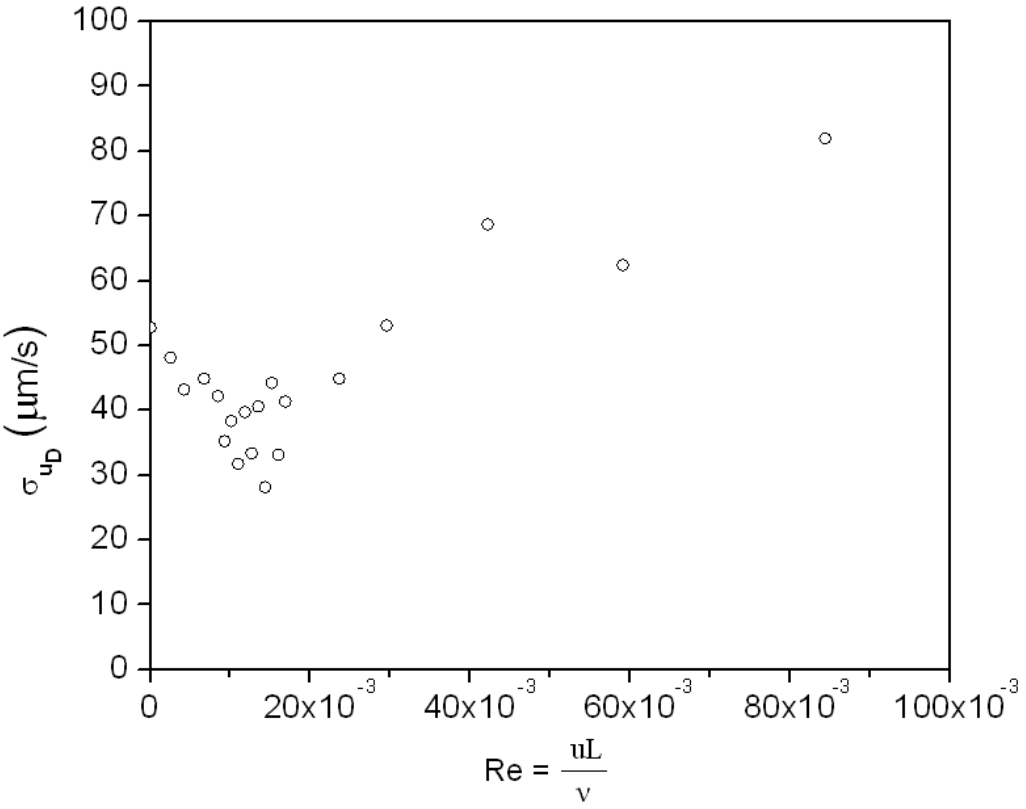

Fig. 2.9. Standard deviation plot of net *D. primolecta* velocities in the longitudinal flow direction (σ_{u_D}) observed in the micro-flow channel.

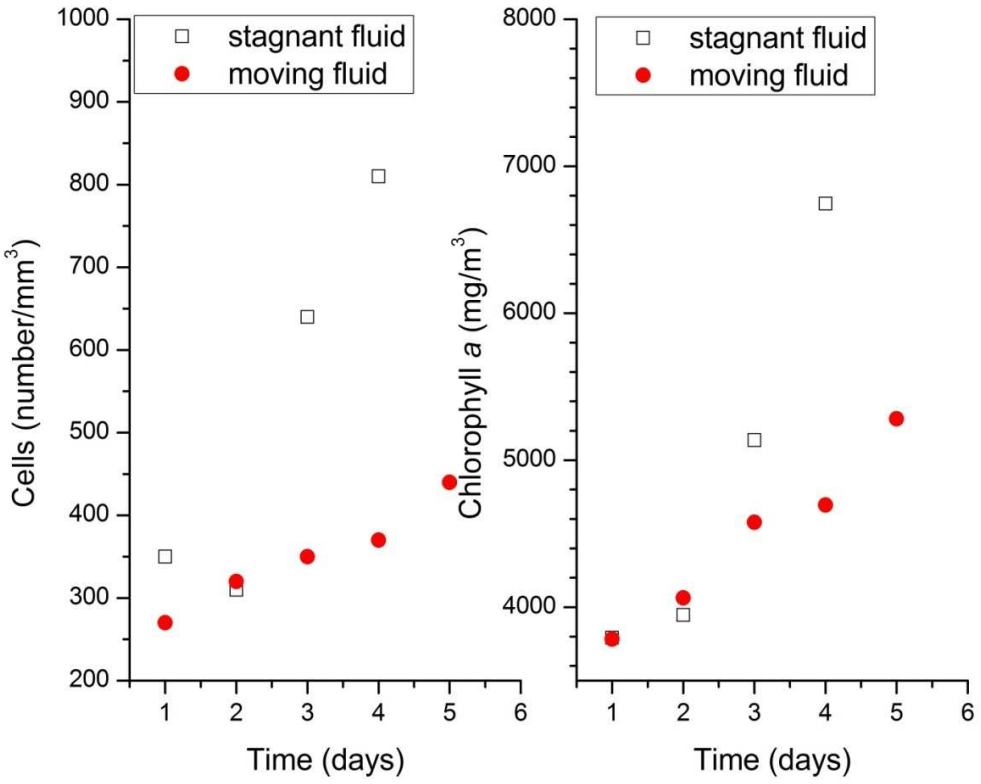

Fig. 2.10. *D. primolecta* accrual in a stagnant fluid (Re=0) and in a moving fluid with an average fluid flow energy dissipation rate $\varepsilon \sim 10^{-7}$ m^2/s^3. Experiments were conducted in a 35 L bioreactor.

Chapter 3

Fluid motion mediates biochemical composition and physiological aspects in the green alga *Dunaliella primolecta* Butcher

Published as: Chengala, A., M. Hondzo, and D. Mashek. 2013. Fluid motion mediates biochemical composition and physiological aspects in the green alga *Dunaliella primolecta* Butcher. Limnol. Oceanogr: Fluids. Environ. **3**:1-18, doi: 10.1215/21573689-2326826).

Experiments were conducted in a laboratory bioreactor to study the effect of small-scale fluid motion on the composition of some key biochemical compounds and physiological processes of the microalga, *Dunaliella primolecta* Butcher. The bioreactor with submersible speakers generated nearly homogeneous and isotropic turbulence. Fluid flow was the only systematically controlled experimental variable, with other environmental conditions, including light intensity, temperature, initial salinity and nutrient concentration nearly similar during the experimental measurements. Growth, protein and fatty acid accumulation of *D. primolecta* were enhanced by the moving fluid flow in the bioreactor. Over an 8-day long experiment under turbulent fluid flow conditions, a

twofold increase in cell number, chlorophyll, protein, and total fatty acid concentrations was observed in *D. primolecta*. Conversely, no significant increase in these variables was observed under stagnant fluid conditions. The results could have important implications for the design and operation of natural and engineered bioreactors under specified fluid flow conditions for efficient bioenergy production from microalgae.

3.1 Introduction

Microalgae are considered as feedstock for the third generation of biofuels for energy production (Brennan and Owende 2013) and provide useful cell factories for the production of an array of valuable chemical compounds, including β-carotene, glycerol, and lipids (Cohen 1999).Various types of microalgal cultures and their potential as a renewable energy feedstock have been analyzed and reviewed extensively in the literature (Stephens et al. 2010; Wijffels and Barbosa 2010; Amaro et al. 2012). Microalgae can be cultivated in arid or inhospitable land that is considered unsuitable for agricultural crops, thereby reducing competition with agriculturally productive areas of biofuel feedstock (Day et al. 2012). Typically, microalgal culture is grown in an open system (e.g., raceway ponds) or closed system (photobioreactors) for the purpose of biofuel production (Chisti 2007). To facilitate microalgal exposure to photosynthetically active radiation (PAR) and nutrients, fluid stirring is mechanically induced in both open and closed systems (Williams and Laurens 2010; Singh et al. 2011). Economic studies have indicated that auxiliary power demand associated with mechanical stirring for microalgal cultivation represents a significant cost for sustainable bioenergy production

from microalgae (Schlagermann et al. 2012). To what extent fluid stirring affects the biochemical composition of biofuel producing microalgae is unknown.

In the bioreactors, algal cells are subject to different fluid motions encompassing laminar, intermittent and turbulent fluid flow conditions. The spatial extent of fluid currents can range from large-scale eddies usually determined by the geometry of the bioreactor, down to the microscopic-scale eddies generated by the swimming of individual microalgae (Hondzo 2012). At the *cell scale,* microalgae experience a velocity gradient and corresponding energy dissipation level that modulates the diffusive sublayer thickness, a thin layer surrounding an individual cell, whereas, molecular diffusion dominates transport and corresponding nutrient uptake in the proximity of the cell. Small-scale turbulence could affect nutrient uptake (Langlois et al. 2009), cell morphology and division rate (Sullivan et al. 2003), and cell encounter rates and aggregate formation (Prairie et al. 2012). Guasto et al., (2012) suggested that the reported levels of turbulence and corresponding energy dissipation rates enhance nutrient uptake only for large microorganisms (60 – 100 μm). Their analysis was based on steady-state and spatially constant velocity gradients in the proximity of microorganisms, cell size, and molecular diffusivity of nutrients. Based on experimental measurements, Warnaars and Hondzo (2006) and Al-Homoud and Hondzo (2008) reported appreciable nutrient uptake by microorganisms smaller than the suggested cell size of 60 – 100 μm. Al-Homoud and Hondzo (2008) proposed that the Kolmogorov velocity, defined as the characteristic rotational velocity of small-scale eddies, was possibly associated with the facilitated nutrient uptake of microorganisms smaller than 60 μm. Guasto et al. (2012)

criticized the suggestion that such a characteristic velocity scale could be a Kolmogorov velocity arguing that the Kolmogorov velocity describes uniform flow incapable of increasing nutrient uptake in the proximity of microorganisms. Guasto et al. (2012) are correct in their statement that the uniform flow does not increase nutrient uptake; however, they misinterpreted the fundamental definition of the Kolmogorov velocity. The impact of small-scale turbulence on microalgae is a complex problem that can influence both physiological and behavioral aspects of microorganisms. The paradigm that small-scale turbulence negatively or positively affects microorganisms based on cell size and velocity gradients in the proximity of the cell that are constant in space and time is overly simplistic, and cannot be generalized for all microalgal species (e.g. Peters and Marrasé 2000). Moreover, strains of specific microalgae systematically change their swimming speed and corresponding velocity gradients in the proximity of the cell in response to their biochemical composition, for example, fatty acid accumulation (Hansen et al. 2013).

Dunaliella primolecta, a unicellular green microalga capable of producing biofuels (Chisti 2007) was used as a model in this study. This alga exhibits changes in several physiological and biological aspects when exposed to different stress conditions (Avron and Ben-Amotz 1992). It has been documented that, in general, *Dunaliella* morphologies depend on environmental conditions and various stages of reproduction (Borowitzka 1981). It is also known that the accumulation of β-carotene in *Dunaliella* is triggered by environmental stresses such as intense PAR, nutrient limitation, extreme temperatures and high salinity (Borowitzka et al. 1984; Raja et al. 2007). *Dunaliella* has also been

shown to rapidly increase or decrease glycerol content to acclimate to hypoosmotic or hyperosmotic environments (Chen et al. 2009). The neutral lipid (triglycerides) yield is greatest under nutrient stress conditions (i.e., low concentration of nitrogen and phosphorus) (Griffiths and Harrison 2009; Dean et al. 2010). Other reports have also shown that factors such as PAR, temperature and nutrient availability affect both lipid composition and lipid content in many algal species (Hu et al. 2008; Khozin-Goldberg and Cohen 2011). These reports suggest that cells may respond to some environmental conditions by adjusting particular aspects of their metabolism and thus change their biochemical composition. It is likely that certain intracellular levels of particular compounds may be obtained by modifying the physical and chemical environments that surround the microalgae. Our study focused on examining the effect of surrounding physical conditions on the biochemical composition and physiology of *D. primolecta.*

Our central hypothesis was that the small-scale fluid motion has an effect on the fatty acid accumulation, cell number, protein and chlorophyll concentration in *D. primolecta.* The experiments were conducted in a laboratory bioreactor with underwater speakers capable of systematically generating and replicating nearly homogeneous small-scale fluid flow velocity gradients and corresponding energy dissipation levels comparable to data reported in the field.

3.2 Materials and Methods

To scale-up laboratory measurements to field conditions, it is important to reproduce reported levels in the field within in the experimental setup. In this case, the energy

dissipation levels in aquatic ecosystems range from 10^{-6} cm^2 s^{-3} to 1 cm^2 s^{-3} (Hondzo and Warnaars 2008; O'Connor and Hondzo 2008). The generated velocity fields and velocity gradients should be equally distributed within the bioreactor so that microalgal cells do not respond to specific flow conditions imposed by the geometry of the experimental bioreactor. Musielak et al. (2009) suggested that the laboratory bioreactors that replicate steady velocity gradients with corresponding energy dissipation levels fail to capture the essence of turbulence, including the diffusion of momentum and vorticity.

3.2.1 Experimental Set-up: Speaker Flow Bioreactor

A rectangular Plexiglas chamber (54 cm × 23 cm × 23 cm (length × width × height) and a capacity of 28 L) was the bioreactor for the experiment (Fig. 3.1A). The reactor was equipped with submersible speakers (AQ339 Aquasonic, Clark Synthesis, USA) on either end to generate fluid motion by the extension and contraction of underwater speaker membranes. For different fluid flow experiments, speakers were fed with a prescribed analog electric current with the sinusoidal input of specified amplitude and frequency through a computer-controlled custom "LabVIEW" program (National Instruments, USA). The sound signal of each speaker was out of phase by 90º, thus, principally pushing the fluid control volume back and forth between the speakers within the bioreactor. Small-scale turbulent eddies were generated in the reactor by placing a grid in front of each speaker. The size of the mesh grid was 1 cm^2 with a solidity (ratio of solid mesh area to total grid area, Fig. 3.1A) of 0.4. Wide-spectrum fluorescent lights were installed outside of the top and bottom of the reactor that were controlled by a 14/10 h light/dark timer. Small openings were provided on the reactor lid for inserting the pH

electrode (model SG 1050CD; Sensorex, USA) and oxygen sensor (Optode, model 3930R sn21; Aanderaa Instruments, USA) to measure the pH and dissolved oxygen (O_2) concentration (corrected for 87.6 salinity) of the culture medium. The oxygen saturation level and the temperature of the culture medium were also recorded by the oxygen probe. Data were recorded 1 min for a 8-day duration. The bioreactor was sealed to prevent any gas or nutrient exchange in and out of the reactor. A nitrogen gas cylinder was also placed next to the bioreactor for controlled reduction of O_2 from the bioreactor on a specified daily schedule in order to prevent an inhibiting effect of oversaturated O_2 concentration on algal growth (Williams and Laurens 2010).

3.2.2 Two-Dimensional Particle Image Velocimetry Set-up

To quantify the fluid flow characteristics generated by the speakers in the bioreactor, a two-dimensional (2D) PIV setup was employed. PIV is a nonintrusive technique that measures the velocity statistics of fluid flow variables, and has a high degree of repeatability (Chengala et al. 2010). PIV system consists of a dual-processor desktop computer and TSI Insight version 3G data acquisition and analysis software(TSI Inc., USA), laser system (Gemini dual Nd : YAG, New Wave Research, USA), TSI 12-bit CCD camera (PowerView 630149G with a 2048 pixel^2 resolution), a synchronizer (TSI model 610034) and a framegrabber (model 600049). The laser optics were abridged through the use of an optical light-arm mounted with the laser on an optical breadboard. The laser arm was positioned on top of the bioreactor in order to focus laser pulses at desired positions along the *x*-*y* plane (Fig. 3.1B). The images were captured by the camera placed laterally (along the *x*-axis) to the bioreactor. The tracers particles used for

the PIV were 8 – 12 µm hollow glass spheres (TSI model 10089) with a density of 1.05 – 1.15 g cc^{-1}.

The experiments were conducted for stagnant fluid (control) and for four different fluid flow conditions achieved by varying the frequency (Hz) and amplitude (V) of the speakers. Image pairs (500) were recorded for each of the defined speaker settings in the positions within the bioreactor shown in Fig. 3.1B. Measurements were taken with a 24 mm × 24 mm field of view and the timing between each frame (ΔT) was adjusted to have a particle displacement of approximately six to eight pixels. The recorded images were processed using the Insight 3G software with typical settings of 64 × 64 pixel interrogation window and recursive Nyquist analysis using a Fast Fourier Transform (FFT) correlator and bilinear peak engine (locates the correlation peak with subpixel accuracy by fitting a set of linear functions to the highest pixel and its four nearest neighbors), to obtain the fluid flow velocities, *u* and *v*. For each speaker setting, 18 sampling locations (indicated by position numbers and *x*, *y*, *z*, in Fig. 3.1B) were quantified and used to estimate the fluid flow conditions inside the bioreactor.

3.2.3 Strain Selection and Culture Conditions

D. primolecta (8 – 12 µm**)** is a halotolerant, unicellular, motile green alga that is often used a good model system for biochemical and physiological investigations (Avron and Ben-Amotz 1992). *D. primolecta* was chosen for the experiment for the following reasons: it accumulates significant amount of lipids under normal growth conditions (Chisti 2007), disruption or bursting of cells is easier than for other algal types because it lacks a rigid cell wall (Milledge and Heaven 2011; also note that intact cell-walls can

hamper lipid recovery as well); it tolerates extreme environmental conditions (e.g. hypersalinity); it is easy to grow in the laboratory; and its growth rate is relatively high.

D. primolecta was obtained from the Culture Collection of Algae at the University of Texas at Austin (UTEX LB1000). Artificial hypersaline medium similar to the one described by Kim et al. (1993) was prepared as the growth medium for culturing *D. primolecta*: macronutrients- 1.5 mol L^{-1} NaCl (salinity 87.6), 0.040 mol L^{-1} Tris-Hcl (pH 7.4), 5 mmol L^{-1} KNO_3, 5 mmol L^{-1} $MgSO_4 \cdot 7H_2O$, 0.3 mmol L^{-1} $CaCl_2$, 0.1 mmol L^{-1} KH_2PO_4, 2 µmol L^{-1} $FeCl_3$ dissolved in 20 µmol L^{-1} EDTA, and 2.5 mmol L^{-1} $NaHCO_3$; micronutrients: 50 µmol L^{-1} H_3BO_3, 10 µmol L^{-1} $MnCl_2 \cdot 4H_2O$, 0.8 µmol L^{-1} $ZnSO_4 \cdot 7H_2O$, 0.4 µmol L^{-1} $CuSO_4 \cdot 5H_2O$, 2.0 µmol L^{-1} $Na_2MoO_4 \cdot 2H_2O$, 1.5 µmol L^{-1} $NaVO_3$, and 0.2 µmol L^{-1} $CoCl_2 \cdot 6H_2O$. The growth medium is adjusted for a pH of 7.4.

The *D. primolecta* strain was inoculated in 0.5 L of the above prepared growth medium, grown in 1L Erlenmeyer flasks incubated at 20°C and maintained on a slowly rotating (15 rpm) shaker (New Brunswick Scientific Co., USA). The cultures were grown to ~2×10^6 cells mL^{-1} (exponential stage) at 20°C under 14 h of light and 10 h of darkness (the same light conditions were also maintained later for the bioreactor). This sample culture suspension (0.5 L) was diluted in 27.5 L growth medium to make the total volume of the bioreactor equal to 28 L. The cell count for the total resulting volume was ~3×10^4 cells mL^{-1}. The pH of the total volume was adjusted to 7.4. Before the start of each experiment, the above experimental preparation was repeated, including inoculating new culture to reach ~2×10^6 cells mL^{-1} with a volume of 0.5 L and diluting this culture in fresh growth medium to start the new experiment at ~3×10^4 cells mL^{-1}. At the end of

each experiment (15 d later), the cultures were discarded. *Dunaliella* cells were microscopically visualized conducted during the sampling time to examine for possible microbiological contamination in the bioreactor (Fig. 3.1C).

3.2.4 Cell Count and Chlorophyll Pigment Analysis

Cell count was performed on the sampled culture (~5 mL) every day over the duration of the experiment using a hemocytometer. The procedure for chlorophyll pigment analysis (http://www.epa.gov/greatlakes/lmmb/methods/methd150.pdf) is detailed as follows. A sample culture (100 mL) was collected and centrifuged at 3750 rpm for 25 min at 4°C. The pellet was resuspended in 1.5 mol L^{-1} NaCl and centrifuged again at 2500 rpm for 15 min at 4°C. The supernatant was removed and 300 µL Milli-Q deionized water was placed over the top of the pellet. The sample was vortexed until it was resuspended (this action lyses and suspends the *Dunaliella* cells). A volume of 2.7 mL acetone was added to extract the pigments, and the sample was mixed by vortexing. The sample was then stored at –20°C for at least 24 h protected from light. After 24 h, the sample was again centrifuged at 2500 rpm for 15 min at 4°C. The salinity of 1.5 mol L^{-1} NaCl and subsequent suspension in Milli-Q water did not affect the stability of the pigments. The absorbance of the clear supernatant (~2 mL on the cuvette) was measured in a spectrophotometer (DR/4000V, Hach, USA) at wavelengths 750 nm, 663 nm, 645 nm and 630 nm. The chlorophyll-a (*Chl*) concentration (µg L^{-1}) was determined as follows (SCOR-UNESCO 1966):

$$Chl = \frac{[11.64A(663\text{ nm} - 750\text{ nm}) - 2.16A(645\text{ nm} - 750\text{ nm}) + 0.1A(630\text{ nm} - 750\text{ nm})]\,E_v\,F}{S_v\,L} \qquad (1)$$

where A is the absorbance, E_v is the extraction volume in mL, F is the dilution factor, S_v is the volume of sample, and L is the light path length.

3.2.5 Protein Quantification

The bicinchoninic Acid (BCA) protein assay (BCA-1; Sigma-Aldrich, USA) was used to determine the protein content in algal suspension. Culture samples (about 100 mL) from the reactor were centrifuged at 3750 rpm for 25 min at 4°C, and the pellet was resuspended in 10 mmol L^{-1} Tris buffer with 1.5 mol L^{-1} NaCl (this action did not affect the stability of the proteins). The sample was centrifuged at 2500 rpm for 15 min at 4°C, followed by the addition of 100 μL lysis buffer (CelLytic P, Sigma-Aldrich). The resulting mixture was vortexed until the pellet was resuspended and then stored at –20°C until protein assays. The pellet was thawed and then brought up to 3 mL with 10 mmol L^{-1} Tris buffer and 100 mmol L^{-1} NaCl (pH 7.4). For the preparation of working reagent, 50 parts BCA solution was added to 1 part copper (II) sulfate solution (4% w/v).Working reagent (2 mL) was transferred to a glass culture tube, and 100 μL prepared sample were added to each tube and mixed immediately by inversion with Parafilm over the top. These tubes were incubated in a 60°C water bath for 15 min and then transferred to 1-mL cuvettes and measured for absorbance at 562 nm in a spectrophotometer (Beckman DU-640, GMI, USA). Protein mass (μg) of the algal sample was calculated from a standard curve prepared using protein standards. Note that the protein standards were prepared by serially diluting 1 mg mL^{-1} bovine serum albumin (A9418 SIGMA, Sigma-Aldrich, USA) with deionized water.

3.2.6 Fatty Acid Analysis

Gas liquid chromatography (GC) was employed to extract fatty acids from *Dunaliella*. The fatty acids were extracted in a chloroform-methanol solvent, trans-esterified with methanol, and placed in hexane (Folch et al. 1957). The procedure for fatty acid extraction was as follows: 100 mL sample from the reactor was centrifuged at 3750 rpm for 25 min at 4°C. The pellet was resuspended in 1 mL of 10 mmol L^{-1}M Tris with 1.5 mol L^{-1} NaCl (pH 7.4) and centrifuged again at 2500 rpm for 15 min at 4°C. The supernatant was removed, and the remaining sample was overlaid with 1.66 mL methanol and 3.33 mL chloroform. The mixture was vortexed until it was resuspended and then stored at –20°C for a minimum of 24 h. Deionized water (1 mL) was added to the stored sample, which was then vortexed and centrifuged at 2500 rpm for 15 min at 4°C. The lower chloroform layer was transferred by Pasteur pipette to another centrifuge tube and stored at –20°C. Chloroform (2 mL) was added to the original tube, which was then vortexed, and stored at –20°C for 24 h. This sample was then centrifuged at 2500 rpm for 15 min at 4°C. The chloroform layer was removed, placed in the second tube and dried down under nitrogen gas with the addition of 1 mL 5% HCl in methanol. It was then placed in 90°C water bath for 90 min to form fatty acid methyl esters (FAMEs). The sample was allowed to cool to room temperature and 1 mL water and 1 mL hexane were added to the sample. The sample was vortexed and centrifuged at 2500 rpm for 15 min. The upper hexane layer was removed and placed in a vial. The procedure was repeated two more times with hexane and this hexane-placed sample was set for GC analysis.

The above prepared sample (placed in hexane) was used for GC analyses with a fused silica capillary column (Supelco Omegawax, model 122-7032; Agilent Technologies, USA; 30 m × 0.25 mm inner diameter (ID) × 0.25 µm film thickness), and GC system (Agilent 5890; Hewlett-Packard, USA) with flame ionization detector (FID). The temperature program was as follows: 50°C with a 2-min hold; ramp: 10°C min^{-1} to 250°C with a 15-min hold. Constant pressure of 20 psi was applied throughout the run of 37 min per sample. Analyses were initiated by injection of 1 µL sample at a split ratio of 20:1 and injector temperature of 250°C. The FID temperature was set at 300°C with air and hydrogen flow rates of 433 mL min^{-1} and 37 mL min^{-1}, respectively. Specific FAMEs were identified based on retention time using a reference standard purchased from Nu-Chek Prep, Inc. (USA) and quantified by adding 10 µL of heptadecanoic acid (C17:0) at 10 mg mL^{-1} per sample as the internal standard.

3.2.7 Fluid Flow Characteristics

Fluid flow velocities were measured to test the flow characteristics in the bioreactor. Measurements were taken on the *x*-*y* plane at 18 different positions in the bioreactor (Fig. 3.1B). The bulk fluid flow in the bioreactor was oscillatory, where the flow was unidirectionally forced back and forth between the speakers in the *x*-direction. According to the definition of Pinton and Labbe (1994), the advective time-averaged velocity, $\bar{u}(\tau)$, for an unsteady flow field at any time τ is given by the expression,

$$\bar{u}(\tau) = \frac{1}{T}\int_{\tau-T/2}^{\tau+T/2} |u(t)|dt \qquad (2)$$

where T is the time averaging window and $|u(t)|$ is the absolute value of the measured velocity. In place of using an arbitrary value for averaging window, T, the integral time scale T_{int} can be used; that is, T can be equated to T_{int} in Eq. 2 to obtain the advective time-averaged velocity using,

$$\bar{u}(\tau) = \frac{1}{T_{int}} \int_{\tau - T/2}^{\tau + T/2} |u(t)| dt \tag{3}$$

The integral time scale, T_{int} is the scale at which the energy is fed into the fluid, and can be obtained using the expression (Pinton and Labbe 1994),

$$T_{int} = \frac{\int E(f)\, df}{\int f\ E(f)\, df} \tag{4}$$

where $E(f)$ is the spectral density of the velocity series in the temporal domain. The velocity fluctuations (u') can then be obtained by subtracting the advective velocity ($\bar{u}$) obtained using the integral time scale (Eq. 3) from the measured absolute PIV velocity ($|u(t)|$), that is, $u' = (|u(t)| - \bar{u})$. In an oscillatory flow, the advantage of using the integral time scale T_{int} is that the resulting fluctuations (u') are on average 20% less than fluctuations obtained by using Eq. 2 (Haider et al. 2005). Throughout this article, we use modified $\bar{u}$ (Eq. 3, denoted u for simplicity) as the x-axis (horizontal) velocity and v as the y-axis (vertical) velocity. Note that no modification has to be made for velocity v since the flow was unidirectional in x-direction. The velocity vectors (Fig. 3.2) were quantified by the velocity magnitude,

$$V = \sqrt{u^2 + v^2} \tag{5}$$

The fluid flow conditions in the bioreactor were described using the Taylor-scale Reynolds number,

$$Re_{\lambda} = \frac{u_{rms}\lambda}{\upsilon} \tag{6}$$

where u_{rms} is the root-mean-square of u, υ is the kinematic viscosity of the fluid, and λ is the Taylor-microscale, which is often used as an estimate to characterize homogeneous and isotropic turbulent flows:

$$\lambda = (\frac{15\upsilon u_{rms}^2}{\varepsilon})^{1/2} \tag{7}$$

3.2.8 Fluid Flow Energy Dissipation

The rate of energy dissipation per unit mass (ε) was estimated from the velocity gradients obtained using the PIV measurements (O'Connor and Hondzo 2008).

$$\varepsilon(x,y) = 4\upsilon\left[\left(\frac{\partial u}{\partial x}\right)^2 + \left(\frac{\partial v}{\partial y}\right)^2 + \frac{3}{4}\left(\frac{\partial u}{\partial y}\right)^2 + \frac{3}{4}\left(\frac{\partial v}{\partial x}\right)^2 + \frac{\partial u}{\partial x}\frac{\partial v}{\partial y} + \frac{3}{2}\left(\frac{\partial u}{\partial y}\frac{\partial v}{\partial x}\right)\right] \tag{8}$$

The length scale below which velocity fluctuations are converted into heat by the action of molecular viscosity is determined by Kolmogorov scale:

$$\eta = \left(\upsilon^3 \big/ \varepsilon\right)^{1/4} \tag{9}$$

The dissipation of energy occurs primarily in the small-scale eddies and is a function of the gradients of fluid flow velocities (Eq. 8). In the bioreactor, the velocities were measured by the PIV; therefore, it was essential to conduct velocity measurements at the appropriate spatial resolution. Saarenrinne and Piirto (2000) suggested that the accurate

estimation of □ from PIV measurements mandates the spatial resolution of fluid flow velocity measurements close to the Kolmogorov microscale. We conducted PIV analyses at a spatial resolution of 0.05 cm, which is finer than the Kolmogorov microscale for low flow conditions and close to the Kolmogorov microscale for high turbulence-intensity levels in the bioreactor (Table 3.1). In our experiment, the dissipation rate was varied from ~10^{-3} cm^2 s^{-3} to ~1 cm^2 s^{-3}, a range reported in aquatic ecosystems.

3.2.9 Homogeneity and Isotropy

To investigate the effect of turbulence on microscopic organisms, research has focused on developing laboratory setups to generate isotropic turbulence conditions (Webster et al. 2004). We developed a laboratory bioreactor that can systematically generate and replicate small-scale turbulence conditions over the time scales of weeks that are needed for measuring biochemical responses in microalgae. Consequently, the flow in the bioreactor was examined for isotropy (defined as flow characteristics statistically invariant to the rotation of the coordinate system) and homogeneity (defined as flow characteristics statistically invariant to translation of the coordinate system). The check for near homogeneity (defined by the ratio of u_{rms} (x,y) to $\langle u_{rms} \rangle$ ~1, where $\langle\ \rangle$ is the spatial average of the selected position; Fig. 3.1B) in the bioreactor consisted of verifying that the spatial variation of the $\frac{u_{rms}}{\langle u_{rms} \rangle}$ statistics was minimal (Hwang and Eaton 2004). The test for near isotropy consisted of verifying that the magnitudes of u_{rms} and v_{rms} were nearly similar and that the time-averaged velocities of u and v were near zero (Webster et al. 2004).

3.2.10 Experimental Protocol and Schedule

For each experimental condition, the culture was grown in the bioreactor for a period of 15 d with the first 7 days considered the acclimatizing period for algal cells (no samples were collected during this time). On day 8, the pH of the culture medium in the reactor was brought to ~7.4 (pH was 7.4 when the experiment started and increased during the 7-day acclimatizing period), and the culture medium was nutrient enriched with initial medium concentrations of nitrate (5 mmol L^{-1} KNO_3), phosphate (0.1 mmol L^{-1} K_2HPO_4), carbonate (2.5 mmol L^{-1} $NaHCO_3$), and NaCl (1.5 mol L^{-1}) equivalent for reactor capacity (28 L), assuming that all of the above concentrations were used up during the acclimatizing period. Prior to each experimental run, nine glass slides were equally distributed at the bottom of the bioreactor. One slide was extracted from the bioreactor daily, and the sample was subjected to cell count and chlorophyll concentration measurement. Under stagnant conditions and lowest speaker settings in the bioreactor, on average 3% to 5% of microalgal biomass had settled, indicating that algal settling was minimal. At higher turbulence levels, there was no detectable accumulation of cells in the bioreactor regardless of the spatial position of the control slides. Algal samples of ~190 mL each were withdrawn from the middle section (at a distance of 12 cm from the bottom and 27 cm from the side) of the bioreactor and from the side (at a distance of 6 cm from the bottom and 0 cm from the side) of the bioreactor and were assayed for chlorophyll, fatty acids, biomass (cell count), and protein, daily for 8 days, starting on day 8 of the experiment. The reactor was filled with fresh nutrient medium to account for loss due to sampling. For the moving fluid experiments, the speakers with

specified frequency and amplitude were started on day 8 and remained running until day 15, except for a short period at each sampling time. The speaker settings remained constant over the duration of a specified experiment with the moving fluid. For all 15 days, the O_2 concentration in the reactor was brought down to 1 mg L^{-1} once a day by pumping N_2 (an inert gas) into the bioreactor. The pumping of nitrogen through the diffuser facilitated mixing in the bioreactor prior to the restart of speakers. We refer to day 8 (when the sample collection began) as day 1 for convenience, since the algal acclimatization period included the first 7 days.

3.3 Results and Discussion

3.3.1 Fluid Velocities

Sample vector plots of the instantaneous velocity fields in the middle half of bioreactor (position 5^y in Fig. 3.1B) are displayed in Fig. 3.2. Spatially distributed fine eddy structures are apparent at all fluid flow conditions. The Taylor-scale Reynolds number ranged from $Re_\lambda = 4$ to $Re_\lambda = 51$. According to Jiménez (1997), a "true" turbulence is achieved at a Taylor-scale Reynolds number approximately around $Re_\lambda \sim 30$. We were able to achieve two fluid flow conditions in the bioreactor at $Re_\lambda = 28$ and $Re_\lambda = 51$ that were close to, and larger than the suggested $Re_\lambda \sim 30$ respectively. Therefore at $Re_\lambda = 28$ and $Re_\lambda = 51$, the flow was classified as turbulent. The other fluid flow conditions with $Re_\lambda = 4$ and $Re_\lambda = 11$ did not meet the minimum required criterion for "true" turbulence. Table 3.1 gives the average of measured and estimated fluid flow statistics for all positions (1^x, 1^y, 1^z through 6^x, 6^y, 6^z) in the bioreactor (Fig. 3.1B). The reported values

represent the volume-averaged quantities of the bioreactor and are denoted by symbol [ ]. The velocity magnitude ranged from 0.068 ± 0.011 cm s^{-1} to 0.963 ± 0.021 cm s^{-1} (mean ± rms) for the corresponding Re_λ. The vertical velocity component was generally slightly larger than the horizontal velocity component. The fluid flow energy dissipation rate ranged over two orders of magnitude between the minimum (~0.001 ± (1.5 × 10^{-4}) cm^2 s^{-3}) and maximum (~0.2 ± 0.04 cm^2 s^{-3}) flow conditions. The corresponding range of Kolmogorov microscale values were from 0.2 ± 0.02 to 0.05 ± 0.006 cm. The velocity gradients were resolved by the PIV at the scale of 0.05 cm, which were similar to the Kolmogorov microscale at the highest turbulence condition.

The probability density function of fluctuating velocities, *u*' and *v*' normalized with their corresponding root-mean-square velocities, $(\frac{u'}{u_{rms}}, \frac{v'}{v_{rms}})$, are plotted for Re_λ = 51 in Fig. 3.3A. A difference between the relative root-mean-square velocities of 6% is estimated; however, both closely follow a near Gaussian distribution. The volume average of the ratio of *u* and *v* root-mean-square velocities, $(\frac{[u_{rms}]}{[v_{rms}]})$, is 0.94 for Re_λ = 51 (Table 3.1), which is close to the isotropic value of 1.0, indicating a fairly good degree of isotropy and homogeneity throughout the measured locations in the bioreactor (Fig. 3.3B). The spatial variation of $(\frac{[u_{rms}]}{[v_{rms}]})$ for the other fluid flow conditions did not vary by a large degree either. Considerable effort was taken to ensure that good flow homogeneity (defined by

$\frac{u_{rms}}{\langle u_{rms} \rangle}$ or $\frac{v_{rms}}{\langle v_{rms} \rangle}$ ~1) was achieved throughout the bioreactor for the selected speaker setting and corresponding Re_λ.

The temporal variation in the root-mean-square ratio of spatially-averaged velocities, $\frac{\langle u_{rms} \rangle}{\langle v_{rms} \rangle}$, over a 5-min interval at Re_λ = 51 is depicted in Fig. 3.4A. The variation encompasses a range from 0.75 to 1.2, indicating that near isotropy ($\frac{\langle u_{rms} \rangle}{\langle v_{rms} \rangle}$ ~1) was maintained in the bioreactor over 5-min duration of PIV recording. Similar isotropy were observed for other Re_λ with deviation not exceeding a range of ±15%. The representative time series of the instantaneous dissipation rate ε deviated significantly from the spatially-averaged $\langle \varepsilon \rangle$ (Fig. 3.4B). The instantaneous dissipation rate shows intermittency (pulses) in the flow which qualitatively agrees with the experimental measurements of Webster et al. (2004). The instantaneous pulses (~10) were up to one order of magnitude larger than the time-averaged value (~1). Other evidence to support the intermittency of turbulence at small scales is provided by the instantaneous strain rate time series (Fig. 3.4C). The one-dimensional strain rate fluctuated significantly around the time-averaged value close to zero. Our data demonstrate appreciable instantaneous spatial and temporal variability of ε and velocity gradient at small scales. The data support the suggestion of Musielak et al. (2009) that laboratory bioreactors should not reproduce steady flow and spatially uniform velocity gradients to test the effect of turbulence on nutrient acquisition by algae. Furthermore, *D. primolecta* responds to

instantaneous flow velocity gradients instead of time-averaged values (Chengala et al. 2013).

Kinetic energy spectra of fluctuating fluid flow velocities under different flow conditions in the bioreactor were determined using the Fast Fourier Transform (FFT) correlation method. The resulting energy spectrum, $E(k)$ of the two fluctuating velocity components (u', v') normalized by ε and υ, were plotted against the wave number (k) normalized by the Kolmogorov length scale (η), (i.e., $E(k)$ $(\varepsilon\upsilon^5)^{-1/4}$ on the y-axis and $k\,\eta$ on the x-axis) in Fig. 3.5. The estimates were compared with the universal Kolmogorov energy spectrum given by $E(k) = 0.535\ C_k\ \square^{2/3}k^{-5/3}$ where the universal Kolmogorov constant C_k is 0.16 for two-dimensional spectra (Hwang and Eaton 2004). The plot for both u' and v' smoothly follow the $(-5/3)^{rd}$ power law in the inertial sub-range for turbulent flow (Re_λ = 28, 51) indicating that the fluid flow was indeed turbulent at these experimental conditions. An average 10% difference was estimated between the u' and v' components for the corresponding Re_λ. The plots of other fluid flow conditions (Re_λ = 4, 11; data not shown) did not follow a smooth $(-5/3)^{rd}$ power law, indicating that turbulence was not fully developed at these conditions.

3.3.2 Dissolved Oxygen Concentration

The concentration of dissolved oxygen (O_2) in the bioreactor showed an expected diurnal trend with O_2 increasing during the lights on condition and a reversed trend during lights off condition (Fig. 3.6). For the high-turbulence condition (Re_λ = 51), with most energetic mixing in the bioreactor, the peak value of 14 – 15 mg L^{-1} was reached for most of the days during the experiment (Fig. 3.6A). For the stagnant condition, the peak value of 10

mg L^{-1} was observed during day 1; O_2 concentration then decreased to an average of ~6 mg L^{-1} during the remaining days of experiment (Fig. 3.6B). The high O_2 concentration during the high turbulence condition indicates that the flow facilitated photosynthesis in the bioreactor during most of the experimental days. The O_2 concentrations for both stagnant and turbulent flow conditions were consistent with the cell population in the bioreactor. Therefore it could be concluded that turbulent conditions facilitated algal physiology in general and photosynthesis in particular, as indicated by the higher O_2 levels in the bioreactor. The combination of turbulence with other factors, including PAR intensity and nutrient concentration, could give different results. The temperature in the bioreactor was 25ºC ± 2ºC throughout each experiment. All experiments were conducted at similar temperature condition; therefore, the results of different experiments are comparable.

3.3.3 Algal Abundance

Fig. 3.7A depicts the algal abundance or population size (N) expressed as normalized cell count ($N(t)/N_{day1}$), versus time under different fluid flow conditions in the bioreactor. During 8 days of algal growth, the cell number was the highest for the turbulent fluid flow conditions (Re_λ = 28 and Re_λ = 51). The total cell number doubled with respect to the initial cell number (ratio = 2.1 at Re_λ = 51). An increase in cell number was also observed at nonturbulent conditions (Re_λ = 11) with cell number increasing an average 30% by the end of the experiment. Under stagnant and low flow conditions ($Re_\lambda \approx 0$ and Re_λ = 4), no appreciable change in the total cell number was observed in the bioreactor.

3.3.4 Chlorophyll and Protein Content

Chl accounted for most (95%) of the total chlorophyll concentration in the present study of *D. primolecta*. For the highest turbulent condition (Re_λ = 51), normalized total chlorophyll (C_{chl}(t) / $C_{chl\,(day1)}$) doubled (ratio = 2.1) by the end of the experiment on day 8 (Fig. 3.7B). C_{chl} showed patterns similar to those of the total cell count. Under stagnant and low flow conditions ($Re_\lambda \approx 0$ and Re_λ = 4), an average constant ratio close to 1 was apparent. The results indicate that fluid flow conditions modulate total chlorophyll content of the cultures, which is consistent with the cell number measurements.

Proteins facilitate the growth of cells and help in metabolic and structural functions of the cell. *Dunaliella* has been shown to contain an array of proteins modified by the covalent attachment of fatty acids and is reported to have a high protein content of 35% - 48% (Gibbs and Duffus 1975). In our experiment, turbulence favored accumulation of protein in *D. primolecta*. Normalized protein (C_p(t) / $C_{p(\text{day1})}$) had a ratio of about 2 for the highest turbulent condition (Re_λ = 51) at the end of the experiments. In contrast to the normalized chlorophyll ratio (which had a ratio of one) at the end of the experimental period (day 8), the protein ratio of the stagnant condition was reduced to 0.6 (Fig. 3.7C).

3.3.5 Fatty Acid Composition

Fatty acids serve as both energy storage and structural components of the cell. Reports on the composition of lipids and their constituent fatty acids in *Dunaliella* species (Fried et al. 1982; Griffiths and Harrison 2009) include a high occurrence of unsaturated and polyunsaturated fatty acids. In general, unsaturated fatty acids are beneficial for the flow

properties of biodiesel, especially under low temperatures, as occurs frequently in aviation uses. Following a trend similar to that of proteins, total chlorophyll, and cell count, the normalized total fatty acid mass in *D. primolecta* was observed to maximize accumulation under the high-turbulence conditions (Fig. 3.7D). Under the stagnant flow condition, the fatty acid mass increased initially and then decreased after day 3 and ended the experimental period with a ratio of 1.

The accumulation of fatty acid mass per cell under different fluid conditions was compared for day 1 and day 8 (Fig. 3.8). At the beginning of experimental run (Fig. 3.8A, day 1), the mass of fatty acid per cell was dominated by unsaturated (C18:1) and polyunsaturated (C16:4, C18:2, C18:3) fatty acids. Over the remaining 7 days of the experiment, the mass of fatty acids per cell increased compared with initial conditions (Fig. 3.8B). Overall, the highest accumulation of fatty acids was observed at the most energetic turbulence conditions in the bioreactor (Fig. 3.8C). Under the stagnant fluid condition ($Re_\lambda = 0$), fatty acids showed little accumulation.

The dominance of the shorter-chain fatty acids (12 and 18 carbon atoms long) indicates the potential of *D. primolecta* for the production of biofuels. Ben-Amotz et al. (1985) suggested that nitrogen deprivation did not increase lipid content in *Dunaliella* species, thus indicating that nutrient stress might not be the only factor influencing lipid storage. *Dunaliella* is known to alter its lipid composition in response to nutrient (phosphorus) stress (Siron et al. 1989), halostress (Al-hasan et al. 1987), and light conditions (Gordillo, et al. 1998). Our experiments suggest that, in addition, fluid flow conditions mediate the fatty acid composition of *D. primolecta.*

3.4 Significance to Aquatic Environments

Algal cells are subject to a range of velocity gradients and corresponding energy dissipation levels in the aquatic environments. In this study, a fluid flow bioreactor capable of producing energy dissipation rates reported in aquatic environments was used to quantify algal response to variable fluid flow conditions. The experimental set-up generated nearly homogeneous and isotropic turbulence. At the Kolmogorov scale, energy dissipation levels depicted spatial and temporal variability, with instantaneous values an order of magnitude larger than time-averaged values. In contrast to the stagnant fluid condition, moving fluid enhanced biomass, cell abundance, protein and total fatty acid accumulation in *D. primolecta.* The highest turbulence flow condition tested (Re_λ = 51), with corresponding volume-averaged energy dissipation rate in the range $\varepsilon = 10^{-1}$ to 1 $cm^2\ s^{-3}$, generated the highest accumulation of fatty acids in *D. primolecta*. Our results indicate that maintaining high turbulence or stirring conditions in natural and engineered aquatic environments could enhance the potential of *D. primolecta* for biofuel production.

Table 3.1. Fluid flow statistics averaged over the volume of the bioreactor.

$[Re_\lambda]$ (–)	$[u]$ (cm s^{-1}) $\times 10^{-3}$	$[v]$ (cm s^{-1}) $\times 10^{-3}$	$[V]$ (cm s^{-1}) $\times 10^{-3}$	$[u_{rms}]$ (cm s^{-1}) $\times 10^{-3}$	$[v_{rms}]$ (cm s^{-1}) $\times 10^{-3}$	[□] (cm^2 s^{-3}) $\times 10^{-4}$	$[\lambda]$ (cm) $\times 10^{-1}$	$[\eta]$ (cm) $\times 10^{-1}$	$\frac{[u_{rms}]}{[v_{rms}]}$ (–)
4	46.2	49.5	68	81.7	91.3	11.3	5.32	1.72	0.88
11	101.7	85.5	133	225	198.8	63.8	4.93	1.12	1.13
28	356	408	542	597	668	795	4.74	0.59	0.89
51	588	762	963	991	1051	2012	5.07	0.47	0.94

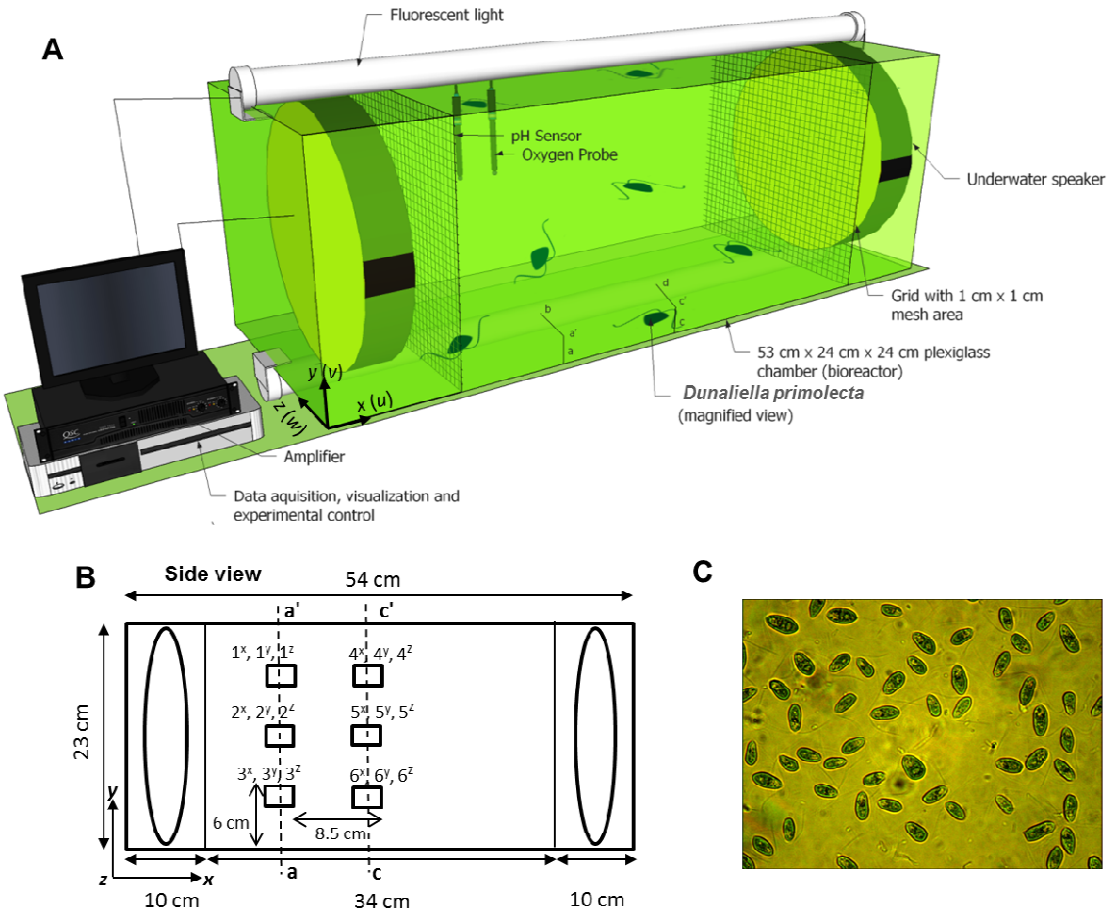

Fig. 3.1. (A) Experimental set-up of the bioreactor. The reactor has two underwater speakers on either side with a steel grid in front of each speaker. It is equipped with an amplifier (connected to the speakers), fluorescent lights, and pH and oxygen sensors. The computer is connected to the bioreactor for data acquisition, visualization and experimental control. (B) Particle image velocimetry sampling locations (*x*, *y*, *z*) refer to the sampling locations perpendicular to the side wall (*y*-direction) of the bioreactor. (C) Microscopic images of *D. primolecta* cells (average cell length is about 10 µm).

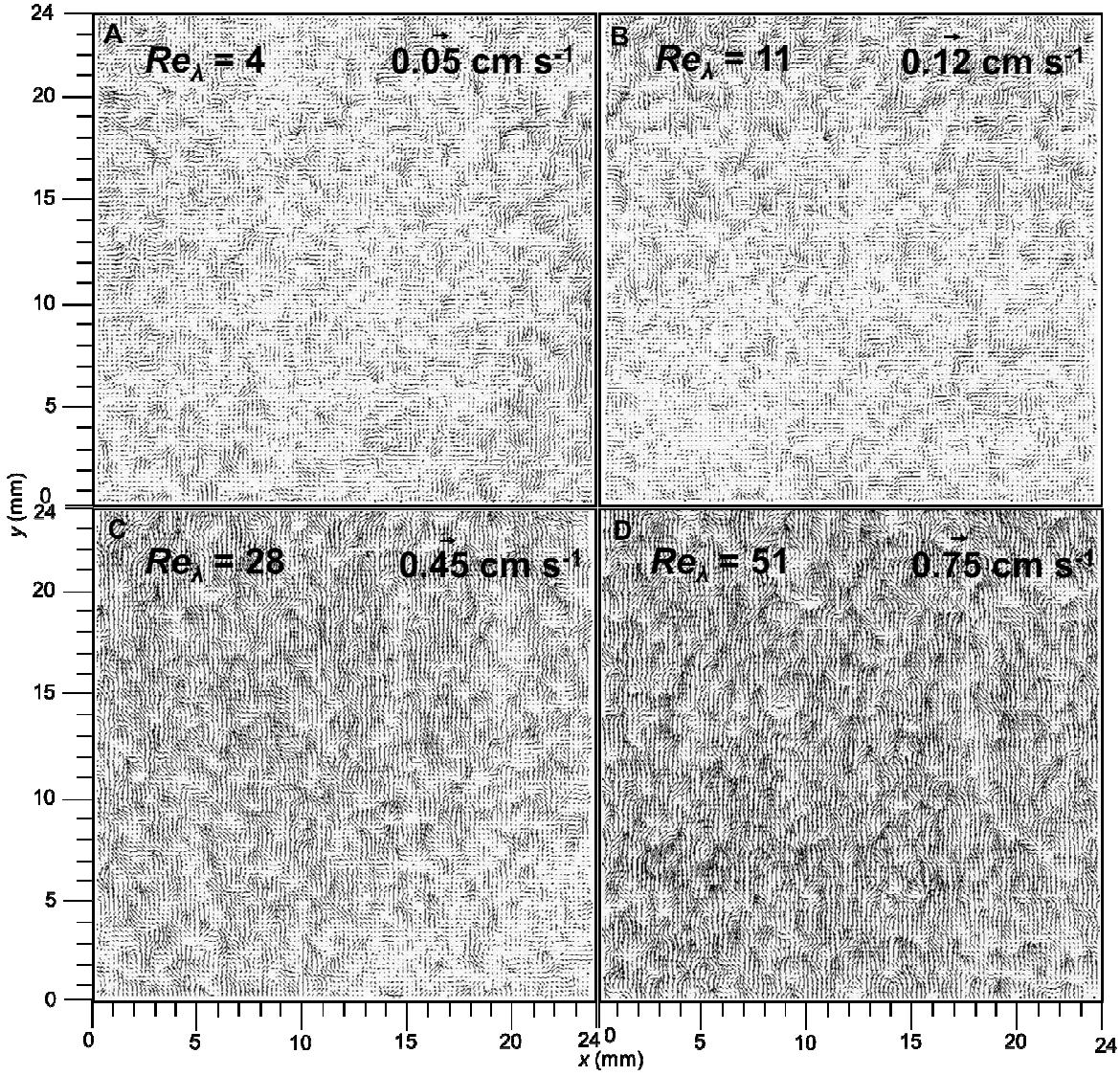

Fig. 3.2. Representative instantaneous velocity vectors (V) of the tracer particles taken at the middle half section (position 5^y in Fig. 3.1B) of the bioreactor under four fluid flow conditions. The flow is characterized by Taylor-scale Reynolds number, $Re_\lambda = \frac{u_{rms}\lambda}{\upsilon}$, where u_{rms} is the root-mean-square velocity of u; λ is the Taylor-microscale, and υ is the kinematic viscosity of the culture medium. (A) Re_λ = 4. (B) Re_λ = 11. (C) Re_λ = 28. (D) Re_λ = 51. The measuring field of view is 24 mm × 24 mm.

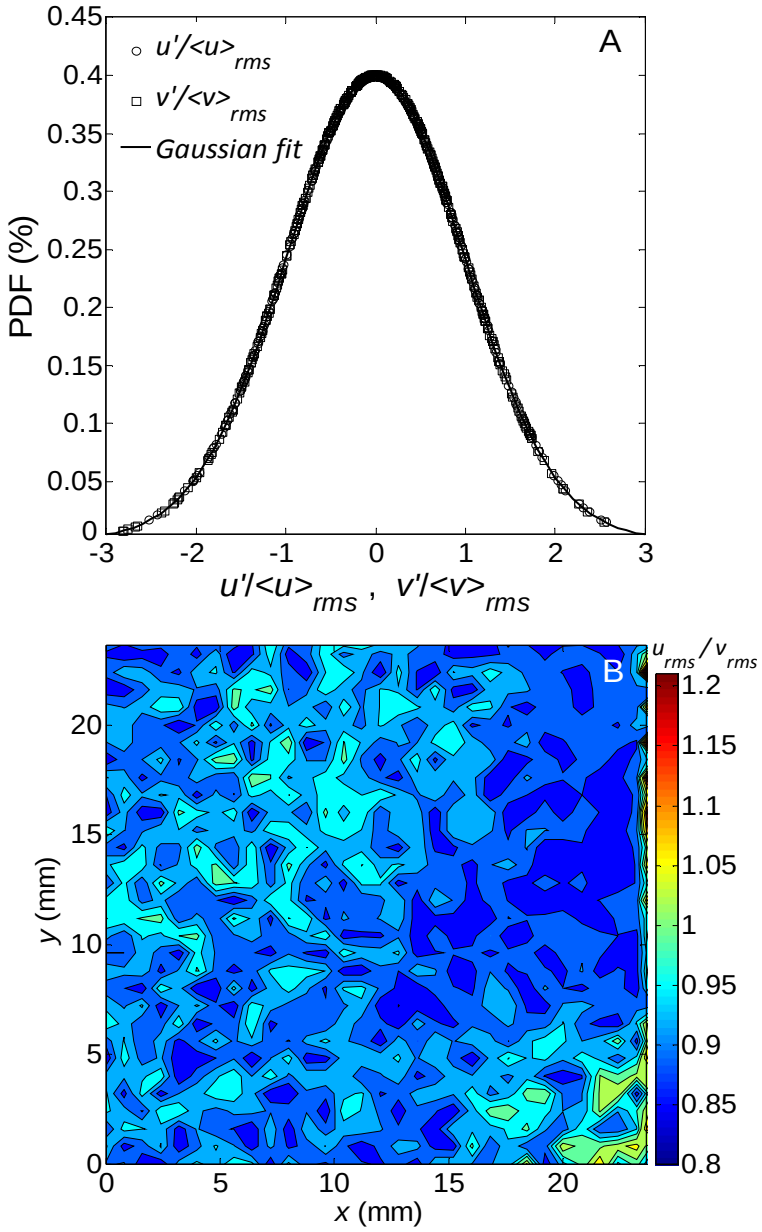

Fig. 3.3. (A) Probability density function (PDF) of the fluctuating velocities (u', v') normalized by their corresponding root-mean-square velocities ($\langle u_{rms} \rangle, \langle v_{rms} \rangle$) for Re_λ = 51. (B) A representative contour map at Re_λ = 51 of instantaneous spatial velocities within the measuring field of view in the bioreactor.

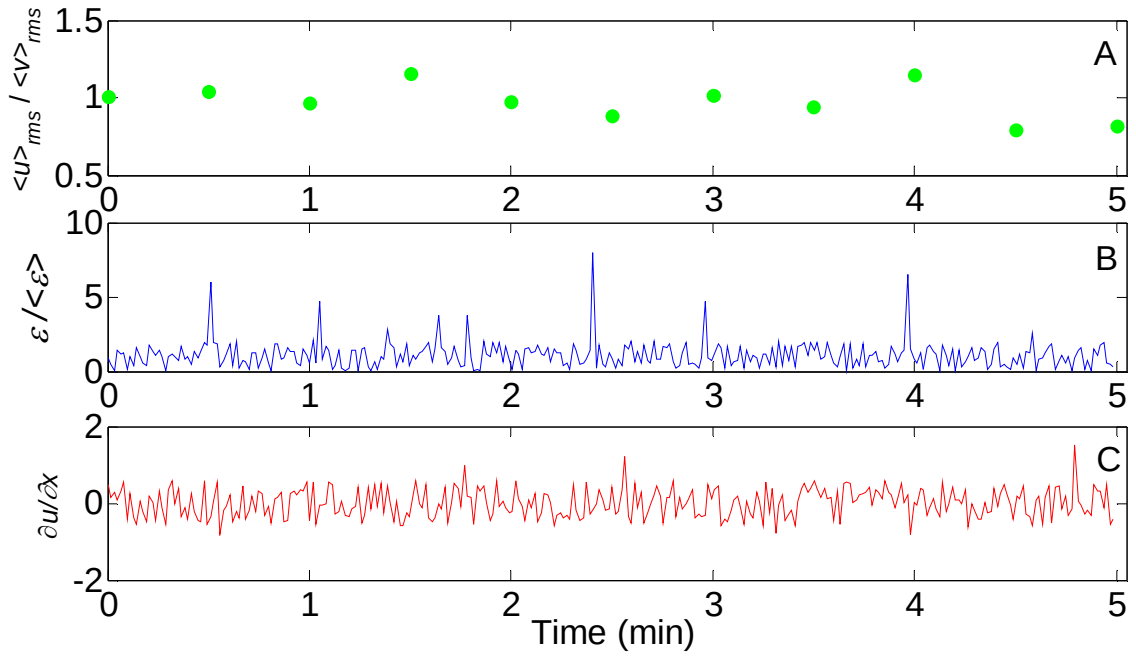

Fig. 3.4. (A) Time series of spatially-averaged root-mean-square velocities $(\frac{\langle u_{rms} \rangle}{\langle v_{rms} \rangle})$. (B) Instantaneous dissipation rate ε (evaluated in the center of field of view; 24 mm × 24 mm) normalized by the window-averaged spatially averaged $\langle \varepsilon \rangle$. (C) Instantaneous one-dimensional strain rate evaluated in the center of field of view. All measurements were collected at position 5^y in the bioreactor (see Fig. 3.1B).

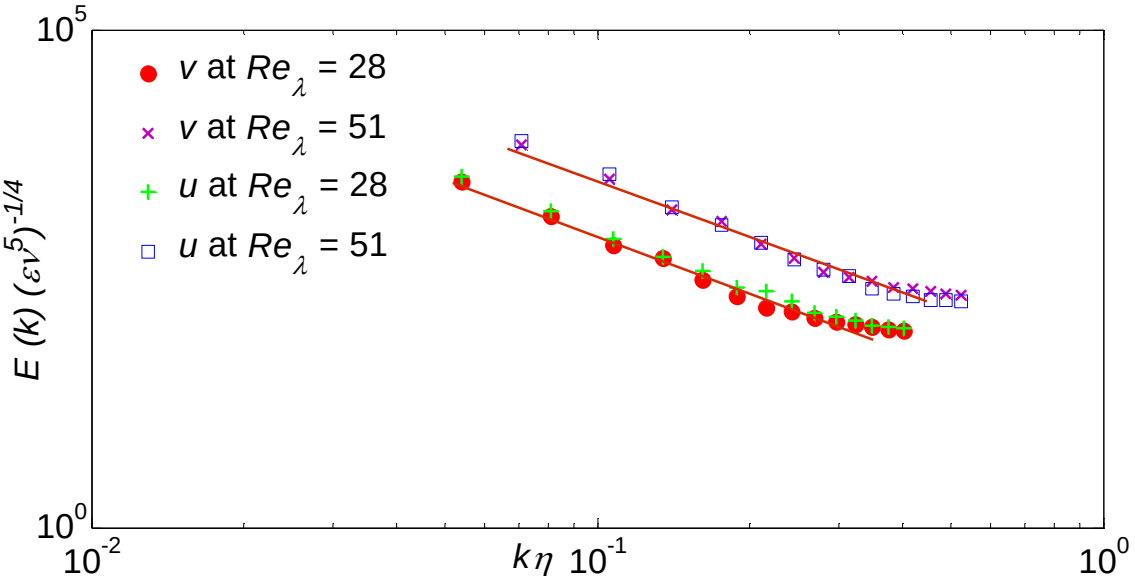

Fig. 3.5. Fluid flow kinetic energy spectra normalized by energy dissipation and kinematic viscosity ($E(k)(\varepsilon\upsilon^5)^{-1/4}$; y-axis) versus wave number (k) normalized by the Kolmogorov microscale (η) ($k\eta$; x-axis).

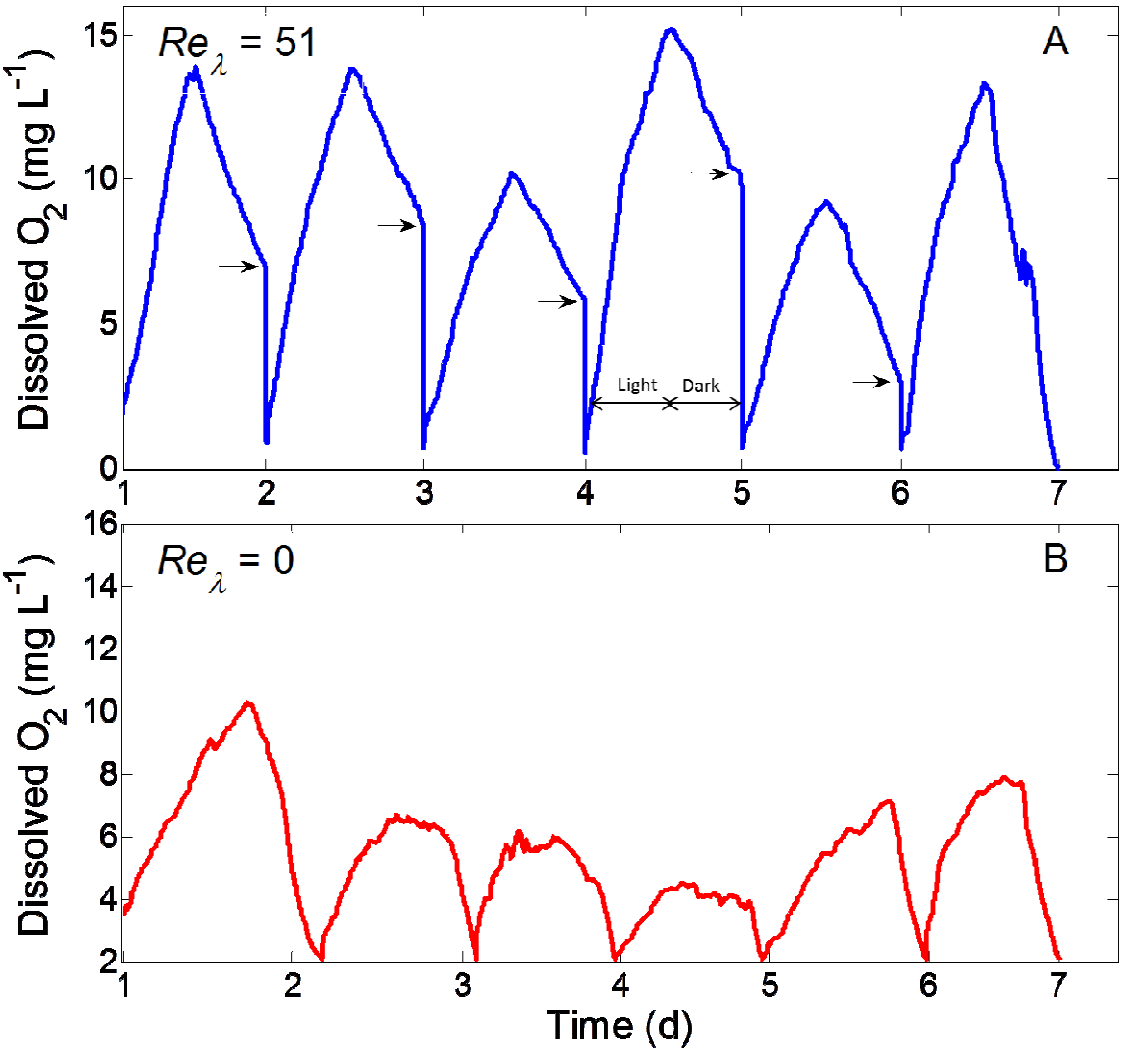

Fig. 3.6. Time series of the measured dissolved O_2 concentration in the bioreactor for a period of 6 days for (A) high turbulence flow ($Re_\lambda = 51$) and (B) stagnant fluid ($Re_\lambda = 0$).

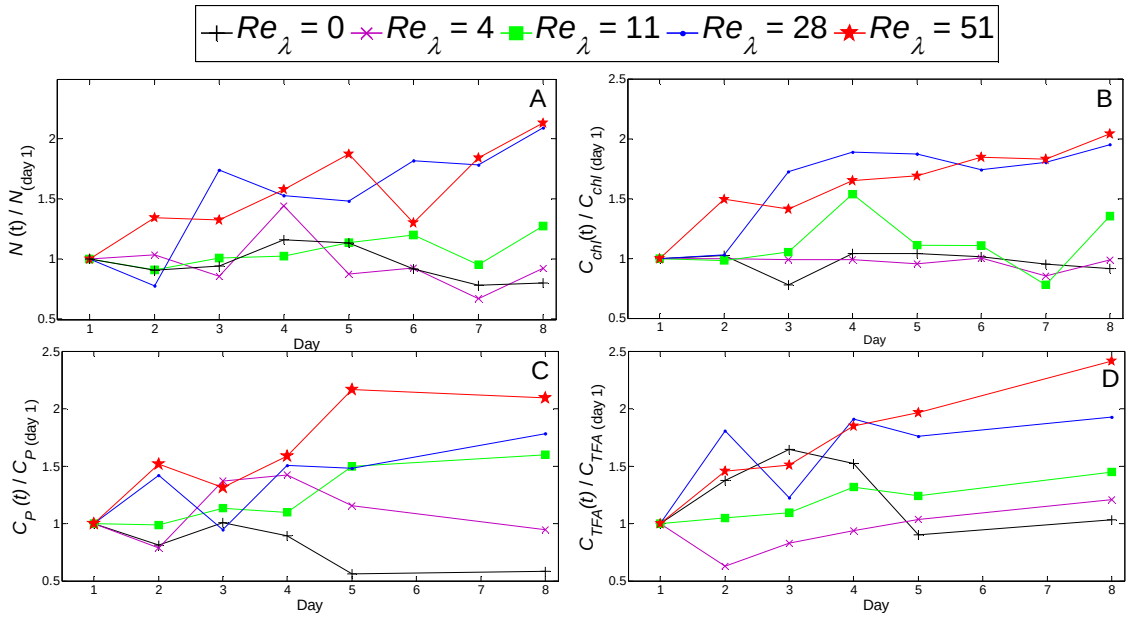

Fig. 3.7. (A) Time series of normalized cell count (N(t)/N$_{(day1)}$), where $N(t)$ is the total cell count on day t and N$_{(day1)}$ is the cell count at day 1 of the experiment. (B) Normalized chlorophyll concentration (C_{chl} (t) / $C_{chl\ (day1)}$), where $C_{chl}(t)$ is the total chlorophyll on day t and $C_{chl\ (day1)}$ is the chlorophyll concentration at day 1 of the experiment. (C) Normalized protein concentration (C_p(t) / $C_{p(day1)}$), where $C_p(t)$ is the total protein concentration day t and $C_{p(day1)}$ is the total protein concentration at day 1 of the experiment. (D) Time series of normalized total fatty acids (C_{TFA}(t) / $C_{TFA(day1)}$), where $C_{TFA}(t)$ is the total fatty acid counts day t and $C_{TFA(day1)}$ is the total fatty acid count of at day 1 of the experiment.

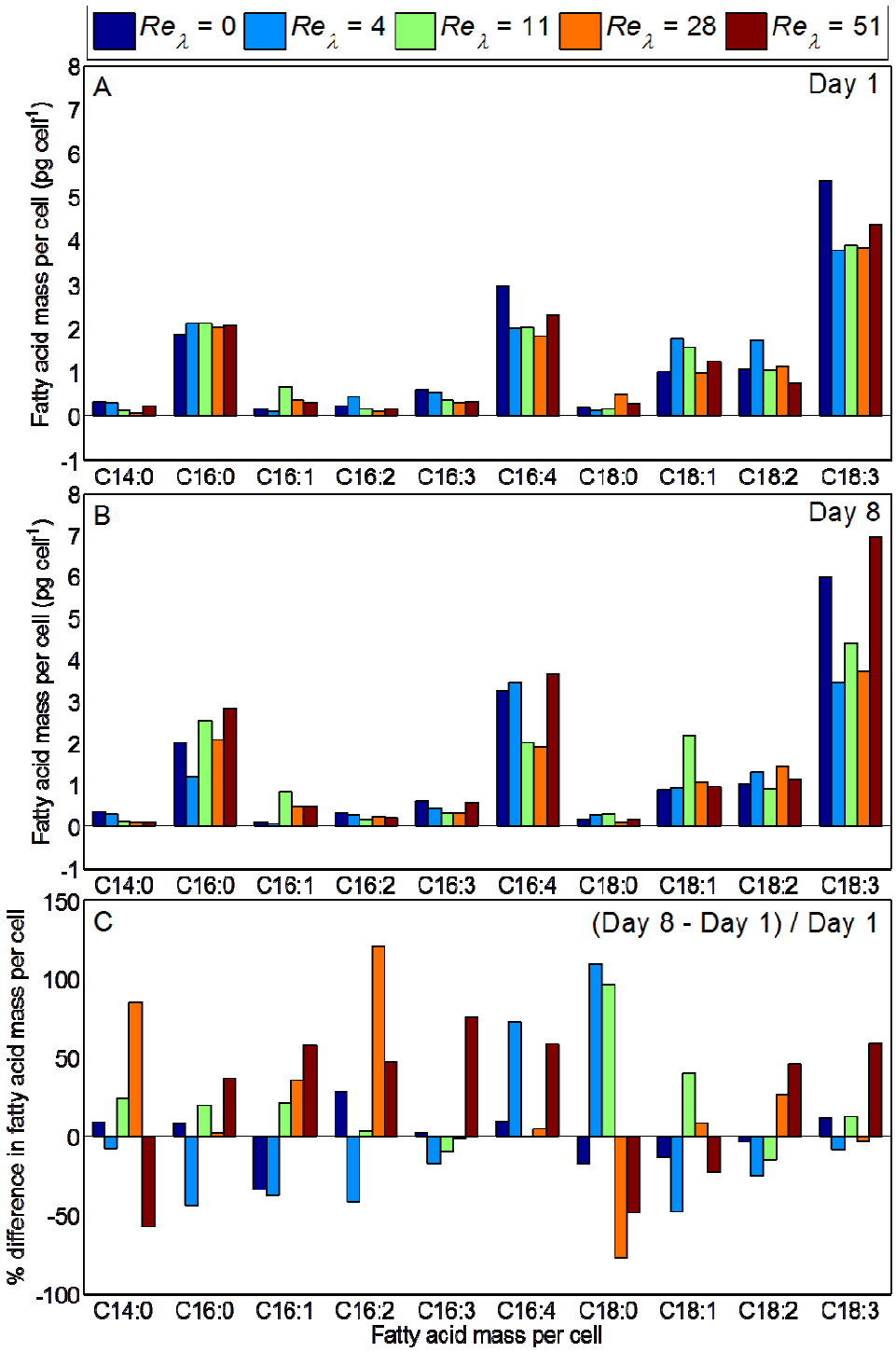

Fig. 3.8. Fatty acid mass per cell at different fluid flow conditions in the bioreactor. (A) Day 1. (B) Day 8. (C) The difference in percent fatty acid mass accumulation per cell over a 7 day period.

Chapter 4

A Microalga Propels Along Vorticity Direction in a Shear Flow

Published as: Chengala, A., M. Hondzo, and J. Sheng. 2013. Microalga propels along vorticity direction in a shear flow. Phys. Rev. E. 87:052704, doi: 10.1103/PhysRevE.87.052704.

Using high speed digital holographic microscopy and microfluidics, we discover that, when encountering fluid flow shear above a threshold, unicellular green alga *Dunaliella primolecta* migrates unambiguously in the cross-stream direction that is normal to the plane of shear and coincides with the local fluid flow vorticity. The flow shear drives motile microalgae to collectively migrate in a thin two-dimensional horizontal plane and consequently alters the spatial distribution of microalgal cells within a given suspension. This shear-induced algal migration differs substantially from periodic rotational motion of passive ellipsoids, known as Jeffery Orbits, as well as gyrotaxis by bottom-heavy swimming microalgae in a shear flow due to the subtle interplay between torques generated by gravity and viscous shear. Our findings could facilitate mechanistic solutions for modeling planktonic thin layers and sustainable cultivation of microalgae for human nutrition and bioenergy feedstock.

4.1 Introduction

Most microalgae are motile and swim in three-dimensional (3D) complex trajectories (Sheng et al. 2007) that allow them to explore and interact with the surrounding environment. Spatial gradients of environmental stimuli are known to alter microorganism swimming behavior and cause taxes (Pedley and Kessler 1992; Fenchel 2002; Kiørboe and Jackson 2001) including chemotaxis, gyrotaxis, phototaxis, and rheotaxis. Insights on these directional migrations have strong implications for predator-prey interactions (Sheng et al. 2007), micro-rheology of active particle suspensions (Rafai et al. 2010), microorganism nutrient exploration (Blackburn et al. 1998), the carbon cycle (Longhurst 1991), high-concentrations of microorganism aggregation within oceanic and lake thin layers (Durham et al. 2009), and biofuel and nutrition production by microalgae (Wijffels and Barbosa 2010; Sing et al. 2011). Although motile microorganisms encounter diversity of fluid flow environments (LeBlond and Mysak 1978; Dekshenieks et al. 2001), and flow affects their physiological and behavioral functions (Koehl et al. 2003; Estrada and Berdalet 1997, Peters and Marrasé 2000; Kessler 1985), fewer reports on shear responses (Pedley and Kessler 1992; Durham et al. 2009; Kessler 1985; Marcos et al. 2012) have been documented. We present an experimental observation that a green alga, *Dunaliella primolecta,* responds to the flow shear by reorienting itself and swimming in the cross-stream direction normal to the plane of shear (*x*-*z* plane in Fig. 4.1(b)), which is also the direction of local flow vorticity (*y*-axis shown in Fig. 4.1(b)). This migration is substantially different from the cell swimming towards or away from the oncoming flow, known as rheotaxis (Montgomery

et al. 1997; Bretherton and Rothschild 1961; Hill et al. 2007), as well as organisms with asymmetric shape and/or body density reorienting and swimming in the plane of shear as a result of the combined effect of gravitational and viscous forces, coined by Kessler (1985) as gyrotaxis (Pedley and Kessler 1992; Durham et al. 2009; Kessler 1985). In this paper, we demonstrate that *D. primolecta* does not behave like a passive particle in a shear flow. We will also show that this shear-induced response causes collective directional migration and alters the spatial distribution of microalgal concentration within a suspension.

4.2 Methods and Materials

D. primolecta is a bi-flagellated unicellular green alga with a body length of about 10 µm (inset in Fig. 4.1). The alga is reported as neutrally buoyant (Borowitzka and Borowitzka 1989) since it accumulates on average 23% of its body weight with lipids and is often targeted for biofuel and human nutrition production (Olmos et al. 2000). Using microfluidics and high-speed digital holographic microscopy (DHM, Sheng et al. 2006, 2010), we have quantified 3D swimming characteristics of *Dunaliella* in a shear flow. The experiments were conducted in a straight Polydimethylsiloxane (PDMS) micro-channel of 35 × 3.5 × 0.42 mm^3. The suspensions of *Dunaliella* were injected into the micro-channel by a computer controlled syringe pump to provide different shear stimuli ($S=du/dz$) at 0, 0.1, 1, 5, 10, and 20 s^{-1}. The obtained streamwise flow velocity distribution agreed well with the profiles of a two-dimensional (2D) Poiseuille flow (Fig. 4.6). A digital holographic microscopy (Fig. 4.5 and details in (Sheng et al. 2010)) incorporated with a Nikon TS-100 microscope was used to image a sample volume of

760 × 760 × 420 μm^3. An imaging objective with the magnification of 20× (Super Plan Fluor 20×) was used. The lighting was provided by a 7 mW He-Ne collimated laser (red, 0.632 μm wavelength). The wavelength of the laser was selected specifically within the range that *Dunaliella* were known to be insensitive to (Foster and Smyth 1980). Additionally, to minimize the effect of phototaxis, uniform intensity of red laser lighting throughout the experimental section was provided. The original holograms were recorded by a 2K × 2K CCD camera (Imperx 4M15L) and were streamed continuously at the rate of 15 frames per second (fps) to a data acquisition computer. Each time sequence consisted of three minutes recording, totaling 1000 holograms per sequence. In-house digital reconstruction and analysis software enabled simultaneous tracking of thousands of particles located within suspensions (Sheng et al. 2010). Positions of *Dunaliella* were computed from in-focus images based on cell morphology. Microalgal swimming velocities and directions were obtained from 3D trajectories. Additional information on cell orientations (zenith angle, ϕ and azimuthal angle, θ (Fig. 4.3(b))) were also generated from the in-focus images. High-speed microscopic movies at the magnification of 100× were employed to further quantify the kinematics of beating flagella and rotational motion of the cell body as well as to provide the phenomenological basis for a physical model.

4.3 Results and Discussion

In a quiescent flow, *Dunaliella* swims in a complex 3D trajectory with random body orientation (Fig. 4.1(a)). While propelling forward, the cell rotates along the fore-aft axis

at ~2Hz counter clockwise, viewed from the rear of the cell body (Fig. 4.2(a), and Schoevaert et al. 1988; Vismara et al. 2004). Note that *cis* (located closer to the eyespot) and *trans* (the other) flagellum of *Dunaliella* beat asynchronously (Schoevaert et al. 1988) with occasional synchrony. Flow shear has no obvious effects on the kinematics of flagella. As the fluid flow in the micro-channel exceeds a critical shear of 10 s^{-1}, *Dunaliella* ***reorients*** the cell body (Figs. 4.1(b)-4.1(d)) and swims in the cross-stream direction (*y*-axis or the spanwise flow direction) that is perpendicular to the plane of shear (*x*-*z* plane). The critical shear regions are situated close to the top and bottom walls of the micro-channel. The observed thickness is extended up to 150 μm from either wall. Close inspection of swimming directions in the critical shear regions revealed that *Dunaliella* prefer to swim in the direction of the local flow vorticity, $\omega_y = (\frac{\partial w}{\partial x} - \frac{\partial u}{\partial z})/2$ (symbols as defined in Fig. 4.1(b)). In the region near the bottom wall, flow vorticity pointing in the positive *y*-axis corroborates with the dominant cross-stream migration direction (in-focus cell images superimposed on the *x*-*y* plane shown in Fig. 4.1(c)), whereas near the top the trend reverses (Fig. 4.1(d)). Swimming in the negative vorticity direction is largely absent, if not completely. In the mid-section of the micro-channel where the shear is weak, cells are advected by the flow. The trajectories of these cells appear as streaks aligned in the streamwise direction, and are consequently removed from Fig. 4.1(b) for clarity. No vertical migration in the z-direction was observed. The diagonal trajectories shown in Figs. 4.1(c)-4.1(d) are the results of the advection in streamwise direction and cross-stream swimming in the spanwise direction. Note that in the micro-channel (Fig. 4.1(b)), there is no flow velocity in the direction of swimming. This cross-stream

swimming in response to flow shear is robust and readily reproducible at any shear rate above the threshold.

In contrast to the quiescent flow, flow shear induces substantial changes in cell swimming kinematics, i.e. speed, cell body orientation and fore-aft axial rotation. In a quiescent flow, *Dunaliella* rotates about its fore-aft axis, owing to the asymmetric attachment of flagella (details in 5.3). With the onset of fluid flow shear, cells are noticeably irrotational and align themselves in the *y*-direction. Using high-speed microscopic observations at the magnification of 100× and 1K fps, we show that a cell performing cross-stream migration *does not rotate* along its long axis (Fig. 4.2(b)). Note that passive ellipsoidal particles immersed in a low shear flow are driven by the flow vorticity and undergo periodic rotation (Jeffery 1922). It is reasonable to expect that flow shear may weaken or strengthen the rate of rotation if cell swims in or against the local vorticity direction, respectively. However, we have only observed reduction in the rate of rotation. Additionally, we have also observed that swimming *Dunaliella* behave diametrically differently from the non-motile passive particles. We have performed the same shear flow experiments on the preserved (dead) *Dunaliella* and observed that non-motile cells do undergo characteristic periodic orbital motion, as predicted by Jeffery (25, Fig. 4.2(c), more details in 5.2.2). Hence, it is concluded that the cell motility plays a significant role in this aberrant shear response.

To examine the alignment of the cell to shear flow, we measured the azimuthal angle, θ, and zenith angle, ϕ, defined by the cell's fore-aft axis and mean flow direction (*x*-axis, Fig. 4.3(b)). The ϕ was estimated by the relation, $sin(\phi) = l_{img}/l_n$, where l_{img}

was the cell's fore-aft axial length measured from its projection on the in-focus image, and l_n was the nominal cell body length (~10 μm). The azimuthal angle was computed as the angle between l_{img} and the flow direction (*x*-axis). Probability Density Functions (PDFs) of θ and ϕ were obtained for all shear rates. For brevity, only distributions of θ for S=1 s^{-1} (dashed line) and 20 s^{-1} (dark line) are shown in Fig. 4.3(a). Additional distribution of ϕ for 20 s^{-1} is shown in Fig. 4.8. Note that the distributions are compiled over the entire sample volume in which *Dunaliella* experienced maximum shear near the wall and minimal shear at the center of the channel. In the flow where the maximum shear is below the critical rate, 10 s^{-1}, the distributions are shown to be uniform, whereas PDFs peak at the azimuthal angle of 90º in the presence of high shear, i.e. cells are aligned in the cross-stream direction (*y*-axis). The PDF of cross-stream migration velocity, *v*, of *Dunaliella* cells at a shear rate of 20 s^{-1} (left inset in Fig. 4.3(a)) with advection velocity removed over the entire sample volume, shows a tri-modal distribution. The central peak located at v=0±5 μm s^{-1} corresponds squarely to the spanwise velocity component associated with the cells advected by the flow in the low shear region (150 < z < 300 μm); whereas two side peaks (centered at ±40 μm s^{-1}) indicate the *y-axis* migration in two high shear regions close to the wall. Close inspection shows that the peak at -40 μm s^{-1} is produced solely by the cells swimming near the top wall. Similarly, the cells near the bottom wall are associated only with the peak at +40 μm s^{-1}. Consequently, these cells located in both regions contribute to the peak in the PDF of θ at 90º (Fig. 4.3(a)). The results are consistent with the abovementioned cross-stream migratory observations. To answer the question whether such a cross-stream

migration is a purely hydrodynamic interaction of *Dunaliella* and a solid wall, we explore the joint PDF of the azimuthal alignment with respect to the wall distance, z (right inset of Fig. 4.3(a)). Peaks of the joint PDF (indicated by red dark region) protrude substantially away from the channel walls, ~15 l_n. These protrusions maintained their shape as they move away from the wall, but quickly lose their integrity to the random orientation, i.e. uniform distribution marked by green (in the mid-section of the channel). The transition from directional alignment to random is rapid and occurs sharply at the distance where the flow shear drops below the critical value. Additionally, elucidated in Fig. 4.7, the cross-stream migration behavior emerges only after the flow shear exceeds 10 s^{-1} as evidenced by the tri-modal distributions of PDFs of the cross-stream velocity, v. Furthermore, the 2D high speed microscopic observations under higher shear conditions (Table 4.2) reveal that cross-stream migration can be observed at the plane sufficiently far away from the wall, z = 75~125 μm (7~15 l_n). At such distances, hydrodynamic forces due to the wall are expected to be weak and often negligible (Blake and Chwang 1974). These observations suggest that the cross-stream migration relate directly to the local flow shear.

Unlike a passive ellipsoid particle in a shear flow, motile *Dunaliella* cell remains irrotational. As shown in Fig. 4.2, a *Dunaliella* cell in a shear flow must beat its flagella to produce the necessary torque to balance the flow vorticity. To conceptualize a possible mechanism for such an action, we have developed a simple resistive force theory model to elucidate the generation of torque (shown in Figs. 4.3(b)-4.3(c)). Similar to live *Dunaliella*, model cell has two flagella, *cis*- and *trans*-flagellum sketched in Fig. 4.3(b)

as the left and right filament respectively. Both model flagella beat within a plane parallel to the fore-aft axis (*y*-axis) and are offset at a distance of d_{fg} to the center of mass. It is assumed that the beating patterns of these two flagella are identical and symmetric with respect to the *y*-axis. The high-speed measurements show that the *cis*-flagellum beats more rapidly than the *trans*-flagellum does, i.e. $\omega^{cis} > \omega^{trans}$, where ω is the beating frequency in radians and the superscript refers to the corresponding flagellum. To obtain the propulsive force on a beating flagellum at low Reynolds number limit, one can approximate this force with the drag exerted by the fluid motion relative to the filament (Gray and Hancock 1955). It is noted briefly here and proved rigorously in chapter 5 (5.4) that the magnitude of the net propulsive force on a flagellum increases linearly with its beating frequency. Consequently, the *cis*-flagellum that beats at higher frequency generates a larger propulsive force, $\langle F_p^{cis} \rangle$ (shown as a longer red arrow in Figs. 4.3(b)-4.3(c)) in comparison to the *trans*-flagellum. Since the direction of a propulsive force is determined solely by its beating patterns (chapter 5), the corresponding beating patterns by the *cis*- and *trans*-flagellum limit the directions of $\langle F_p^{cis} \rangle$ and $\langle F_p^{trans} \rangle$ to be symmetric with respect to the cell fore-aft axis. The axial component of $\langle F_p^{cis} \rangle$ and $\langle F_p^{trans} \rangle$ parallel to the swimming direction must balance the total drag force, $\overrightarrow{F_D}$, on the cell body. On the other hand, the normal components (longer red arrows in Fig. 4.3(c)) remain unbalanced and consequently produce a force normal to the fore-aft axis. Since it is located in a plane that is offset at d_{fg} away from the center of rotation, this force produces a counter clockwise (CCW) torque that causes the cell to rotate in CCW in a quiescent flow when viewed from the rear (Fig. 4.3(b)). In a planar shear flow above the critical shear rate,

Dunaliella responds to shear by reorienting and swimming in the direction (*y*-axis) normal to the shear plane (*x*-*z*). The same torque by the beating flagella counteracts the viscous moment by the flow shear and prevents the cell from rotating in a shear flow. Illustrated in Fig. 4.3(c), since a drag force is also present on the flagellum in addition to the propulsive force, to generate the CCW torque in a shear flow, the net propulsive force, $\vec{F}_p^{cis} - \vec{F}_p^{trans}$, normal to the fore-aft axis must exceed the total drag force on the flagella, $\vec{F}_{df}^{cis} + \vec{F}_{df}^{trans}$. This relationship provides us with a criterion that determines the minimum frequency difference between *cis*- and *trans*-flagellum necessary to allow *Dunaliella* to maintain irrotationality in a shear flow while migrating cross-stream. The criterion is provided briefly here as $\Delta f_{min} \geq S\left(\frac{2d_{fg}}{l_f}\right)C$ and more details in chapter 5, where S is the flow shear, l_f is the length of each flagellum, and C is a coefficient that depends only on the kinematics of the beating flagella. The criterion is simple but descriptive and provides us with the lower bound. We validate this criterion against the experimental observations. For instance, assuming a beating pattern like translating rods and using physiologically relevant parameters, i.e., flagellum length, l_f = 12 μm, offset distance, d_{fg} = 0.5 μm and a shear rate of 20 s^{-1}, the minimum frequency difference, Δf_{min}, is estimated as 2.9 Hz. The predicted value is well below experimentally observed frequency difference of 7 Hz, i.e. the beating frequency of 30 Hz for the *trans* and of 37 Hz for the *cis*-flagellum. Additional discussions are provided in chapter 5. Note that this model describes one of *possible* mechanisms that may explain the two primary experimental observations: (i) In the presence of flow shear above a critical value, motile

Dunaliella reorients itself and swims in the direction of local flow vorticity; and (ii) *Dunaliella* is capable of maintaining the cell body irrotational in a shear flow, whereas in quiescent fluid, it rotates about its fore-aft axis while swimming forward. The other possible mechanisms may include but are not limited to: both flagella beat in three dimensions and are not confined within a single 2D plane, or *trans*- and *cis*-flagella could beat in different planes. To discern which mechanism is involved, our observations may not be sufficient to explain the full scope. Further research will be needed.

To assess the implications of the aforementioned shear-induced response for large-scale biophysical processes, we compute both isotropic and anisotropic dispersion coefficients (SI in Sheng et al. 2010, Figs. 4.4(a) and 4.4(b)). To determine the swimming induced dispersion coefficients (D_{ii}, $i = x, y, z$), we apply the Lagrangian description of diffusion, which has been introduced by Taylor (1921) to determine the dispersion rate of a scalar in stationary, homogeneous, and isotropic turbulence, subsequently extended by Csanady (1963) to suspended particles, and employed to swimming micro-organisms by Sheng *et al.* (2010). It is shown that the dispersion coefficient can be calculated by integrating the autocorrelation function, $R_{ii}(\tau)$, of the Lagrangian velocity components along the particle trajectory, i.e.,

$$D_{ii}(t) = \int_0^t R_{ii}(\tau)\, d\tau = \int_{\tau=0}^{t} \int_{\eta=0}^{\infty} u_i(\eta)\; u_i(\eta+\tau)\, d\eta\, d\tau \qquad (1)$$

where τ is the time lag, u is the fluctuation component of *Dunaliella* swimming velocity, and the subscript i refers to a direction, x, y or z. Due to the limited spatial extent of essentially all velocity measurement, the dispersion coefficient is ensemble averaged over

many microalgal trajectories with a finite length as,

$$D_{ii}(t) = \langle \int_0^t d\tau \int_0^\tau R_{ii}(\eta)\, d\eta \rangle = \int_0^t d\tau \int_0^\tau \langle R_{ii}(\eta) \rangle \, d\eta \qquad (2)$$

where $\langle \ \rangle$ denotes ensemble averaging performed over trajectories of *Dunaliella*. The asymptotic value of $D_{ii}(\tau)$, as $\tau \to \infty$, yields the Fickian dispersion coefficient. The isotropic dispersion, *D*, is estimated by averaging the coefficient, $D = \frac{1}{3}(D_{xx} + D_{yy} + D_{zz})$. The subsequent anisotropic dispersion rate is computed by $A_{ii} = \left(\frac{D_{ii}}{D}\right) - 1$. The value of A_{ii} indicates the extent of anisotropicity in the i-th direction. A positive A_{ii} suggests that in the i-th direction *Dunaliella* disperse faster than the isotropic rate. To elucidate visually the effects of the abovementioned cross-stream migration on dispersion, we have plotted swimming trajectories at two flow conditions (S = 0 s^{-1} and S = 20 s^{-1}) (Fig. 4.4(c)). Each trajectory is made to originate from the same point and color-coded by the time as *Dunaliella* disperses. The suspension disperses less in the presence of low flow shear than it does in quiescent fluid, whereas the dispersion increases "exponentially" as shear is increased. The initial reduction in dispersion are consistent with the observations by Chengala et al (2010) that *Dunaliella* reduce the swimming velocity while acclimatizing to the low shear flow conditions. Further, the disparity among the components of anisotropic dispersion tensor shows the structural change of the suspension as it diffuses. At no or low shear (S < 5 s^{-1}), suspension diffuses nearly uniformly in all directions (Top in Fig. 4.4(c)). In the regime, 5< S < 10 s^{-1}, *Dunaliella* prefer to swim axisymmetrically in the direction of mean flow. As the shear increases to induce the aforementioned response, the population disperses in a 2D plane perpendicular to shear (bottom in Fig. 4.4(c)).

4.4 Summary and Conclusion

We observe that a green alga, *D. primolecta*, aligns and swims in a preferred direction at the flow shear above the critical rate of 10 s^{-1}. The resultant swimming direction is perpendicular to the shear plane (*x*-*z*) and in-line with local vorticity (*y*-axis), and is substantially different from that of gyrotaxis: a phenomenon occurring due to asymmetric distribution of cell mass or bottom heaviness, where the cells reorient by the subtle balances between gravitation and viscous torques. The cells must swim vertically and the plane of shear must align vertically. In contrast, in our quiescent flow experiments, *D. primolecta* swim in random directions, which are evident in PDFs of cell orientations (Fig. 4.3(a)) and 3D trajectories (Fig. 4.1(a), Fig. 4.4(c)). In high shear experiments, we observe that *Dunaliella* prefers swimming on horizontal planes (*x*-*y* planes) normal to the shear (*x*-*z*). It is evident in the PDF distribution shown in Fig. 4.8 for zenith angle, ϕ, compiled over 1000 sample tracks where the PDF peaks at $\cos(\phi) = 0^{o}$ or $\phi = 90^{o}$. In contrast to the motion of an elongated passive particle in a shear flow, the cell body of *Dunaliella* remains irrotational. This active shear-induced response results in a substantial change in spatial heterogeneity of microalgal suspension, forming what appears to be a 2D thin dispersion layer. Note that the *y*-axis overlaps with the intermediate strain of a planar shear in which direction cells experience the least net stress on the membrane. The discovery motivates an interesting paradigm to harvest microalgae at large scales from diluted bioreactors by manipulating hydrodynamic cues. Microalgal biomass separation from dilute suspensions is one of the highest energy costs associated with biofuels and human nutrition production. The observed shear-induced

swimming provides additional insights into the mechanisms and processes that mediate the formation, maintenance, and dispersion of microalgal thin layers in lakes and oceans.

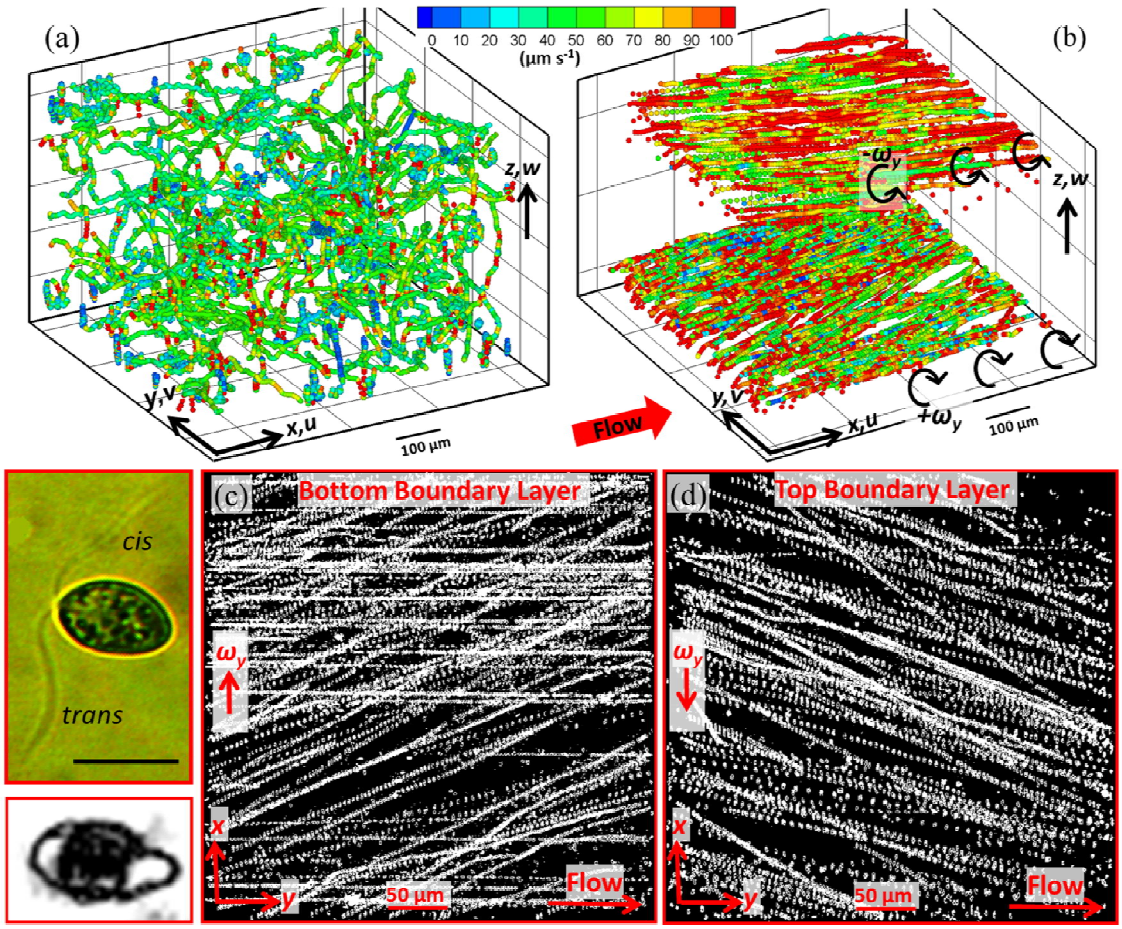

Fig. 4.1. 3D swimming trajectories of *D. primolecta* (a) in a quiescent fluid, (b) in shear flow of $S = 20\ s^{-1}$. *x*: streamwise and mean flow direction, *y*: spanwise and the intermediate strain direction of a planar shear flow. Local vorticity aligns in the positive *y* axis within the bottom boundary layer and in the negative *y* axis within the top boundary layer. *z*: the wall normal direction. The cells in the mid-section of channel are advected (they appear as straight lines) and are removed to make the viewing clear. The velocity components in the corresponding direction are denoted as *u*, *v*, and *w*. A straight micro-channel with the rectangular cross-section of $0.42 \times 3.5\ mm^2$ is used for visualization. The trajectories are color coded by the magnitude of swimming velocity. Superimposed in-focus images of individual *Dunaliella* subjected to the high flow shear located in (c) bottom and (d) top boundary layers. Local vorticity is marked with an arrow separately. Inset - Top: Optical microscopic image, Bottom: In-focus digital holographic image of *D. primolecta*. Scale: 10 μm. Note: The diagonal trajectories shown in Figs. 4.1(c)-4.1(d) are the results of the streamwise flow advection and cross-stream swimming in spanwise.

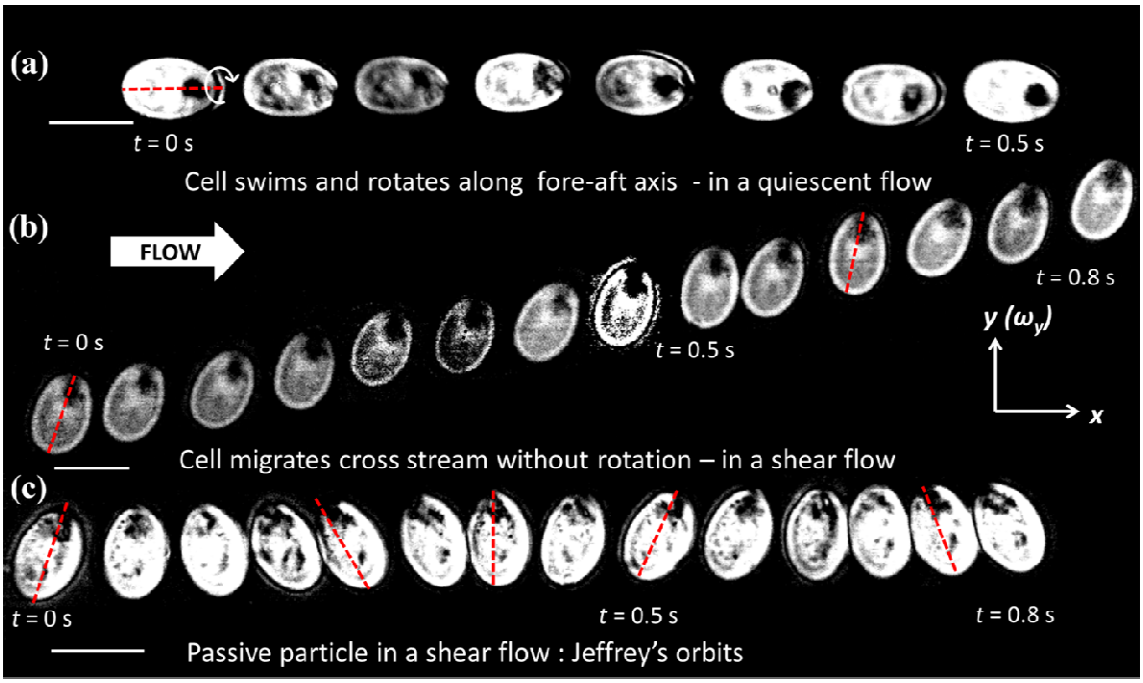

Fig. 4.2. Sample of time sequences (only shown for every 63 frames): motile cell swims (a) in a quiescent fluid; (b) in a shear flow of $S = 20\ s^{-1}$. In a quiescent flow, cell body rotates counter clockwise about 2Hz when viewed from the rear. Rotation direction is indicated by the position of the cell nucleus with nucleolus (dark spots on the front side of the cell). In a shear flow, the cell remains irrotational and swims perpendicular to the mean flow (y-axis). (c) Non-motile cell (fixed with 4% formaldehyde) in a shear flow undergoes periodic motion. Scale: 10 µm. The figure elucidates the rotationality/non-rotationality of the cell in different fluid flow conditions. The x positions of the cell in Fig. 4.2(b) are, however, manually arranged closer to each other.

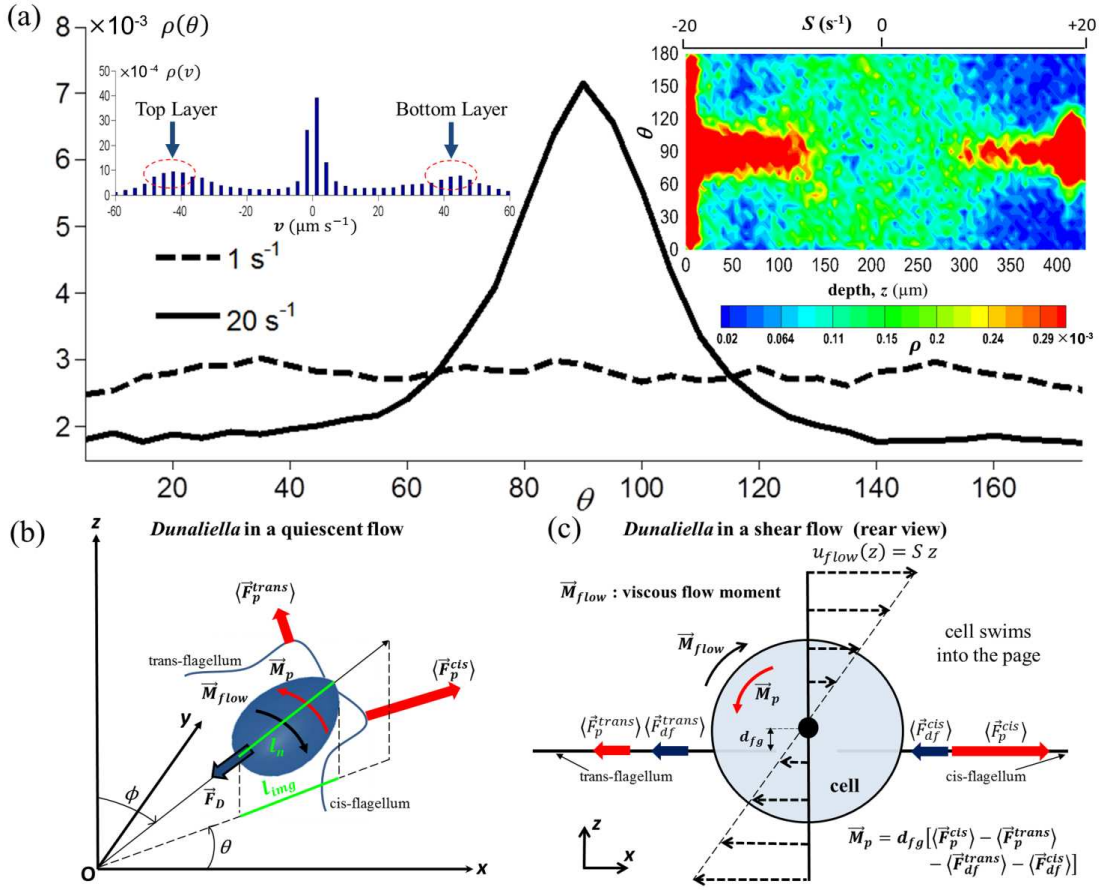

Fig. 4.3. (a) PDFs of cell alignment in a shear flow. The alignment is defined as the angle between the cell's fore-aft axis and the mean flow direction, *x*. Insets: Left - histogram of spanwise swimming velocity, Right - Joint PDF of θ (azimuth angle) with respect to varying micro-channel depth, and consequently flow shear. (b) Schematics of cell alignment in a flow: θ (azimuth angle) varies from 0 -180º and θ = 90º represents the direction perpendicular to the flow and the direction of local vorticity. ϕ represents the zenith angle. (c) Hydrodynamic model of the cell in a shear flow: viscous torque by the flow is balanced by that produced by the flagella.

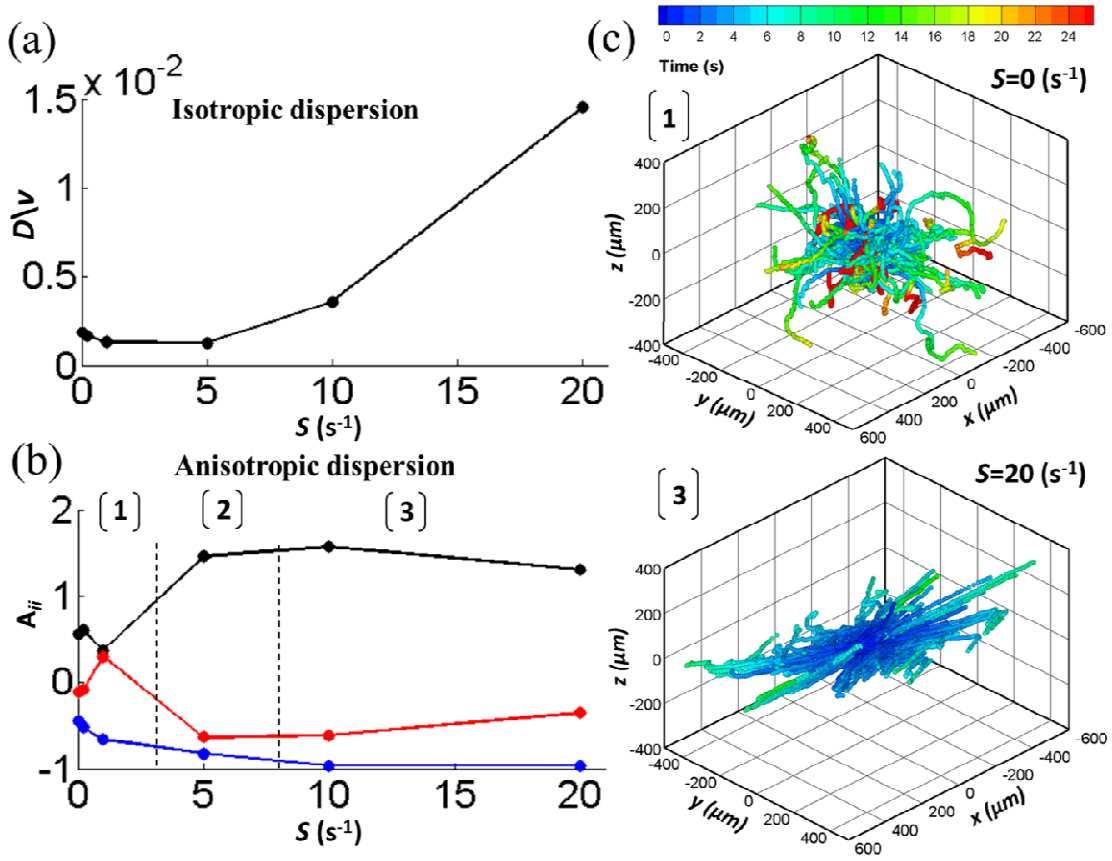

Fig. 4.4. Swimming induced dispersion (a) Isotropic dispersion coefficient, – , normalized by kinematic viscosity, ν. An average error is estimated at 0.3 × 10^{-2} μm^2 s^{-1} (b) Anisotropic dispersion tensor, — Symbols: Black - , Red - , Blue - . The error: 0.3, 0.2, and 0.15 μm^2 s^{-1} for , and , respectively. (c) 3D elucidation of the cell dispersion pattern using Lagrangian trajectories. All trajectories are made to originate from the same point. Top: a quiescent flow; Bottom: a shear flow of 20 s^{-1}. Color: time elapsed.

4.5 Supplemental Information

This supplemental provides additional information on materials and methods, and additional observed cell kinematics.

4.5.1 Cell Culture

Dunaliella primolecta was obtained from the Culture Collection of Algae at the University of Texas at Austin (UTEX LB1000). The algae were grown in the modified Johnson's medium (Olmos et al. 2000) in a diurnal (14 hr light – 10 hr dark cycle) growth chamber that was maintained at 20^{o} C. The cultures were shaken by hand once a day and were allowed to reach the mid-log growth phase. A sample suspension at about 2×10^{6} cells mL^{-1} was prepared for motility experiments 10 days after the inoculation. The cell count was performed using a Haemocytometer counting chamber. The suspension without dilution was injected directly into the microfluidics channel with the dimensions of $35 \times 3.5 \times 0.42$ mm^{3} in *x*, *y* and *z* directions respectively. Additionally, fixed (dead) cells suspensions were used to provide observations on the kinematics of the individual particles when exposed to fluid flow shear.

4.5.2 Cell Fixation

A 100 mL suspension containing live microalgal cells was mixed with 4 mL of 4% formaldehyde solution in Phosphate Buffered Saline (PBS). Formaldehyde fixes tissue by cross-linking the proteins, primarily the residues of the basic amino acid lysine but preserves the cell morphology. The suspension remained in solution for approximately

10-15 min. The sample was then centrifuged for 10 min at 1500 revolutions per minute (×228 g), the supernatant was decanted and the pellets re-suspended in the PBS. The cells were “washed” twice and re-suspended in fresh media for microscopic observations.

4.5.3 Microfluidics and Digital Holographic Microscopy

Measurements were performed using in-line, cinematic (15 fps) digital holographic microscopy (Sheng et al. 2006, 2007, 2008, 2010). The optical setup is similar to that described in Sheng *et al.* 2010, but incorporated the holographic microscopy technique into a permanent inverted light microscope (Nikon TS-100). Holographic microscopic images were recorded via a Nikon inverted microscope at the magnification of 20× (Super Plan Fluor 20×). The original holograms were recorded by a 2K × 2K CCD camera (Imperx 4M15L) and were streamed continuously at the rate of 15 fps to a data acquisition computer. Each time sequence consisted of over three minute recording, totaling 1000 holograms per sequence. Digital reconstruction and analysis using in-house developed software enabled simultaneous tracking of thousands of particle traces. Trajectory parameters including velocity, size and shape of particles as well as motility statistics were subsequently computed (Sheng et al. 2007). The stationary particles were removed at the bottom of the micro-channel by subtracting each hologram with a time averaged hologram, in which the stationary particles form clear interference patterns. Fig. 4.6 shows the overlapped in-focus images of *Dunaliella* cells over the entire depth of microfluidic channel. The suspension was injected by a computer-controlled syringe pump to generate different shear rates in the micro-channel. The 3D distributions of flow velocity were measured directly by recording holograms of tracer particles (Polystyrene

particles with a diameter of 2.9 μm) at the given flow rates. The velocities were obtained by applying PIV analysis to holographic images at a given depth. These images contain only the particle displacement within a corresponding layer of 5μm thickness. Fig. 4.7 shows the stream-wise fluid flow velocities (u_{flow}) at different shear rates. Dots represent the experimental Poiseuille flow bounded by a rectangular geometry. The analytical solution for the streamwise velocity component, u, is given by

$$u(x,y) = \frac{Q}{C_p} \times \sum_{n=1,3,5....}^{\infty} \frac{1}{n^3}\left(1 - \frac{\cosh(n\pi\, x/h)}{\cosh(n\pi\, \gamma/2)}\right)\sin(n\pi\, y/h), \quad (3)$$

where $C_p = \sum_{n=1,3,5....}^{\infty} \frac{2h^2}{\pi n^4} \times \left(\gamma - \frac{2}{n\pi}\sinh(n\pi\, \gamma/2)\right)$ and $\gamma = w / h$, Q is the flow rate, h is the depth, and w is the width of the micro-channel. The measurement agrees well with the theoretical analysis (Fig. 4.7). The sample was discarded after each run through the micro-channel and fresh suspension was prepared using the original batch culture. Table 4.1 provides experimental flow conditions used for the shear response of live *D. primolecta*. For low shear rate experiments, data were recorded 5 minutes after the initiation of flow pump. The delay time is approximately the time it took to set up a steady flow in the micro-channel.

4.5.4 High-Speed Microscopic Experiments

To determine the kinematics of the rotational motion of the cell body, the high-speed visualization experiments were conducted using phase contrast microscopy at the magnification of 100×. A second micro-channel was constructed to provide high magnification observations. The micro-channel was machined out of a 400 μm thick

silicon shim (McMaster-Carr, CA) and sandwiched between a glass slide and a thin cover slip (100 μm). All components were glued using epoxy resin. Two 1 mm ports were laser machined, connected with tubing and sealed with epoxy. During the experiments, the micro-channel was inverted, i.e. with the cover slip facing the objective, allowing the optical access of a high-magnification oil-immersion objective (100×, WD = 0.17 mm). The observations at different shear rates were conducted at the fixed plane with a distance of 50~125 μm away from the bottom channel wall by varying the flow rate using a computer-controlled syringe pump, subsequently changing the maximum shear rate close to the cover slip. A high speed CMOS camera (IDT N4) was used to image the kinematics of both the beating flagella and the cell body at 1000 frame per second. The rotation of the cell body was elucidated by the position of nucleolus with nucleus (dark spot on the front part of cell body that can be seen in Fig. 4.2). The angular velocity was approximated by manually identifying the periods of nucleolus in the video image sequences. The kinematics of the beating flagellum, i.e. beating frequency, amplitude, wavelength, was also determined manually from the sequences and still images. The experiments were conducted in both quiescent and various shear flow conditions, with the maximum shear rate reaching 200 s^{-1} (Table 4.2). Both live and fixed cells were used for comparison.

In a quiescent flow, *Dunaliella* swims in random directions and rotates counter clockwise (~2 Hz) about the fore-aft axis viewed from the rear. The statistics of cell body rotation is determined by visualizing the position of the nucleolus within nucleus. The results are consistent with the observation by Schoevaert *et al.* 1988. However, in a shear

flow, cells that migrate in the cross-stream direction cease to rotate along the cell's axis but these cells beat their flagella asynchronously with slips of synchrony. Dead cells in a shear flow, though, has the same motions as the elongated passive ellipsoids, i.e. periodic tumbling with closed orbits, (Jeffery 1921, Fig. 2(c)).

4.5.5 Evidence of Flow Shear in Triggering Cross-Stream Migration

Table 4.2 provides the experimental observations that highlight the external flow conditions needed to trigger the robust cross-stream migration. These experiments are conducted in a 420 μm microfluidic channel. As described in 4.5.3 and 4.5.4, two techniques: 3D holographic microscopy and 2D high-speed microscopy, are employed. Quantitative 3D kinematics measurements of a volumetric suspension are performed using 3D holography. The holographic experiments cover the shear flows with the maximum shear rate, S, of 0, 0.1, 1, 5, 10, and 20 s^{-1}. Different shear rates are achieved by altering the flow rate. Volumetric 3D trajectories are obtained for each shear condition (Fig. 4.8, Fig. 4.9). In Fig. 4.8, for all shear flows, the images in different planes along the depth are embedded onto one selected plane and are color coded to obtain trajectories of *Dunaliella* cells. In Fig. 4.9, 3D trajectories of *Dunaliella* are displayed. It can be observed that the shear induced response is evident slightly at S=10 s^{-1} and distinctly at S=20 s^{-1}. At S = 1 s^{-1} and S = 5 s^{-1}, cells seem to be advected by the flow. Random walk trajectories can be observed at S = 0 s^{-1} and S = 0.2 s^{-1}. Statistics of the cross-stream velocity, v, of *Dunaliella* are computed using this 3D data set and shown in Fig. 4.10. It is observed that as long as the flow shear, S, is below 10 s^{-1}, PDFs are symmetric and peaks

at v = 0 µm/s. As the flow shear exceeds the critical value, 10 s^{-1}, tri-modal distribution emerges and the trend accentuates with the increasing shear. As discussed in the paper, the two side-peaks correspond to the cross-stream migration in two high shear regions (close to the walls). Experiments under the high shear conditions, i.e., S = 50 – 200 s^{-1}, are conducted using 2D high speed microscopy. When the large number of swimming cells (> 100) migrates in the direction of local vorticity, the collective behavior is deemed to be "observed". Since this behavior is very unique, one will not mistake the migration with the others. The plane of observation is located at the distance of z = 75~125 µm to the bottom wall (details in Table 4.2, column 3). Since the hydrodynamic forces or effects due to the presence of a wall decay rapidly with the distance from the wall, (i.e., it scales inversely to the power of the distance), wall effect may be considered negligible at the observation plane.

4.5.6. Distribution of Cell Orientation

Additional information on the distribution of cell's zenith angle (ϕ) was generated from the in-focus holographic images. In a shear flow (S = 20 s^{-1}), the cells were predominantly oriented at $\cos(\phi) = 0^{o}$ or ϕ = 90º (Fig. 4.11). This provides additional evidence that cells are unambiguously swimming in the cross-stream direction. The majority of cells swim on horizontal planes (x-y) normal to the shear flow (x-z plane).

Table 4.1 Maximum velocities and corresponding maximum shear rate for each experimental condition. The 3rd column represents the number of tracks obtained during the experiment.

u_{max} (μm/s)	*du/dz* (1/s)	No. of tracks obvserved	Cell density 10^6 (cell/mL)
No flow	0	283	
17	0.15	267	
100	1	767	2.04
500	5	954	
1000	10	1303	
2120	20	1325	

Table 4.2. High speed microscopic observation of shear-induced response under various shear rates at planes of observations from the bottom of the micro-channel. The depth of micro-channel is 420 μm.

Maximum Shear rate du/dz (s^{-1})	**Measurements** (Volumetric or Planar)	**Plane of observation to the wall,** z (μm)	**Shear rate at plane(s) of observation,** S (s^{-1})	**Shear Response**	
				Yes	**No**
0	Volumetric	0-420	0		X
0.2	Volumetric	0-420	-0.2 – 0.2		X
1	Volumetric	0-420	-1 – 1		X
5	Volumetric	0-420	-5 – 5		X
10	Volumetric	0-420	-10 – 10	X	
20	Volumetric	0-420	-20 – 20	X	
50	Planar	125	21	X	
60	Planar	125	25	X	
75	Planar	75	50	X	
100	Planar	100	55	X	
160	Planar	125	70	X	
200	Planar	100	110	X	

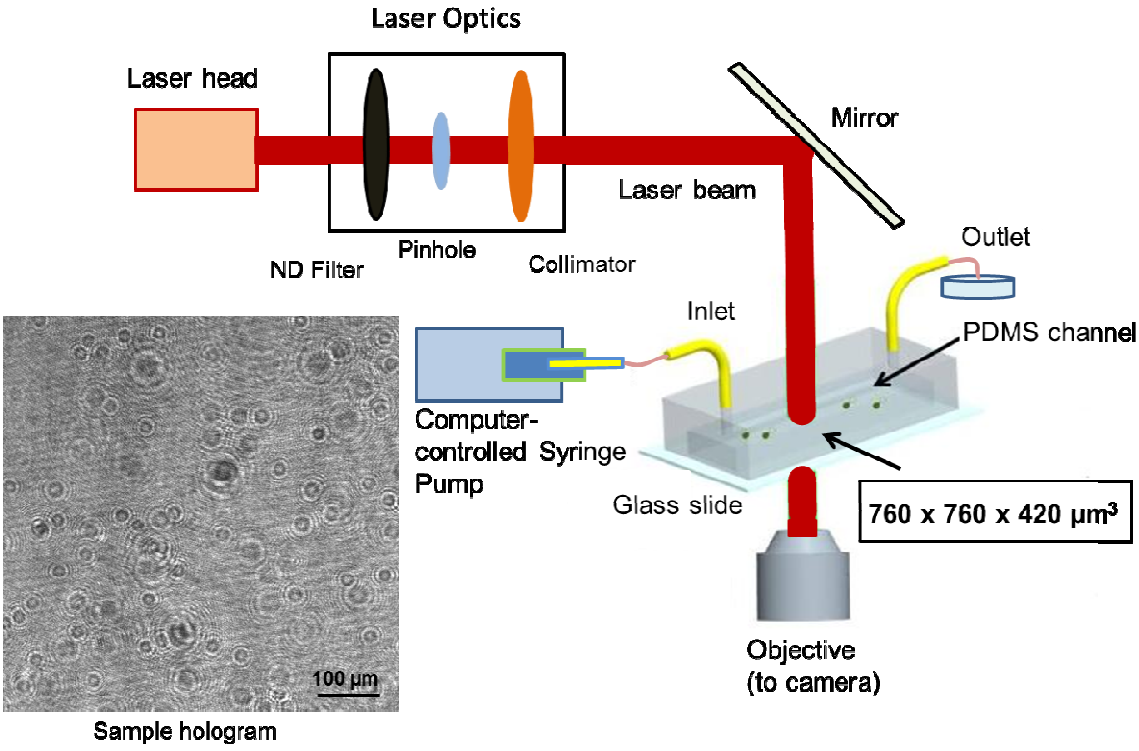

Fig. 4.5. Experimental set-up. Inset: A sample hologram.

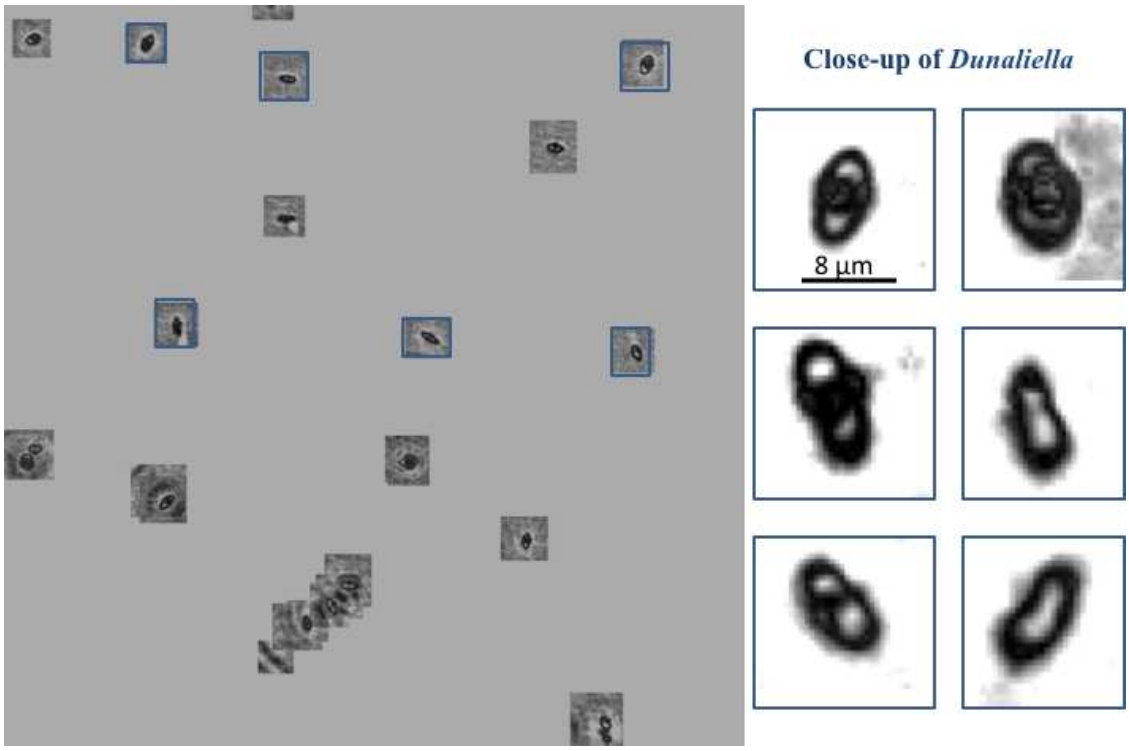

Fig. 4.6. Overlapped in-focus images of *Dunaliella* over the entire depth of micro-channel.

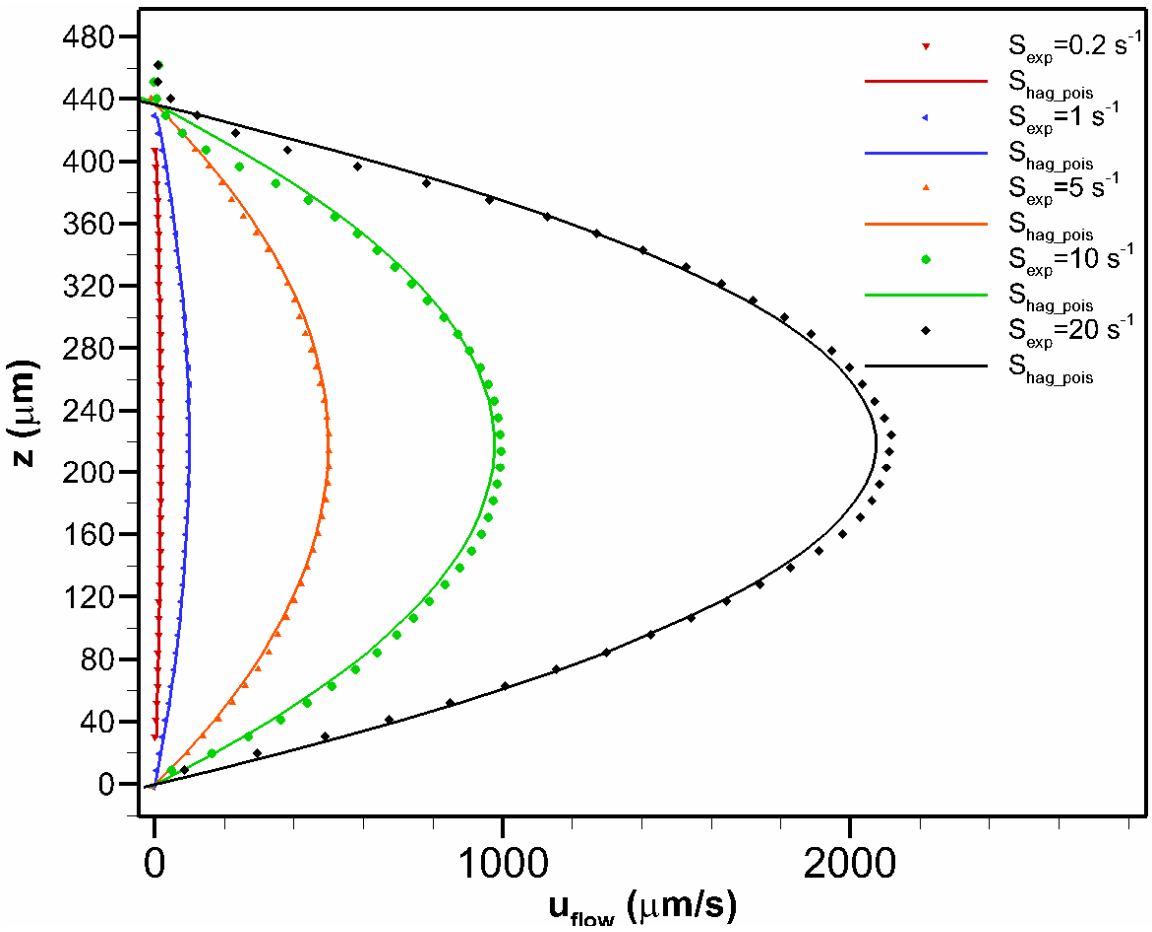

Fig. 4.7. Streamwise velocity component, *u* distribution at various shear rates along the micro-channel of depth, z. Dots represent the experimental measurements and the solid lines represent the analytical solution of Poiseuille flow within the rectangular channel.

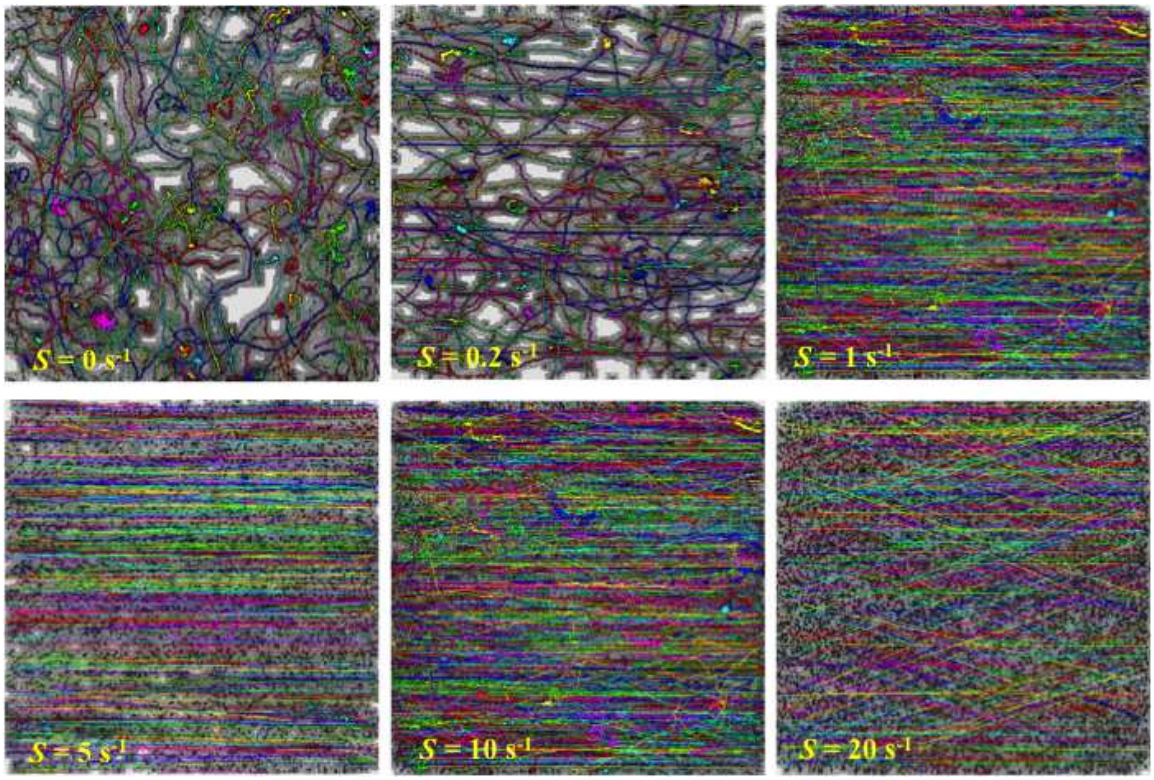

Fig. 4.8. Images of *Dunaliella* tracks imbedded on to one z-plane at different shear rates.

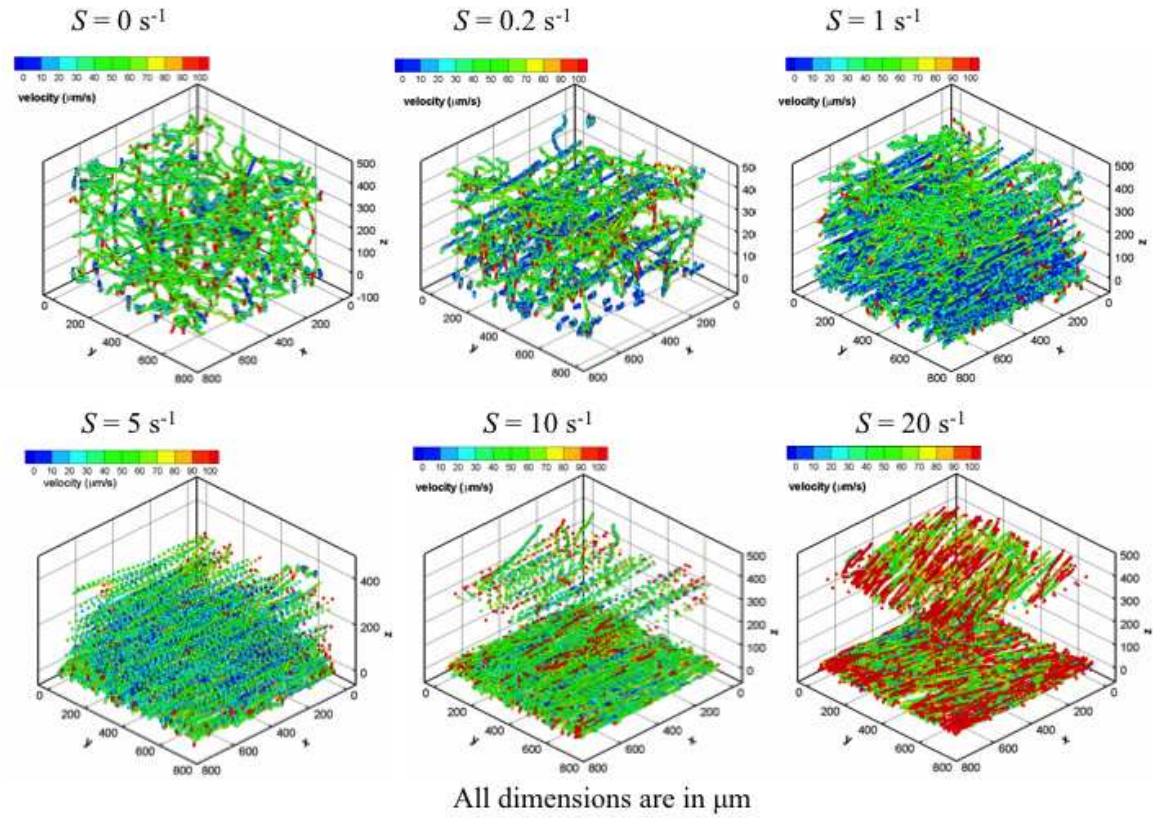

Fig. 4.9. Comparison of the trajectories of *Dunaliella* under different shear rates.

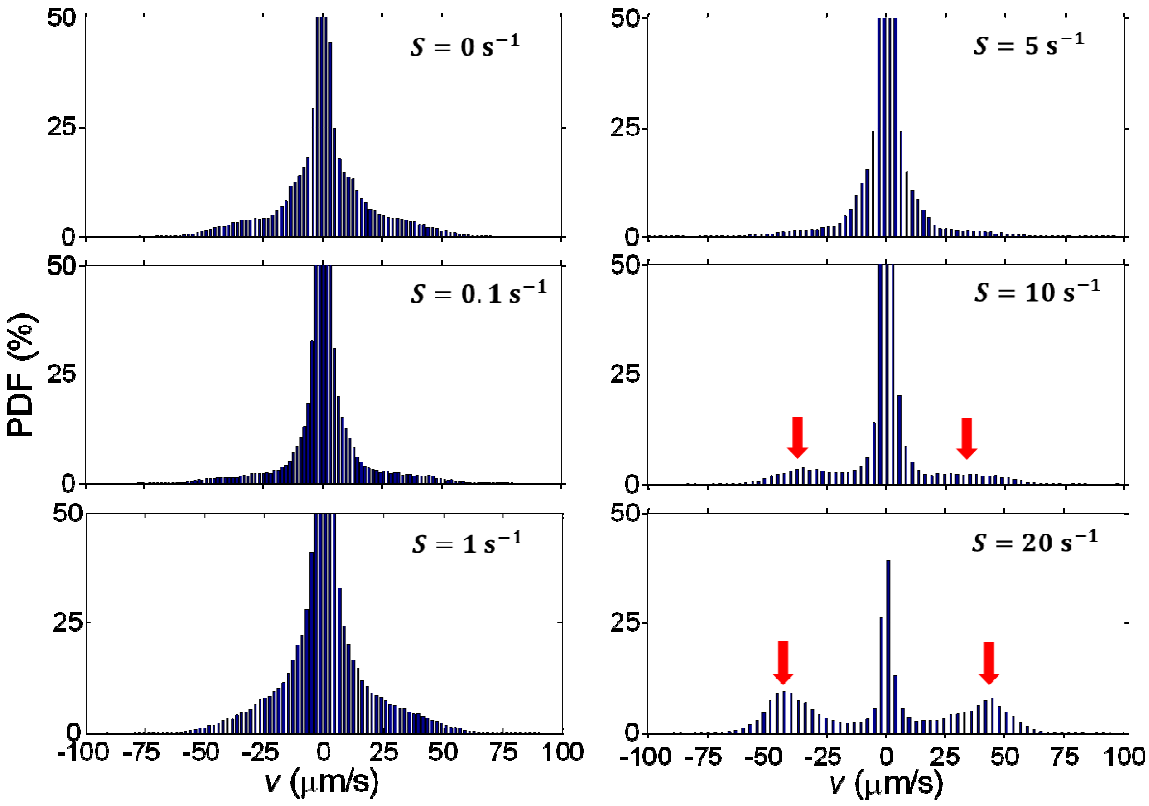

Fig. 4.10. PDFs of the cross-stream velocity, *v*, of *Dunaliella* at different flow shear, *S*. Each PDF is computed over a volumetric measurement of 3D trajectories using Digital Holographic Microscopy. The maximum shear rate for each measurement is indicated on the top-right corner of the panel. 3D measurements are performed over the shear rate of 0, 0.1, 1, 5, 10, and 20 s^{-1}.

Fig. 4.11. The distribution of zenith angle, ϕ, at S= 20 s^{-1} compiled over 1000 sample tracks. The peak is found at $cos(\phi)$ = 0º or ϕ = 90º.

Chapter 5

Numerical Model Development of a Swimming *Dunaliella primolecta*

Published (most part) as supplemental material for: Chengala, A., M. Hondzo, and J. Sheng. 2013. Microalga propels along vorticity direction in a shear flow. Phys. Rev. E. 87:052704, doi: 10.1103/PhysRevE.87.052704.

We investigated the swimming behavior of microalga, *Dunaliella primolecta* Butcher, having spheroidal bodies with two flagella located at the anterior part of the cell that uses breast-like motion for its propulsion. The direction of cell swimming is random in a quiescent flow, while, in a unidirectional shear flow, the cell displays a unique behavior of propelling along the local vorticity direction. The cell rotation is absent during this propulsion in the shear flow and the flagella beating are observed to be asynchronous. A physical model is developed using the Resistive Force Theory (RFT) that is based on our assertion that the flagella kinetics is the key to the question why motile cell remain irrotational in a shear flow. We demonstrate that the moments generated by beating flagella and their alignment to flow are necessary to counter-act the vorticity of the shear flow. The model incorporates the key ingredient of the flagella kinematics including, the asynchronous beating between the *cis*- and the *trans*-flagellum. The forces and the moments generated by the flagella in a shear and the quiescent flow are estimated numerically.

5.1 Introduction

A complete swimming dynamics of the motile characteristics of bi-flagellates such as *Dunaliella*, that generate thrust from the anterior part of the cell have been scarcely documented. Motility augments the formation of algal cell aggregations or dispersions that are often associated with ecological and economic ramifications (Durham et al. 2009; Bearon et al. 2004). Cell motility is required for many important physiological processes during development, such as cell migration during gastrulation, tissue regeneration and embryological development (Polin et al. 2009). Additionally, motility studies aim at understanding the reasons for selecting a particular swimming style by micro-organism, the thrust generated through the dynamic body-fluid interactions and how the central nervous system controls the motion through sensory feedback (Ishikawa 2009). Different types of cells use a variety of strategies to seek food, produce energy, avoid death and fulfill different roles during their lifetime. In a viscous fluid environment, cell motility affects many biological processes, including reproduction, infection and the marine life ecosystem (Lauga and Powers 2009; Horwitz and Parsons 1999).

Dunaliella uses *flagella* for motility. Flagella are whip-like appendages that protrude from the cell body and are highly conserved organelles of cell locomotion for most of the algal species that are capable of motility. The coordinated motion of a group of flagella play an important role in many aspects of life, from fluid transport in the reproductive system and the respiratory tract, to mechanical and biochemical signal transduction in the kidneys and eyes (Polin et al. 2009). The flagellar apparatus is a complex organelle of great structural diversity that senses the mechanical, chemical,

gravitational and light stimulation of the cell (Melkonian 1982). Flagella also play an important role during sexual fusion of the cell. Flagella are comprised of several hundred proteins that are assembled using the equally conserved mechanism called the intraflagellar transport. The flagellar beat frequency and flagellar waveforms, which are the two main features of flagellar bending are generated by the functions of the outer and inner dynein arms. The motion of flagella is also involved in intercellular communication and pathogenesis (Drescher et al. 2010). Therefore, it is important to explore and mechanistically explain the dynamics of flagellum during cell locomotion.

5.1.1 Cell Composition

The cell body of *Dunaliella* is composed of a single cup-, dish-, or bell-shaped chloroplast, a pyrenoid basal with continuous starch shell, the eyespot, vacuoles, and nucleus with nucleolus that can be seen at the anterior part of the cell. Cells are mostly radially symmetrical, flattened, dorsoventrally curved or slightly asymmetrical. The general shape of the cell can be seen as ellipsoidal (Fig. 5.1A), ovoid, cylindrical, pyriform, or fusiform to almost spherical. The cell size and shape, though, may vary depending on different environmental conditions and stages of growth cycle. The cell surface is smooth with distinctive mucilaginous cell coat and the cell wall is absent. The division is usually by asexual reproduction by longitudinal division of vegetative flagellate cells (Preisig 1992).

5.1.2 Flagellum Structure

A flagellum is structurally complex, containing more than 250 types of proteins (Fig. 5.1B). Each flagellum consists of a non-rigid axoneme, or cylinder, with nine outer pairs of microtubules surrounding two central microtubules known as a '9 + 2' structure (Omoto et al. 1999). A membrane, sometimes beset by hairs or scales, surrounds the axoneme. The outer pairs of microtubules are connected to the axoneme by a protein called Nexin. Each of the nine outer pairs of microtubules has an "*a*" tubule and a "*b*" tubule. The *a* tubule has numerous molecules of a protein called dynein that are attached along its length which helps in bending. The dynein molecules are located along the length of the complete microtubule and extend 'arms' out to the adjacent partial microtubule. The molecules then climb along the partial microtubule, which produces a shear force that is converted to bending. The flexibility of the microtubules allows flagella to bend in a whip like motion, which is a critical factor in cell motility (O'Malley 2011).

5.1.3 Beating Pattern of the Flagellum

The flagella are named as *cis* and *trans* depending on their position relative to the eyespot. The *cis* flagellum is closer to the eyespot and is represented as the right side flagellum in Fig. 5.1B. The *trans* flagellum is relatively farther to the eyespot and is represented as the left side flagellum in Fig. 5.1B. The beating has two aspects: forward stroke (power or effective stroke) and backward stroke (recovery stroke). During forward stroke, the cells gain positive displacement as the flagella move toward the posterior end of the cell but they are restored to their initial position during the recovery stroke. During the recovery stroke, the flagella move close to the cell body and the result is that cell

movement is less in the recovery stroke than during the forward stroke. The bends resembling a “sine wave” can be observed along the length of the flagellum during both the forward and the recovery strokes. The two strokes are not distinct from one another since the recovery stroke begins at the base of the flagellum before the effective stroke has finished. Similarly it is observed that the effective stroke begins before the end of the recovery stroke. Further, a close inspection reveals that the flagellar beat is asynchronous with a periodic slip of synchrony, contrary to the earlier published reports (Schoevaert et al. 1988) that state that the flagellar beating is always synchronous. Schoevaert et al. 1988 also show that the frequency of *cis* flagellum beating is observed to be 60 Hz and that of the *trans*-flagellum is observed to be 50 Hz with 300 Hz recorded camera. In a quiescent flow, the cell rotates counter clockwise (~2Hz) about the fore-aft axis viewed from the rear of the cell body (Vismara et al. 2004).

5.1.4 Motivation for Numerical Model Development

Based on data presented in chapter 4, we proposed that: In a shear flow above a critical value, motile *Dunaliella* reorients itself and swims in the direction of local flow vorticity (Fig. 5.2). *Dunaliella* is capable of maintaining the cell body irrotational while displaying this behavior in the shear flow, whereas in a quiescent flow, it rotates about its fore-aft axis while swimming forward. We provide additional evidence below that the observed unique swimming of *Dunaliella* in a unidirectional shear flow is entirely controlled by the fluid flow shear.

Evidence: ***Cross-stream swimming orientation of Dunaliella was in the direction of local fluid flow vorticity and was concentrated in a horizontal plane with $S > 10\ s^{-1}$.***

Explanation: Fig. 5.3 depicts the concentration of cells in a low shear up to 0.2 s^{-1} (Fig 5.3A) and in a shear flow up to S = 20 s^{-1} (Fig 5.3B) in a micro-fluidic channel. The azimuth angle, ϕ, refers the angle between the vertical (z) and the orientation of the cell at location p(x,y,z), and the horizontal angle, θ, refers to the angle between the horizontal (x) and the orientation of the cells at location p(x,y,z). In order for the cells to be "*exclusively*" swimming in the cross-stream direction in a shear flow, θ should be ~90° and cos (ϕ) should be ~90° or ϕ ~0°. It can be seen that for shear flow, both the above conditions (θ = 90°, ϕ ~0°) are satisfied. The cells appear to be concentrated in the shear range, $S \geq 10$ s^{-1}, indicating that the observed cross-stream phenomenon occurs only above a critical shear rate, $S \geq 10$ s^{-1}. In contrast, in regions of low shear ($S \leq 10$ s^{-1}) where the shear has not reached the critical shear, it can be observed that the cells do not appear to be concentrating in the horizontal plane and may possibly spread across the micro-fluidic channel.

In this chapter, we examined the observed swimming uniqueness of the cell in shear and stagnant flows via a mathematical model. The motion of both (*cis* and *trans*) flagellum of *Dunaliella* was investigated with respect to their individual waveforms and the swimming behavior of the organism. The forces and moments generated by the flagella were estimated numerically. In the first section, we compared the experimental results of swimming with numerical simulations using the method of Resistive Force Theory (RFT) (Gray and Hancock 1955), and show that there was a good agreement between the experimental observations and numerical simulation. Secondly, we developed a mathematical model to demonstrate that the moments generated by beating

flagella and their alignment to flow are necessary to counter-act the vorticity of the flow. The model includes (i) model description and nomenclatures; (ii) proof of dependency of the propulsive force on beating frequency; (iii) model application to cell swimming in a quiescent flow; (iv) CCW torque generation in a shear flow. A criterion of minimum difference in beating frequency for generating the torque in a shear flow was also provided. This criterion provided the lower bound of the asynchronous beating and was evaluated using a simple beating pattern and several offset distances against the experimental observations.

5.2 Materials and Methods

5.2.1 Microscopic Experiments

To determine the kinematics (*x*, *y* positions) of the flagella and the rotational motion of the cell body in a micro-fluidic channel, the method and techniques described in chapter 4 (4.5.4) (phase contrast microscopy (100×) on custom made microfluidic channel (400 μm, Fig. 5.4)) was adopted. The rotation of the cell body was elucidated by the position of nucleolus with nucleus and the angular velocity of both the fixed and the live cells were computed by manually identifying the periods of nucleolus in the video image sequence.

5.2.2 Jeffery Orbits

The motion of an isolated ellipsoid particle in a viscous fluid was described by Jeffery (Jeffery 1922) in 1922. Jeffery's orbits describe the irregular and random continuous

rotation of an ellipsoid suspended in a sheared fluid. Jeffery showed that ellipsoids of revolution rotate in a linear shear field with a time period, $T = \frac{2\pi(r_e + 1/r_e)}{S}$, where r_e is the ratio of major and minor axis of cell body, *S* is the shear rate. In our experiments, the flow pattern of fixed cells in shear were evaluated and compared with the live cells. Additionally, the flow pattern of fixed cells were examined to see if the cells followed the similar motions as the elongated passive ellipsoids, i.e. periodic tumbling with closed orbits as predicted by Jeffery.

5.2.3 Flagella Kinematics

To obtain the linear displacement of the flagellum in space, the positions (*x*, *y*) of the flagellum were mapped from the raw images. The raw images were converted from pixel dimension to physical dimension (μm) and using adobe photoshop an image contrast was applied to clearly distinguish the flagella (Fig. 5.5). A dense set of spatial observation locations was then implemented manually along the length of the flagellum and these points were extracted using a Matlab (Mathworks 2012b) developed code. This was done for the entire beating cycle of the flagellum, i.e., one complete cycle of the forward stroke and the recovery stroke. The starting positions of each beat of the flagellum were made to originate from (0, 0), by subtracting the starting position from the other positions throughout the length of the flagellum. More points were added in between the initially (raw) extracted points and a linear interpolation in space and time was done to obtain a smooth beating flagella. The positions were used measure the linear displacements (*x*, *y*) of the flagellum. Consequently, the linear velocities of the flagellum ($u = dx/dt$, $v = dy/dt$)

were obtained using the central forward differentiation. The displacement angle, φ that was manually obtained from the images was incorporated to rotate the position of the flagellum so that the flagellar motion was adjusted to point along the *y*-axis (into the page) direction.

$$u_{fg} = u\cos\varphi + v\sin\varphi \quad (1)$$

$$v_{fg} = -u\sin\varphi + v\cos\varphi \quad (2)$$

where u_{fg} and v_{fg} are the velocities of flagellum in normal and spanwise direction with respect to the body aligned reference frame (along *y*-axis), *u* and *v* are mapped out velocities of flagellum in the normal and tangential direction, respectively. These kinematic variables were used to describe the forces and moments on the flagellum using the RFT. The viscous force on the cell body was incorporated to find the total drag on the cell body and can be estimated from the formulas governing the motion of a sphere in Stokes flow (Lauga and Powers 2009). The added drag force ($\vec{F}_{body}$) by the cell body was given by,

$$\vec{F}_{body} = 12\pi\mu R \quad (3)$$

where μ is the dynamic viscosity of the culture medium, and *R* is the equivalent spherical radius of an ellipsoidal cell. The radius of equivalent sphere from an ellipsoid was calculated based on the following expression. The area of the ellipsoid is, $A_s = \pi ab$, where *a* is the major and *b*, the minor axis length of the cell body. The value of $A_s = 218.4\ \mu m^2$, for $a = 10.5\ \mu m$ and $b = 6.62\ \mu m$ (note: *a*, *b* values are obtained from the experiment). The surface area of the sphere, $S_a = 4\pi R^2$. Equating A_s to S_a, the equivalent radius, *R* was found to be 4.17 μm.

5.2.4 RFT on the Flagellum

For a low Reynolds number swimming of micro-organism, the propelling forces of micro-organisms are balanced by resistance forces exerted by the ambient fluid. The resistance force are approximated by resistive-force theory, introduced by Gray and Hancock, 1955. If the force exerted on the fluid is non-zero on average, the micro-organisms will have net movement, and will swim by the beating of the flagella. The presence of an inert head would lower the speed of the micro-organism compared to propelling with the flagellum alone. RFT states that the normal and tangential components of force acting on the fluid by an element of flagellum is proportional to the normal and tangential component of the relative velocity of the flagellum with the fluid far away, provided the radius of curvature is large compared to its diameter. Thus approximately the total force exerted by a flagellar segment ($\vec{F}_{flag}$) is:

$$\vec{F}_{flag} = \vec{F}_{\perp} + \vec{F}_{||} = \varepsilon_{\perp} u_{fg} dl_f + \varepsilon_{\parallel} v_{fg} dl_f \tag{4}$$

where $\varepsilon_{\perp}$ and $\varepsilon_{\parallel}$ are the resistance coefficients, u_{fg} and v_{fg} are the velocities in the normal and tangential direction respectively, and dl_f is the differential length of the flagellum. The subscript, "*fg*", refers to the flagellum. The total net force can then be obtained by integrating over the entire flagellum. The total net drag force ($\vec{F}_T$), experienced by the cell body would then be,

$$\vec{F}_T = \vec{F}_{flag} + \vec{F}_{drag} \tag{5}$$

Previously, Jones et al. 1994, investigated the swimming signatures of *Chlamydomonas*, a bi-flagellated green alga, which exhibits gravitactic (upward swimming in an ambient fluid) and gyrotactic (balance of gravity and viscous flow) behavior, in shear flow using the RFT approach. O'Mally 2011, used boundary element

method to investigate the swimming behavior of *Chlamydomonas* in shear flow where the aforementioned swimming character was not reported to be observed.

5.3 Physical Model Description

5.3.1 Model Description

Model *Dunaliella* has two identical flagella with the nominal length, $l_f = \sim 12$ μm and a radius of r_{fg}. In literature, there exist the kinematic differences between the two flagella. One flagellum close to the eyespot, namely *cis*-flagellum, which is observed to beat faster than the other one, named as *trans*-flagellum. In this model, the right flagellum (Fig. 5.6A) is designated as "*cis*" and the left as "*trans*". To simplify the model and to elucidate the fundamental physics, it was assumed that both flagella beat in the same plane, e.g. a plane parallel to *x*-*y* plane but offset a distance of d_{fg} to the center of mass (Fig. 5.6B), and presume the same beating pattern (Fig. 5.6A). Based on the observations, the model *cis*- and *trans*-flagellum are allowed to beat at different frequencies, i.e., $\omega^{cis} > \omega^{trans}$ where the superscript denotes the corresponding flagellum. Note that the waveform of the *trans*-flagellum at the time, t, reciprocates that of the *cis*-flagellum (Fig. 5.6A) presumably at a different time, $t + \Delta t$, as long as the phases are the same, i.e. $\omega^{cis}(t + \Delta t) = \omega^{trans} t$. These two waveforms that are reflectional symmetric to the fore-aft axis is defined as a corresponding pair. In the later section, the total net forces on these two flagella will be computed over a corresponding pair first and then averaged over various phases. For simplicity, the origin of our coordinates is located at the center of mass and the principle axis of rotation is the fore-aft axis (sketched in Fig. 5.6B).

Conventional notations, $\vec{\imath}$, $\vec{\jmath}$ and $\vec{k}$, are used for unit vectors of *x*, *y* and *z*-axis, respectively.

It is noted that the plane of flagella is located at a distance, d_{fg}, away from the axis of rotation. This unique offset in conjunction with the asynchronous beating of *cis*- and *trans*-flagellum underlines the key mechanism of the model to explain the experimental observations: (i) In a quiescent flow, cell swims forward and rotates counterclockwise (CCW) about its long axis; (ii) In a shear flow above a critical shear rate, *Dunaliella* migrate in the direction of flow vorticity, but remains irrotational. Elucidated in Fig. 5.6A the propulsive force generated by a beating flagellum scales linearly with its beating frequency, ω_{fg}. Since *cis*- and *trans*-flagellum beat asynchronously, the net propulsive force, $\langle\vec{F}_p\rangle$, generated by each flagellum differs substantially, i.e., the magnitude of $\langle\vec{F}_p^{cis}\rangle$ is larger than that of $\langle\vec{F}_p^{trans}\rangle$. The *y*-component must balance the viscous drag on the cell body, $\vec{F}_D = \left(\langle\vec{F}_p^{cis}\rangle + \langle\vec{F}_p^{trans}\rangle\right)\cdot\vec{\jmath}$, where " $\cdot$ " represents the dot product. Due to differences in their beating frequencies, the *x*-components of net propulsive forces, $\langle\vec{F}_p^{cis}\rangle$ and $\langle\vec{F}_p^{trans}\rangle$ (sketched as red arrows in Fig. 5.6B) will not balance and generate a net force normal to the fore-aft axis. Since the plane of flagella is located at a plane at d_{fg} away to the center, this radial force produces a CCW torque viewed from the rear (Fig. 5.6B). In a quiescent flow, this torque causes the cell to rotate about *y*-axis at the rate of Ω_{cell} and balances the clockwise (CW) moment by the viscous flow shear. In a shear flow, the same torque counteracts the flow vorticity and causes the cell to remain irrotational. This simple model appears to provide satisfactory explanation. On the other

hand, we also acknowledge that the current model cannot describe how *Dunaliella* reorient in the direction of local vorticity; neither does it explain why *Dunaliella* orient only in that direction. To answer these questions, a more sophisticated model may be needed but is beyond the scope of the current work.

In 5.3.2, the framework to describe the kinematics and kinetics of a beating flagellum using RFT will be established. In 5.3.3, this framework will be applied to derive the kinetics of a swimming algae in a quiescent flow and to prove that the net propulsive force of a flagellum scales linearly with its beating frequency, ω_{fg}, and the torque scales linearly with the difference of the beating frequency, $\Delta\omega_{fg} = \omega^{cis} - \omega^{trans}$ between the pair of the flagella. Then a discussion on the model in a quiescent flow will be provided. Finally, in 5.3.4, the model will be applied to the shear flow to determine the minimum $\Delta\omega_{fg}$ necessary to generate a CCW torque.

5.3.2 Kinematics and Kinetics of a Beating Flagellum

The parametric form will be used to describe the flagellum (Fig. 5.6A) and its kinematics. The parametric description is defined in a curvilinear coordinate system. The unit vectors for the normal (n) and transverse (s) axis are $\vec{e}_n$ and $\vec{e}_s$, respectively. The origin of the curvilinear coordinate is located at the root (s = 0) of the flagellum. The tip of the flagellum is at $s = l_f$. The entire filament is composed of a series of elements with a finite length of ds, centered at the position, $[x_s, y_s, z_s]$. Not to lose any generality, the position can be uniquely defined by three parametric functions of s and phase, $T(\omega_{fg}t)$, where ω_{fg} is the beating frequency in radians. For a linear phase function, the phase is

often expressed as $T = \omega_{fg}t + \phi$. Thus, one can define the entire moving flagellum at any given time, t, as the following:

$$x_s = x_n\left(s, T(\omega_{fg}t)\right),\ y_s = y_n\left(s, T(\omega_{fg}t)\right),\ z_s = d_{fg}; s \in [0, l_f]. \tag{6}$$

Consequently, the velocity, $[u_{fg}, v_{fg}, w_{fg}]$, of the flagellar element is expressed as

$$u_{fg} = \frac{dx_n}{dt} = \frac{\partial x_n}{\partial T}\frac{dT}{d(\omega_{fg}t)}\omega_{fg} = \frac{\partial x_n}{\partial T}\dot{T}\omega_{fg}$$

$$v_{fg} = \frac{dy_n}{dt} = \frac{\partial y_n}{\partial T}\frac{dT}{d(\omega_{fg}t)}\omega_{fg} = \frac{\partial y_n}{\partial T}\dot{T}\omega_{fg}$$

$$w_{fg} = 0 \tag{7}$$

where $\dot{T} = \frac{dT}{d(\omega_{fg}t)}$. The velocity scales linearly with the flagellar beating frequency. The resultant instantaneous propulsive forces generated by the portion of the element can be approximated using Resistive Force Theory,

$$d\vec{F}_{Par} = \varepsilon_{\parallel}\{(u_{fg}\vec{\imath} + v_{fg}\vec{\jmath}).\vec{e}_{\parallel}\}ds = \varepsilon_{\parallel}(u_{fg}cos\theta + v_{fg}sin\theta)\,ds\,;$$

$$d\vec{F}_{Per} = \varepsilon_{\perp}\{(u_{fg}\vec{\imath} + v_{fg}\vec{\jmath}).\vec{e}_{\perp}\}ds = \varepsilon_{\perp}(-u_{fg}sin\theta + v_{fg}cos\theta)\,ds \tag{8}$$

where subscript "$\parallel$" and "$\perp$" represent the parallel and perpendicular components to the element respectively, $d\vec{F}_{Par}$ is the parallel and $d\vec{F}_{Per}$, the perpendicular instantaneous force on the flagellum, and $\vec{e}_{\parallel}$ and $\vec{e}_{\perp}$ are the unit vectors which can also be defined in the following generic form in Cartesian coordinates:

$$\vec{e}_{\parallel} = \cos\theta_s\vec{\imath} + sin\theta_s\vec{\jmath};\ \vec{e}_{\perp} = -\sin\theta_s\vec{\imath} + cos\theta_s\vec{\jmath} \tag{9}$$

where $\tan(\theta_s) = \frac{\partial y_n/\partial s}{\partial x_n/\partial s}$. The instantaneous forces for forward thrust on the global flagellum are (Fig. 5.7):

Parallel ($d\vec{F}_{\parallel}$) : $d\vec{F}_{\parallel} = -\{d\vec{F}_{par}\}\vec{e}_{\parallel} = \{\varepsilon_{\parallel}[-(u_{fg}cos\theta + v_{fg}sin\theta)]ds\}\vec{e}_{\parallel}$

Perpendicular ($d\vec{F}_{\perp}$) : $d\vec{F}_{\perp} = -\{d\vec{F}_{per}\}\vec{e}_{\perp} = \{\varepsilon_{\perp}[-(-u_{fg}sin\theta + v_{fg}cos\theta)]ds\}\vec{e}_{\perp}$

The above equations can be written as:

$$d\vec{F}_{\parallel} = \{\varepsilon_{\parallel}\left[-\left(\frac{\partial x_n}{\partial T}\dot{T}\omega_{fg}cos\theta + \frac{\partial y_n}{\partial T}\dot{T}\omega_{fg}sin\theta\right)\right]ds\}\vec{e}_{\parallel} = -(\varepsilon_{\parallel}\omega_{fg}\dot{T}ds)\vec{g}_{\parallel}$$

$$d\vec{F}_{\perp} = \{\varepsilon_{\perp}\left[-\left(-\frac{\partial x_n}{\partial T}\dot{T}\omega_{fg}sin\theta + \frac{\partial y_n}{\partial T}\dot{T}\omega_{fg}cos\theta\right)\right]ds\}\vec{e}_{\perp} = -(\varepsilon_{\perp}\omega_{fg}\dot{T}ds)\vec{g}_{\perp} \quad (10)$$

where $\vec{g}_{\parallel}$ and $\vec{g}_{\perp}$ are the directional vectors that depend only on the waveform of the flagellum. These directional functions are:

$$\vec{g}_{\parallel}(s,t) = \left(\frac{\partial x_n}{\partial T}cos\theta_s + \frac{\partial y_n}{\partial T}sin\theta_s\right)(cos\theta_s\vec{\imath} + sin\theta_s\vec{\jmath}$$

$$\vec{g}_{\perp}(s,t) = \left(-\frac{\partial x_n}{\partial T}sin\theta_s + \frac{\partial y_n}{\partial T}cos\theta_s\right)(-sin\theta_s\vec{\imath} + cos\theta_s\vec{\jmath}) \quad (11)$$

The overall instantaneous forces on the flagellum can be obtained by:

$$\vec{F}_p(t) = -\int_0^{l_f}[(\varepsilon_{\parallel}\omega_{fg}T)\dot{ds}\,\vec{g}_{\parallel} + (\varepsilon_{\perp}\omega_{fg}\dot{T})ds\,\vec{g}_{\perp}]ds$$

$$= -\varepsilon_{\parallel}\omega_{fg}\dot{T}\int_0^{l_f}\left(\vec{g}_{\parallel} + \frac{\varepsilon_{\perp}}{\varepsilon_{\parallel}}\vec{g}_{\perp}\right)ds$$

$$= -\varepsilon_{\parallel}\omega_{fg}\dot{T}\int_0^{l_f}(\vec{g}_{\parallel} + \gamma\vec{g}_{\perp})ds \quad (12)$$

where $\gamma = \varepsilon_{\perp}/\varepsilon_{\parallel}$. The magnitude of the instantaneous force depends only on the beating frequency, and the direction solely on the specific waveform at a given time. Integrating over time or over phase, one can obtain the net propulsive force as

$$\langle \vec{F}_p \rangle = -\frac{\varepsilon_{\parallel}\omega_{fg}}{\tau}\int_0^{\tau}\left[\dot{T}\int_0^{l_f}(\vec{g}_{\parallel}+\gamma\vec{g}_{\perp})ds\right]dt \tag{13}$$

where τ is the integral time scale within which the net propulsive force is measured. Hence, it is proven that the magnitude of net propulsive force scales linearly with the beating frequency, but the direction depends only on the beating patterns of the flagellum. In short, the faster a flagellum beats, the larger the net propulsive force is. If flagella share the same beating pattern, directions of the propulsive forces must be the same.

5.3.3 Swimming in a Quiescent Flow

Assuming *cis*- and *trans*-flagellum maintaining a corresponding pair, one can simplify the position vectors for each element in cis-flagellum and its corresponding counterpart in *trans*-flagellum as

$$x_s^{cis} = x_n,\ y_s^{cis} = y_n\ z_s^{cis} = d; \qquad x_s^{trans} = -x_n,\ y_s^{trans} = y_n,\ z_s^{trans} = d \tag{14}$$

and subsequently the velocities as $\vec{\boldsymbol{u}}^{cis} = \omega^{cis}\dot{T}(\frac{\partial x_n}{\partial T}\vec{\imath} + \frac{\partial y_n}{\partial T}\vec{\jmath})$ and $\vec{\boldsymbol{u}}^{trans} = \omega^{trans}\dot{T}(-\frac{\partial x_n}{\partial T}\vec{\imath} + \frac{\partial y_n}{\partial T}\vec{\jmath})$ for *cis*- and *trans*-flagellum respectively. Note that the beating pattern of the flagella are identical but reflectional symmetric to each other and their beating frequencies are different, assuming $\omega^{cis} > \omega^{trans}$. Even with the existing asynchronous beating, one can always find a beating waveform of the *trans*-flagellum that is corresponding to that of the *cis*-flagellum. With this observation, the relationships of the instantaneous force by corresponding averaging and of the total net forces by phase averaging in this section will be derived. First, the geometric relationships for the tangent

and normal unit vectors of the pair can be obtained. The relationships include $\tan(\theta_s^{cis}) = \frac{\partial y_n/\partial s}{\partial x_n/\partial s}$ and $\theta^{trans} = \pi - \theta^{cis}$. Subsequently, the unit vectors for both flagella are simplified as the following using the above relationships:

$$\vec{e}_{\parallel}^{cis} = \cos\theta_s^{cis}\vec{\imath} + sin\theta_s^{cis}\vec{\jmath}, \qquad \vec{e}_{\perp}^{cis} = -\sin\theta_s^{cis}\vec{\imath} + cos\theta_s^{cis}\vec{\jmath}$$

$$\vec{e}_{\parallel}^{trans} = -\cos\theta_s^{cis}\vec{\imath} + sin\theta_s^{cis}\vec{\jmath}, \ \vec{e}_{\perp}^{trans} = -\sin\theta_s^{cis}\vec{\imath} - cos\theta_s^{cis}\vec{\jmath} \tag{15}$$

Using Eqs. 11 and 15, the directional functions for the *cis*-flagellum are:

$$\vec{g}_{\parallel}^{cis}(s,t) = \left(\frac{\partial x_n}{\partial T}cos\theta_s^{cis} + \frac{\partial y_n}{\partial T}sin\theta_s^{cis}\right)(cos\theta_s^{cis}\vec{\imath} + sin\theta_s^{cis}\vec{\jmath})$$

$$\vec{g}_{\perp}(s,t) = \left(-\frac{\partial x_n}{\partial T}sin\theta_s^{cis} + \frac{\partial y_n}{\partial T}cos\theta_s^{cis}\right)(-sin\theta_s^{cis}\vec{\imath} + cos\theta_s^{cis}\vec{\jmath}), \tag{16}$$

and the directional functions for the *trans*-flagellum in a corresponding waveform to that of the *cis*-flagellum are:

$$\vec{g}_{\parallel}^{trans}(s,t) = \left(\frac{\partial x_n}{\partial T}cos\theta_s^{cis} + \frac{\partial y_n}{\partial T}sin\theta_s^{cis}\right)(-cos\theta_s^{cis}\vec{\imath} + sin\theta_s^{cis}\vec{\jmath})$$

$$\vec{g}_{\perp}^{trans}(s,t) = \left(-\frac{\partial x_n}{\partial T}sin\theta_s^{cis} + \frac{\partial y_n}{\partial T}cos\theta_s^{cis}\right)(sin\theta_s^{cis}\vec{\imath} + cos\theta_s^{cis}\vec{\jmath}). \tag{17}$$

After substituting Eqs. 16, 17 into 12 and substantial algebraic operations, the net force on a pair of corresponding flagellum is obtained as:

***cis*-flagellum:** $\vec{F}_p^{cis} = -\varepsilon_{\parallel}\omega_{fg}\dot{T}\int_0^{l_f}(\vec{g}_{\parallel} + \gamma\vec{g}_{\perp})ds$

$$= -\varepsilon_{\parallel}\omega^{cis}\dot{T}\{\int_0^{l_f}[(\frac{\partial x_n}{\partial T}cos\theta_s^{2\,cis} + \frac{\partial x_n}{\partial T}\,sin\theta_s^{cis}cos\theta_s^{cis} + \frac{\partial y_n}{\partial T}sin\theta_s^{cis}cos\theta_s^{cis} +$$

$$\frac{\partial y_n}{\partial T}\,sin\theta_s^{2\,cis} \quad + \gamma\frac{\partial x_n}{\partial T}sin\theta_s^{2\,cis} - \gamma\frac{\partial x_n}{\partial T}\,sin\theta_s^{cis}cos\theta_s^{cis} - \gamma\frac{\partial y_n}{\partial T}sin\theta_s^{cis}cos\theta_s^{cis} +$$

$$\gamma\frac{\partial y_n}{\partial T}\,cos\theta_s^{2\,cis}]ds\}$$

$$= -\varepsilon_{\parallel}\omega^{cis}\dot{T}\{\int_0^{l_f}[(cos\theta_s^{cis^2} + \gamma sin\theta_s^{cis^2})\frac{\partial x_n}{\partial T} + (1-\gamma)sin\theta_s^{cis}cos\theta_s^{cis}\frac{\partial y_n}{\partial T}]ds\}$$

$$-\varepsilon_{\parallel}\omega^{cis}\dot{T}\{\int_0^{l_f}[(\gamma cos\theta_s^{cis^2} + sin\theta_s^{cis^2})\frac{\partial y_n}{\partial T} + (1-\gamma)sin\theta_s^{cis}cos\theta_s^{cis}\frac{\partial x_n}{\partial T}]ds\} \qquad (18)$$

***trans*-flagellum:** $\vec{F}_p^{trans} = -\varepsilon_{\parallel}\omega_{fg}\dot{T}\int_0^{l_f}(\vec{g}_{\parallel} + \gamma\vec{g}_{\perp})ds$

$$= -\varepsilon_{\parallel}\omega^{trans}\dot{T}\{\int_0^{l_f}[(-\frac{\partial x_n}{\partial T}cos\theta_s^{2\,cis} + \frac{\partial x_n}{\partial T}\,sin\theta_s^{cis}cos\theta_s^{cis} - \frac{\partial y_n}{\partial T}sin\theta_s^{cis}cos\theta_s^{cis} +$$

$$\frac{\partial y_n}{\partial T}\,sin\theta_s^{2\,cis} \quad - \gamma\frac{\partial x_n}{\partial T}sin\theta_s^{2\,cis} - \gamma\frac{\partial x_n}{\partial T}\,sin\theta_s^{cis}cos\theta_s^{cis} + \gamma\frac{\partial y_n}{\partial T}sin\theta_s^{cis}cos\theta_s^{cis} + \gamma$$

$$\frac{\partial y_n}{\partial T}\,cos\theta_s^{2\,cis}]ds\}$$

$$= -\varepsilon_{\parallel}\omega^{trans}\dot{T}\{\int_0^{l_f}[-(cos\theta_s^{cis^2} + \gamma sin\theta_s^{cis^2})\frac{\partial x_n}{\partial T} - (1-\gamma)sin\theta_s^{cis}cos\theta_s^{cis}\frac{\partial y_n}{\partial T}]ds\}$$

$$-\varepsilon_{\parallel}\omega^{trans}\dot{T}\{\int_0^{l_f}[(\gamma cos\theta_s^{cis^2} + sin\theta_s^{cis^2})\frac{\partial y_n}{\partial T} + (1-\gamma)sin\theta_s^{cis}cos\theta_s^{cis}\frac{\partial x_n}{\partial T}]ds\} \qquad (19)$$

The net force on a pair of corresponding flagellum, (18 + 19) =>

$\vec{F}_p^{cis} + \vec{F}_p^{trans} =$

$$-\varepsilon_{\parallel}\omega^{cis}\dot{T}\{\int_0^{l_f}[(cos\theta_s^{cis^2} + \gamma sin\theta_s^{cis^2})\frac{\partial x_n}{\partial T} + (1-\gamma)sin\theta_s^{cis}cos\theta_s^{cis}\frac{\partial y_n}{\partial T}]ds\}$$

$$-\varepsilon_{\parallel}\omega^{cis}\dot{T}\{\int_0^{l_f}[(\gamma cos\theta_s^{cis^2} + sin\theta_s^{cis^2})\frac{\partial y_n}{\partial T} + (1-\gamma)sin\theta_s^{cis}cos\theta_s^{cis}\frac{\partial x_n}{\partial T}]ds\}$$

$$+ \ -\varepsilon_{\parallel}\omega^{trans}\dot{T}\{\int_0^{l_f}[-(cos\theta_s^{cis^2} + \gamma sin\theta_s^{cis^2})\frac{\partial x_n}{\partial T} - (1-\gamma)sin\theta_s^{cis}cos\theta_s^{cis}\frac{\partial y_n}{\partial T}]ds\}$$

$$-\varepsilon_{\parallel}\omega^{trans}\dot{T}\{\int_0^{l_f}[(\gamma cos\theta_s^{cis^2} + sin\theta_s^{cis^2})\frac{\partial y_n}{\partial T} + (1-\gamma)sin\theta_s^{cis}cos\theta_s^{cis}\frac{\partial x_n}{\partial T}]ds\}$$

$$= -\varepsilon_{\parallel}\dot{T}\left(\omega^{cis} - \omega^{trans}\right)G_1\vec{\imath} - \varepsilon_{\parallel}\dot{T}\left(\omega^{cis} + \omega^{trans}\right)G_2\vec{\jmath} \qquad (20)$$

where $G_1 = \int_0^{l_f}[(\cos^2\theta_s^{cis} + \gamma\sin^2\theta_s^{cis})\frac{\partial x_n}{\partial T} + (1-\gamma)sin\theta_s^{cis}cos\theta_s^{cis}\frac{\partial y_n}{\partial T}]$ and

$G_2 = \int_0^{l_f}[(\gamma\cos^2\theta_s^{cis} + \sin^2\theta_s^{cis})\frac{\partial y_n}{\partial T} + (1-\gamma)sin\theta_s^{cis}cos\theta_s^{cis}\frac{\partial x_n}{\partial T}]ds$

Finally, the net propulsive force generated by both *cis*- and *trans*-flagellum over time is expressed as,

$$\langle \vec{F}_p^{cis} \rangle + \langle \vec{F}_p^{trans} \rangle = -\frac{\vec{\imath}\varepsilon_{\parallel}\dot{Y}(\omega^{cis}-\omega^{trans})}{\tau}\int_0^{\tau} G_1 dt - \frac{\vec{\jmath}\varepsilon_{\parallel}\dot{Y}(\omega^{cis}+\omega^{trans})}{\tau}\int_0^{\tau} G_2 dt \qquad (21)$$

The phased average "⟨ ⟩" is performed first between a corresponding pair and then over entire phase space. The corresponding pair is defined (5.3.2) as a pair of beating waveforms that are identical but reflection to the cell fore-aft axis.

The result in Eq. 21 show that the *y*-component of total propulsive force increases with increasing of the mean beating frequency, $(\omega^{cis} + \omega^{trans})/2$, and balances the drag force on the cell body, $\vec{F}_D$ to propel the cell forward. A non-zero *x*-component can be produced as long as two flagella beat asynchronously, and a CCW torque is produced to cause the cell body to rotate about its fore-aft axis. The torque scales linearly with the difference of the beating frequency, $(\omega^{cis} - \omega^{trans})$. Notice that both directional vectors must be negative, i.e. $\int_0^{\tau} G_1 dt < 0$ and $\int_0^{\tau} G_2 dt < 0$, to produce the positive propulsion.

5.3.4 Swimming in a Shear Flow

As shown in Fig. 4.3(c), there are two net forces on each beating flagellum when the cell swims in the intermediate strain direction of a planar shear flow (note that the shear plane is the *x*-*z* plane and the intermediate strain direction is the *y*-axis). The forces on each flagellum are the propulsive force, F_p, and drag force, F_{df}. As shown in 5.3.2, the force, F_p, is linearly proportional to the beating frequency, ω_{fg}, and its direction is determined by the beating pattern only. To determine the drag force on the flagellum due to the presence of the flow shear, the flagellum kinematics and ensemble averaging over a

corresponding pair will be used. When a pair of corresponding flagella is subject to a cross-flow, $\vec{u}_{flow} = u_{flow}\vec{\imath}$, the resistive forces on the filament of *cis*-flagellum and its corresponding *trans*-flagellum respectively are the following:

$$\vec{F}^{cis}_{\perp,df} = \varepsilon_{\perp}\left(u_{flow} sin\theta_s^{cis}\right) ds\ \vec{e}_{\perp}$$

$$= \varepsilon_{\perp}\left(u_{flow} sin\theta_s^{cis}\right) ds\ (-\sin\theta_s^{cis}\vec{\imath} + cos\theta_s^{cis}\vec{\jmath}\,)$$

$$= -\varepsilon_{\perp} u_{flow} ds\left[\vec{\imath}\sin^2\theta_s^{cis} - \vec{\jmath} sin\theta_s^{cis} cos\theta_s^{cis}\right]$$

$$d\vec{F}^{cis}_{\parallel,df} = \varepsilon_{\parallel}\left(u_{flow} cos\theta_s^{cis}\right) ds\ \vec{e}_{\parallel}$$

$$= -\varepsilon_{\parallel}\left(u_{flow} cos\theta_s^{cis}\right) ds\ (\cos\theta_s^{cis}\vec{\imath} + sin\theta_s^{cis}\vec{\jmath}\,)$$

$$= -\varepsilon_{\parallel} u_{flow} ds\left[\vec{\imath}\cos^2\theta_s^{cis} - \vec{\jmath} sin\theta_s^{cis} cos\theta_s^{cis}\right]$$

Similarly,

$$d\vec{F}^{trans}_{\perp,df} = -\varepsilon_{\perp} u_{flow} ds\left[\vec{\imath}\sin^2\theta_s^{cis} + \vec{\jmath} sin\theta_s^{cis} cos\theta_s^{cis}\right]$$

$$d\vec{F}^{trans}_{\parallel,df} = -\varepsilon_{\parallel} u_{flow} ds\left[\vec{\imath}\cos^2\theta_s^{cis} + \vec{\jmath} sin\theta_s^{cis} cos\theta_s^{cis}\right] \quad (22)$$

where θ_s is the angle between filament to the *x*-axis, u_{flow} is the velocity magnitude of the cross flow and $\varepsilon_{\parallel}$ and $\varepsilon_{\perp}$ are the resistance coefficient in the tangent and normal directions. The subscript "df" suggests the drag force on each individual filament (opposite to the direction of propulsion).

Averaging over the corresponding pair gives,

$$d\vec{F}^{cis}_{\perp,df} + d\vec{F}^{cis}_{\parallel,df} + d\vec{F}^{trans}_{\perp,df} + d\vec{F}^{trans}_{\parallel,df} =$$

$$+ \quad -\varepsilon_{\perp} u_{flow} ds\left[\vec{\imath}\sin^2\theta_s^{cis} - \vec{\jmath} sin\theta_s^{cis} cos\theta_s^{cis}\right]$$

$$+ \quad -\varepsilon_{\parallel} u_{flow} ds\left[\vec{\imath}\cos^2\theta_s^{cis} - \vec{\jmath} sin\theta_s^{cis} cos\theta_s^{cis}\right]$$

$$+ \quad -\varepsilon_{\perp} u_{flow} ds\left[\vec{\imath}\sin^2\theta_s^{cis} + \vec{\jmath} sin\theta_s^{cis} cos\theta_s^{cis}\right]$$

$$+ \quad -\varepsilon_{\parallel} u_{flow} ds\left[\vec{\imath}\cos^2\theta_s^{cis} + \vec{\jmath} sin\theta_s^{cis} cos\theta_s^{cis}\right]$$

$$= -\varepsilon_{\perp} u_{flow} ds\left[2\vec{\imath}\sin^2\theta_s^{cis}\right] + -\varepsilon_{\parallel} u_{flow} ds\left[2\vec{\imath}\cos^2\theta_s^{cis}\right]$$

$$= -\gamma\varepsilon_{\parallel} u_{flow} ds\left[2\vec{\imath}\sin^2\theta_s^{cis}\right] + -\varepsilon_{\parallel} u_{flow} ds\left[2\vec{\imath}\cos^2\theta_s^{cis}\right] \qquad \text{(Note: } \gamma = \varepsilon_{\perp}/\varepsilon_{\parallel}\text{)}$$

$$= -2\varepsilon_{\parallel} u_{flow} ds\left(\gamma\sin^2\theta_s^{cis} + \cos^2\theta_s^{cis}\right)\vec{\imath} \qquad (23)$$

The entire drag force on the corresponding pair is given by,

$$\vec{F}_{df}(t) = -2u_{flow}\varepsilon_{\parallel} H_1(t)\vec{\imath} \qquad (24)$$

where $H_1(t) = \int_0^{l_f}\left(\gamma\sin^2\theta_s^{cis} + \cos^2\theta_s^{cis}\right)ds$ and the net drag after integration over time is given by,

$$\langle\vec{F}_{df}\rangle = -\frac{2u_{flow}\varepsilon_{\parallel}}{\tau}\vec{\imath}\int_0^{\tau} H_1(t)dt \qquad (25)$$

Since swimming *Dunaliella* is a self-propelling body, the cell is force- and moment-free, i.e. there is no net forces and torques on the cell. In 5.3.3, it is shown that the *y*-component of net propulsive force must balance the drag; whereas the *x*-component remains non-zero and subsequently produces a CCW torque that causes the cell body to rotate in a quiescent flow. Because of this rotation, the unbalanced radial force (*x*-component of the propulsive forces by *cis*- and *trans*-flagellum) produces no net effects to change the swimming direction of the cell, i.e. *model Dunaliella is capable of swimming in a straight line*.

In a shear flow, one can obtain the total moment about *y*-axis as the following:

$$-\left(\frac{\vec{\imath}\varepsilon_{\parallel}\dot{T}\left(\omega^{cis}-\omega^{trans}\right)}{\tau}\int_0^{\tau}G_1 dt+\frac{2u_{flow}\varepsilon_{\parallel}}{\tau}\vec{\imath}\int_0^{\tau}H_1(t)dt\right)d_{fg}=C_m\Omega'_{cell} \quad (26)$$

where Ω'_{cell} is the relative angular velocity of cell body to the surrounding fluids and C_m is the angular mobility coefficient (Lauga et al. 2006). For an elongated spheroid, like *Dunaliella*, and with its long axis in the intermediate strain direction, the relative angular velocity of the particle is found to be $\frac{1}{2}\omega_{flow}$, where ω_{flow} is the flow vorticity. The first term in LHS is the *x*-component of the propulsive force and the second is the flow drag on the flagella.

To maintain *Dunaliella* irrotational in a shear flow, the *x*-component of net propulsive force (the first term in LHS in Eq. 26) must exceed the drag force on the flagella (the second term in Eq. 26):

$$-\dot{T}\left(\omega^{cis}-\omega^{trans}\right)\int_0^{\tau}G_1 dt>2u_{flow}\int_0^{\tau}H_1(t)dt \quad (27)$$

Eq. 27 provides us a necessary condition to generate a CCW toque about the fore-aft axis that counter the CW moment exerted by the viscous shear flow. Note that the larger the difference in asynchronous beating frequencies between *cis*- and *trans*-flagellum, the larger the CCW torque is. The magnitude of the torque depends also on the waveform and beating pattern of the flagella, G_1 and H_1, but less prominent.

Below, the focus will be on establishing a criterion for minimum frequency difference, $\omega^{cis}-\omega^{trans}$, that would generate a CCW torque in a shear flow without assuming any specific beating kinematics. Using the simplest waveform, i.e. the flagellum will be treated as a rigid rod and allow it to beat like a paddle, and with constant flow shear, S, the cross flow at the plane of the flagella is $u_{flow}=S\,d_{fg}$. The

minimum beating frequency, $\Delta\omega_{fg} = 2\pi\Delta f_{min}$. Using $\Delta\,\omega_{fg} = \omega^{cis} - \omega^{trans}$, $\Delta f_{min} = \frac{\omega^{cis} - \omega^{trans}}{2\pi}$. Substituting the above expressions on Eq. 27,

$$-\dot{T}\left(\omega^{cis} - \omega^{trans}\right)\int_0^{\tau} G_1 dt > 2S\, d_{fg}\int_0^{\tau} H_1(t)dt$$

$$= -2\pi\Delta f_{min}\dot{T} > 2S\, d_{fg}\frac{\int_0^{\tau} H_1(t)dt}{\int_0^{\tau} G_1 dt}$$

$$\Delta f_{min} = -\frac{\left(\omega^{cis} - \omega^{trans}\right)}{2\pi} > 2S\, d_{fg}\frac{\int_0^{\tau} H_1(t)dt}{\int_0^{\tau} G_1 dt}$$

$$\Delta f_{min} = -\frac{\left(\omega^{cis} - \omega^{trans}\right)}{2\pi}$$

$$> 2S\, d_{fg}\frac{\int_0^{\tau}\left\{\int_0^{l_f}\left(\gamma \sin^2\theta_s^{cis} + \cos^2\theta_s^{cis}\right)ds\right\}dt}{\int_0^{\tau}\{\int_0^{l_f}[(\cos^2\theta_s^{cis} + \gamma\sin^2\theta_s^{cis})\frac{\partial x_n}{\partial T} + (1-\gamma)sin\theta_s^{cis}cos\theta_s^{cis}\frac{\partial y_n}{\partial T}]ds\}dt} \quad (28)$$

Substituting $sin^2\theta = 1 - cos^2\theta$, the expression reduces to $\left[\gamma + (1-\gamma)\cos^2\theta_s^{cis}\right]$ in the numerator of Eq. 28. With further simplifications the expression reduces to,

$$> 2S\, d_{fg}\frac{\int_0^{\tau}\{\int_0^{l_f}\left(\left[\gamma + (1-\gamma)\cos^2\theta_s^{cis}\right]\right)ds\}dt}{\int_0^{\tau}\{\int_0^{l_f}[(\gamma + (1-\gamma)\cos^2\theta_s^{cis})\frac{\partial x_n}{\partial T} + \frac{(1-\gamma)sin\theta_s^{cis}cos\theta_s^{cis}}{\gamma + (1-\gamma)\cos^2\theta_s^{cis}}\frac{\partial y_n}{\partial T}]ds\}dt}$$

$$> \frac{2S\, d_{fg}}{l_f}\frac{\int_0^{\tau}\{\int_0^{l_f}\left(\left[\gamma + (1-\gamma)\cos^2\theta_s^{cis}\right]\right)ds\}dt}{\int_0^{\tau}\{\int_0^{l_f}[(\gamma + (1-\gamma)\cos^2\theta_s^{cis})\frac{\partial x_n}{\partial T} + \frac{(1-\gamma)sin\theta_s^{cis}cos\theta_s^{cis}}{\gamma + (1-\gamma)\cos^2\theta_s^{cis}}\frac{\partial y_n}{\partial T}]ds\}dt}$$

Taking $\int_0^{\tau}\{\int_0^{l_f}\left(\left[\gamma + (1-\gamma)\cos^2\theta_s^{cis}\right]\right)ds\}dt = \int_0^{\tau}\{\left(\left[\gamma + (1-\gamma)\cos^2\theta_s^{cis}\right]\right)l_f\}dt$ and assuming $x_n, y_n \ll 1$ and integrating from θ_1^{cis} and θ_2^{cis}

$$> \frac{2S\, d_{fg}}{l_f} \int_{\theta_1^{cis}}^{\theta_2^{cis}} \frac{[\gamma + (1-\gamma)\cos^2\theta]}{\pi sin\theta[\gamma + (1-\gamma)\cos^2\theta]} d\theta$$

$$\Delta f_{min} > \left(\frac{2d_{fg}}{l_f}\right) \int_{\theta_1^{cis}}^{\theta_2^{cis}} \frac{[\gamma + (1-\gamma)\cos^2\theta]}{\pi sin\theta[\gamma + (1-\gamma)\cos^2\theta]} d\theta$$

$$\Delta f_{min} = \frac{\omega^{cis} - \omega^{trans}}{2\pi} > S\left(\frac{2d_{fg}}{l_f}\right) C \tag{29}$$

where C is constant for specific beating patterns and needs to be evaluated numerically. In the simple case, the coefficient, C, can be obtained analytically as,

$C = \int_{\theta_1^{cis}}^{\theta_2^{cis}} \frac{[\gamma+(1-\gamma)\cos^2\theta]}{\pi sin\theta[\gamma+(1-\gamma)\cos^2\theta]} d\theta$, where θ_1^{cis} and θ_2^{cis} are the starting and ending angular positions of the *cis*-flagellum to the *x*-axis.

5.4 Results

5.4.1 Jeffery Orbit

Our observation shows that the fixed cells migrate similar to a passive particle in a shear flow. With an experimental value r_e= 1.58 (ratio of *a* (=10.5 μm) and *b* =(6.62 μm)) and S = 20 s^{-1}, an estimation of T ~1.5 Hz is obtained. The measured value of T is comparable to the period of rotation of algal cells observed in the stagnant flow (~2Hz).

5.4.2 Flagella Beating Pattern

The representative time evolutions of the *cis* and the *trans*- flagellum beating as the cell propels forward are displayed under observed experimental (Fig. 5.8A) and predicted numerical (Fig. 5.8B) conditions. The experiments were recorded at 600 Hz or 1/600

seconds and it takes approximately 17/600 seconds to complete one beat (forward or backward) cycle. In order to create a smooth flagella beating, in the simulation, a cubic spline interpolation was performed creating 1/6000 data between experimentally recorded consecutive times of the beating flagella. This results in a smooth waveform progression of the flagella compared to the experimental data. It is observed that during the effective stroke, bending waves move the flagella toward the posterior of the cell closer to the cell body. During the recovery stroke, the flagella are restored to their initial position by the same bending wave (see Fig. 5.9). Both flagellum beat in the same waveform pattern even though the frequency of *cis* (37 Hz) and *trans*- flagellum (30 Hz) is different. The beating pattern observed is mostly asynchronous with periodic (or occasional) slips of synchrony. The temporal waveform of the *cis*- (Fig. 5.9A) and *trans*- flagellum (Fig. 5.9B) and simultaneous beating (Fig. 5.9C) of the flagellum are pictorially depicted in Fig. 5.9.

5.4.3 Comparison between Experimental and Simulated Results

The velocities (u_{fg} and v_{fg}) obtained from the RFT are compared with the experimental observation (Fig. 5.10). The drag coefficients (C_S and C_T) are achieved iteratively by trial and error to match with the experimental results (shown as dots). The value of drag coefficients (C_s = 0.64 and C_T = 1.53) that matched the closest experimental values was consistent with an earlier observation on similar swimming micro-algae *Chlamydomonas* (O' Malley 2011). The simulation data under-predicts the velocity values from the experimental results in the forward stroke mode (<0.012 seconds) but over-predicts in the backward stroke mode (>0.012 seconds). This observation holds true for both the stream-

wise (u_{fg}) and the span-wise (v_{fg}) velocities of the flagella. The forces generated by the *cis* and *trans*- flagellum are shown in Fig. 5.11. The drag coefficients, C_S = 0.64 and C_T = 1.53 were used for force calculation. The forces display a similar trend to the velocity profile. This can be expected since the forces are linearly proportional to the velocity. The maximum force (positive) with a value of ~15 pN is observed during the power stroke (<0.012 s) and minimal force (negative) with a value of ~8 pN is observed during the effective stroke (>0.012 s) for *trans*- flagellum. The values are slightly higher for *cis*-flagellum with the values being 18 pN (positive) and 11 pN (negative). This is consistent with our observation of *cis*- flagellum beating faster than the *trans*- flagellum, therefore, the value of forces should be higher for *cis*-flagellum. Also, it can be observed that the *cis*- and the *trans*- force cycles are complementary to each other during the asynchronous beating of the flagella although there exists a difference in beating frequency (~ 7Hz) between the two flagellum. The net moment or torque produced by the *trans*-flagella in a shear flow when the angle of inclination between the *trans*- flagellum with respect to head is 45° (that is, when *trans*-flagellum starts beating, it's tip makes an angle of 45° with respect to head), is depicted in Fig. 5.12. The shape of the moments is a sine wave like function. It should be noted that the torque would be zero if both the flagellums were in the same beating plane.

5.4.4 Physical Model Prediction

It is observed that C varied with the selection of θ_1^{cis} and θ_2^{cis} and was bounded between 0.80 and 1.76. The maximum value of 1.76 was used to obtain a criterion for the minimum difference in beating frequency, Δf_{min}. In a shear flow at the rate of $S =$

$20\ s^{-1}$ and the flagellum length of $l_f = 12\ \mu m$, the model predictions for the minimum difference in beating frequency versus flow shear using different d_{fg} values (Fig. 5.13) was plotted. The result demonstrated that minimum frequency difference scales linearly with local shear stress and d_{fg}. In comparison to the experimental measurements, a small separation, d_{fg} (=0.1μm) which is the lower bound of asynchronous beating, provides the criterion of minimum difference in beating frequency for generating the torque in a shear flow for the cells to counter-act the viscous flow moment by flow shear and remain irrotational.

5.5 Conclusion

Firstly, a comparison was made between the experimentally observed velocities of *Dunaliella* cells with the numerical results using the RFT approach. The forces and moments (or torque) generated by the beating flagella were estimated numerically. The numerical results closely matched with the experimental values. Secondly, a physical model was developed to obtain the torque that rotates the swimmer in quiescent flow and keeps the swimmer steady in a shear flow. Our assertion is that the flagella kinetics is the key to the question: "*why the motile cell remain irrotational in shear flow?*" The model has incorporated the key ingredient of the flagella kinematics, including the asynchronous beating between the *cis*- and the *trans*-flagellum. It is also proved that the magnitude of the propulsive force on a flagellum scales linearly with its beating frequency and the direction depends only on its beating pattern. The asynchronous beating, assuming the identical but symmetric pattern to the cell fore-aft axis (or the swimming direction),

produces a pair of propulsive forces. The net axial component of the total propulsive force summed over the pair must balance the drag on the cell body. The net radial component, on the other hand, scales with the frequency difference of the pair and generates a force normal to the fore aft axis. When the flagellum pair beats in a plane slightly offset to the center of mass, this net radial force will produce a CCW torque/moment about the fore-aft axis. In a quiescent flow, this torque causes the cell to rotate, whereas in a shear flow, this torque could counteract the viscous flow moment by flow shear and cause the cell to be irrotational. Although we have not been able to experimentally verify our assumption about the offset between the plane of flagella and the center of mass, the offset found from the model prediction appears to be small and highly possible considering the asymmetric shape of the cell. A criterion of minimum difference in beating frequency for generating the torque in a shear flow is demonstrated. This criterion provides the lower bound of the asynchronous beating. It is evaluated using a simple beating pattern and several offset distances against the experimental observation. The possible offsets are well within the physiologically sound parameter range.

5.6 Future Work

The physical model proposed is not an explicit model that explains the observation of cell swimming in a shear flow; perhaps there could be other possible mechanisms that allow cells to maneuver in the environment with different shear rate and different beating plane alignment, so it would be interesting to quantify all the physical plausibility and their implications. The other mechanism that could be possible is out-of-plane beating of the

flagella or the two flagella beating in different planes. In Fig. 5.14, the slender body theory is used (which claims to provide more accurate results than RFT because of less assumptions and sophisticated approach) to understand the flow field around the beating flagella in a quiescent flow at the instant of synchronous swimming. The observations show that flagellar beat generates vortices that may be helpful in expelling out fluids or nutrients, or possibly predators away from the flagellar proximity to a distant location. The streamlines and vectors may also provide important clues about the chemo-, photo- or other taxes attractant to the cell. These have not been investigated in our work. It would also be interesting to examine the characteristics of the flow field around the beating flagellum under shear flow conditions and/or when the beating of the flagella is asynchronous. Another important aspect to quantify would be the energy dissipated by the cell while swimming in a shear flow, since energy input/output is an important variable while designing engineering bioreactors aimed at culturing cells for biofuel production.

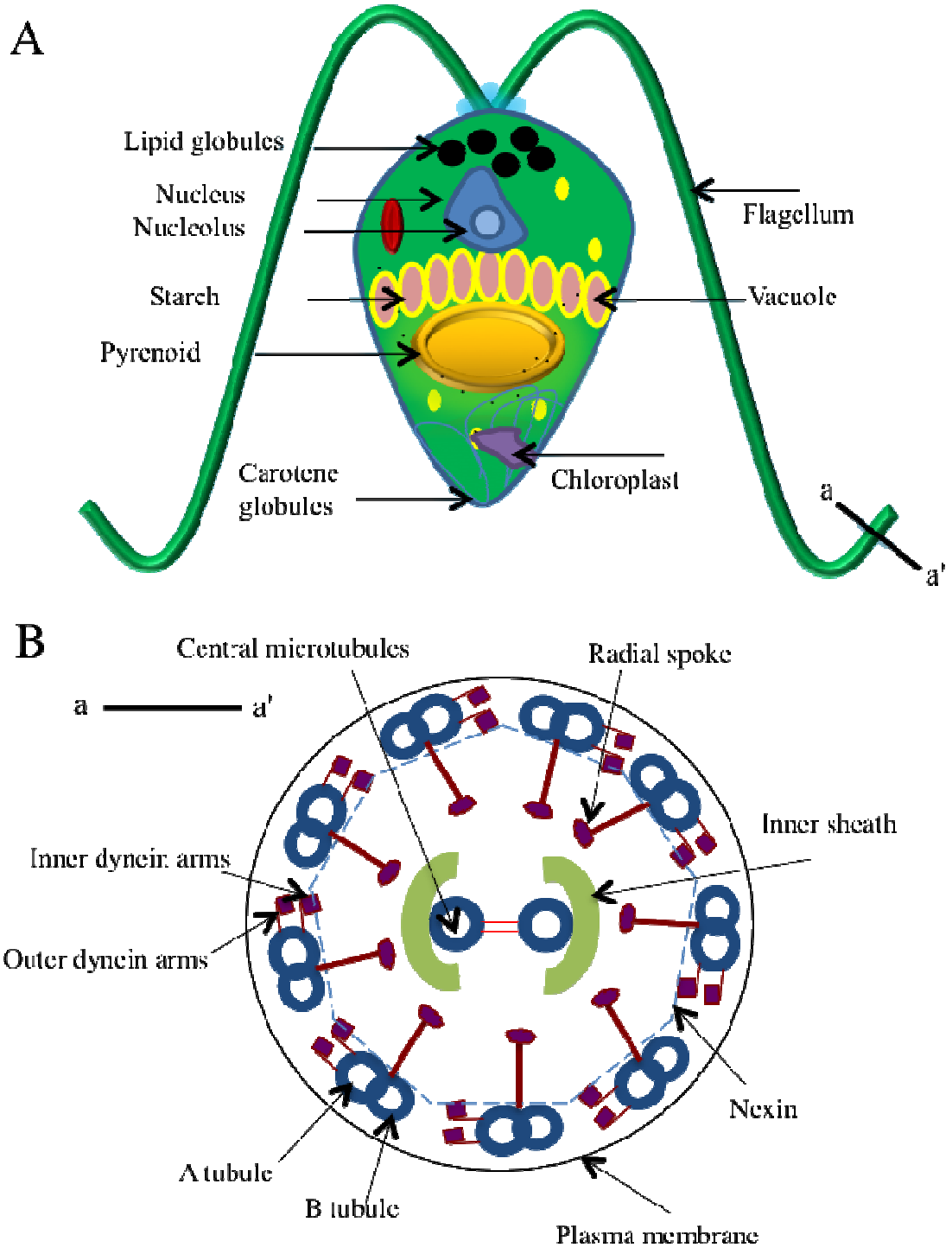

Fig. 5.1. (A) Cell body composition of *Dunaliella*. (B) Internal structure of the flagellum.

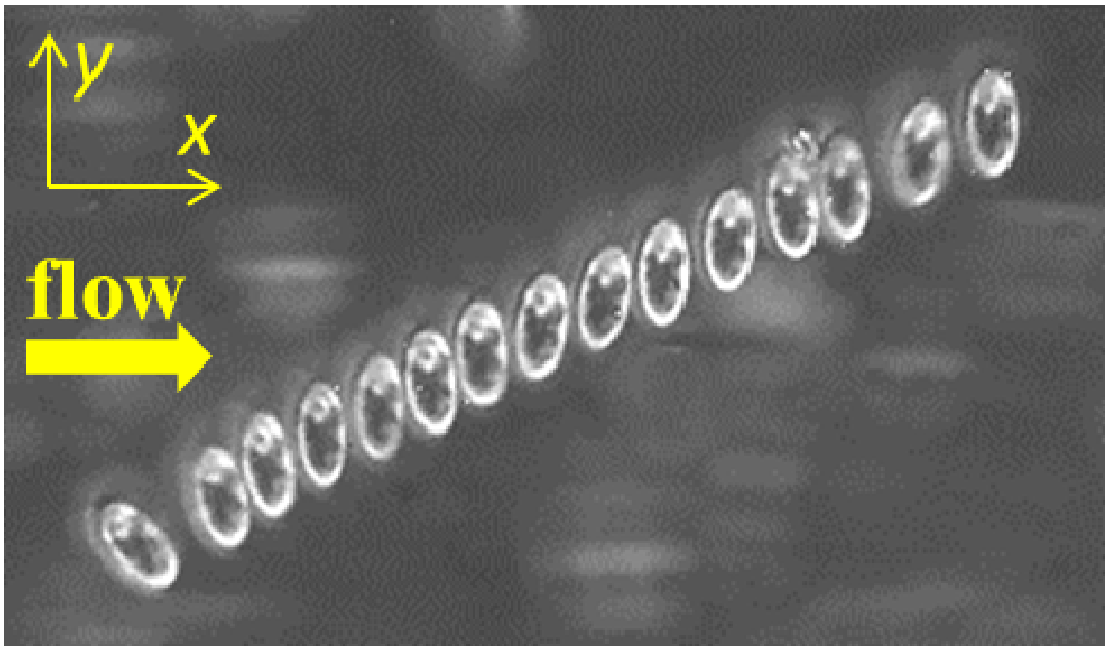

Fig. 5.2. Swimming of *Dunaliella* cell in a shear flow. The cell is observed to be swimming in the direction of local vorticity (*y*-axis), which is perpendicular to the direction of flow.

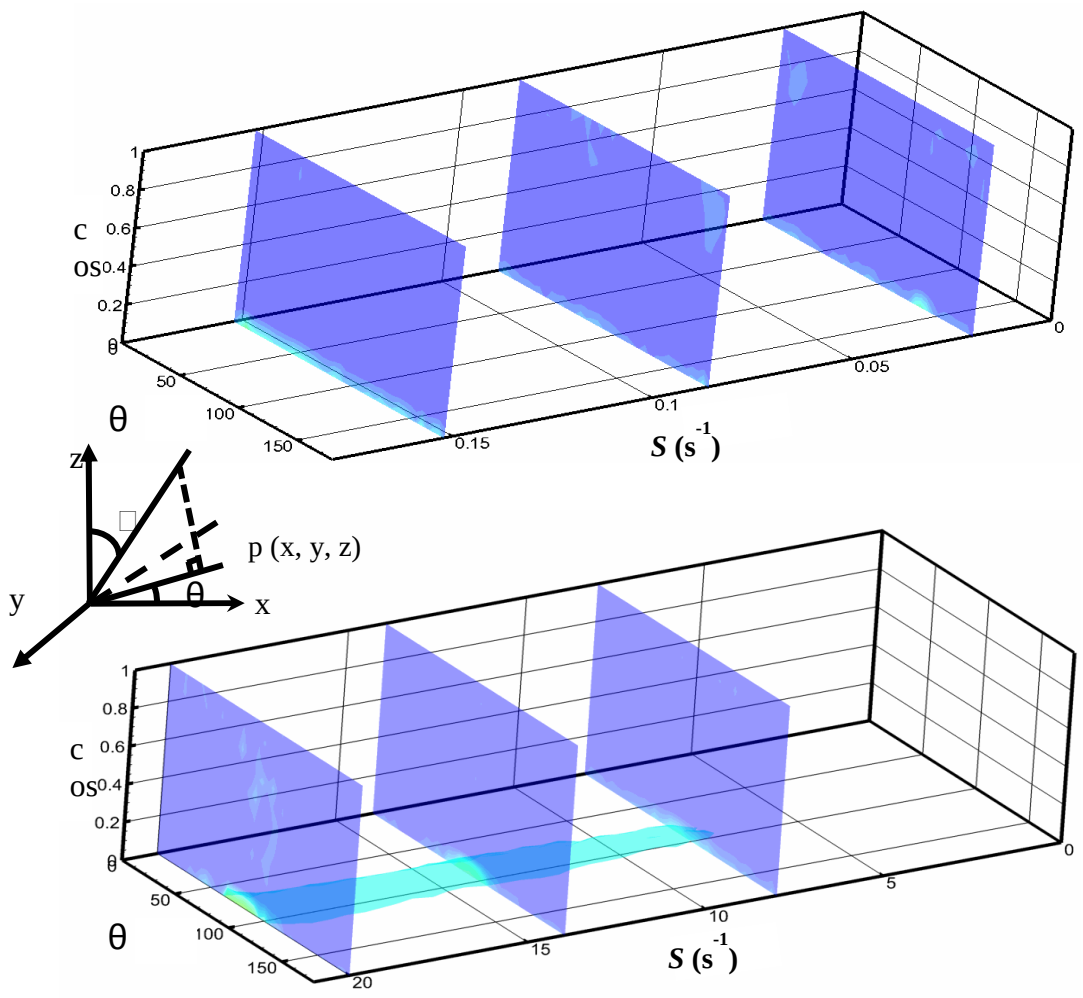

Fig. 5.3. Cross-stream migration of *Dunaliella* in (A) low shear (up to S = 0.2 s^{-1}) and (B) High shear (up to S =20 s^{-1}). The concentration of cells is observed in the horizontal plane at high shear (S > 10 s^{-1}).

Fig. 5.4. Photographic image of the micro-fluidic channel used for high speed experiments to observe the rotation of the cell body. A 400 μm thick silicon shim is sandwiched between a glass slide and a thin cover slip (100 μm).

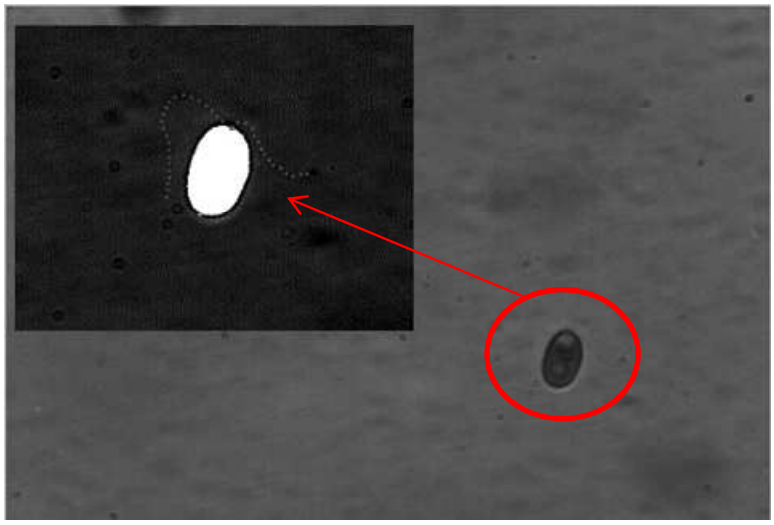

Fig. 5.5. The portion of the cell body with the flagella (shown in black, image size: 1016 × 1016 pixel) is re-sized to 531 × 412 pixel. A contrast of the resized image is developed to map the kinematics (*x*, *y* positions) of the flagella.

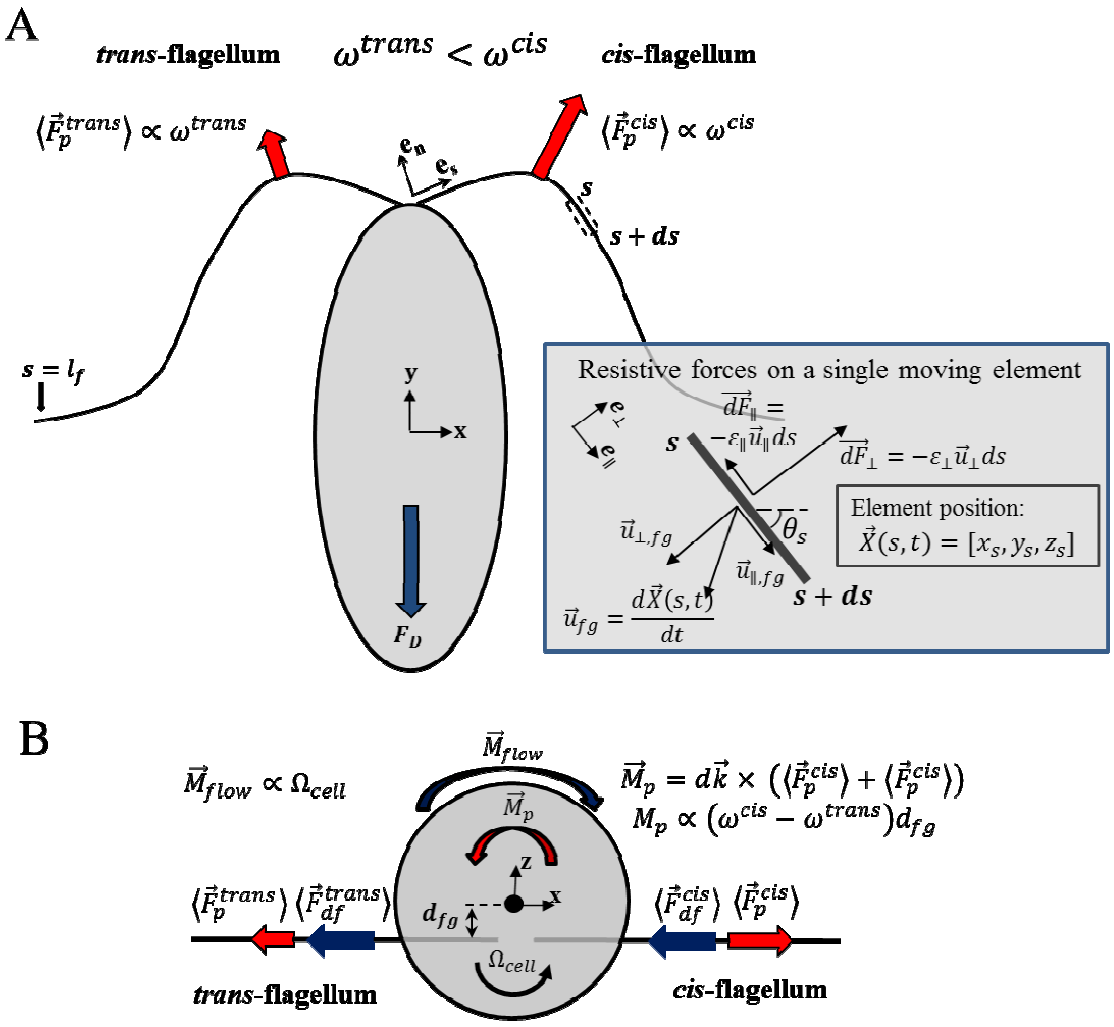

Fig. 5.6. Schematics showing the kinetics of *Dunaliella* swimming on the *x-y* plane while migrating in the direction of *y*-axis elucidates a generation mechanism of moment/torque about cell fore-aft axis owing to the asynchronous beating between *cis*- and *trans*-flagellum, and a plausible offset between the beating plane to cell's center of rotation (A) Top-view (*x-y* plane) (B) Rear-view of a swimming *Dunaliella* (*x-z* plane).

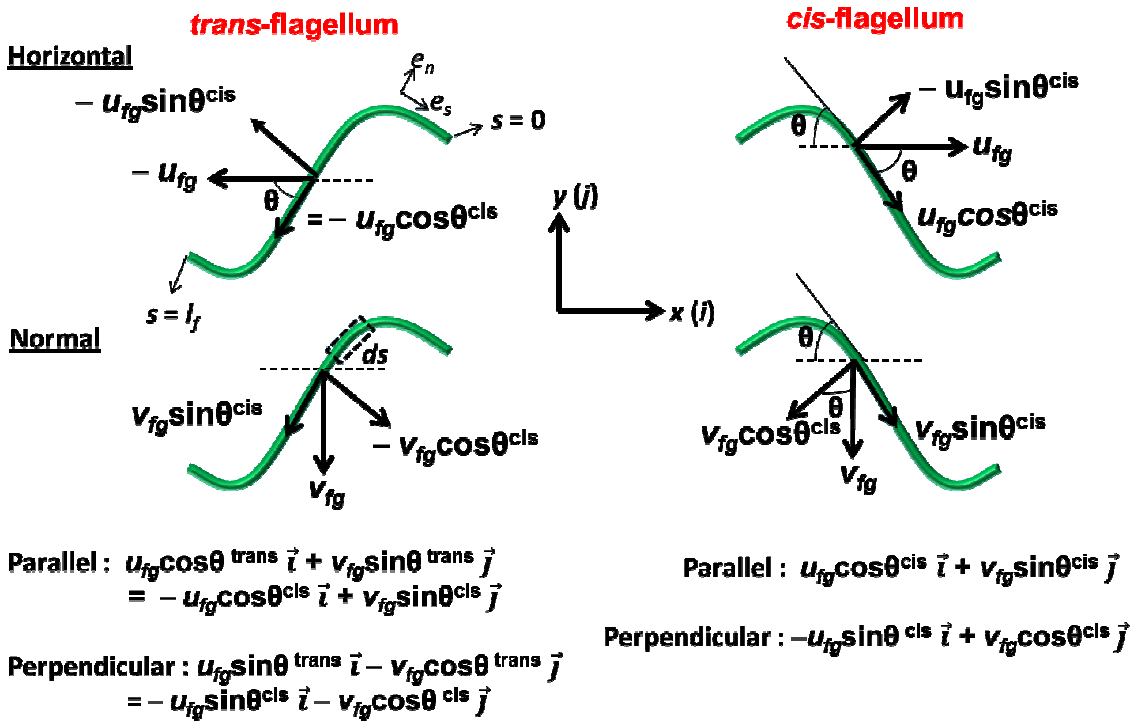

Fig. 5.7. Components of the velocities and the forces acting on the length of the flagellum.

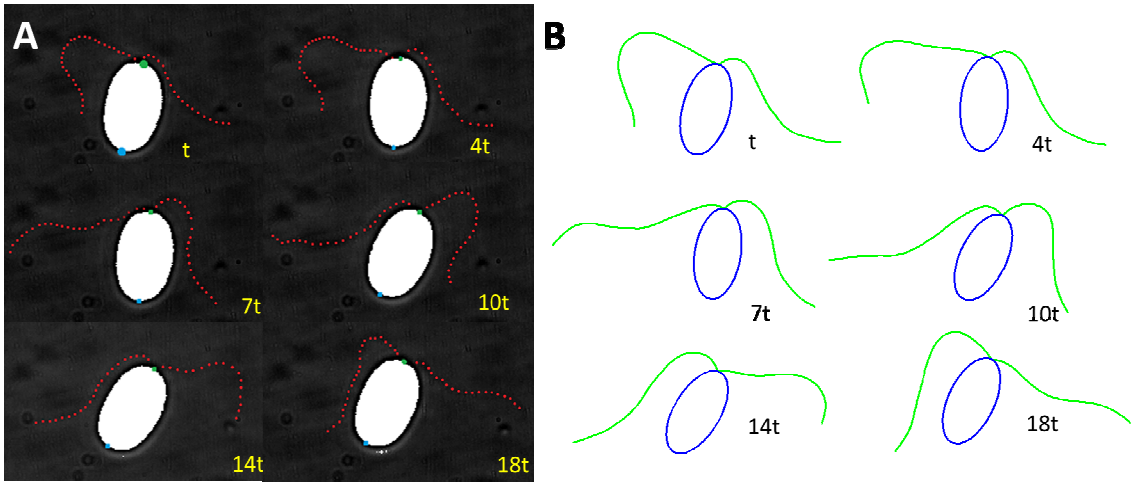

Fig. 5.8. Time history of the flagella beating in a shear flow (S = 20 s^{-1}). (A) Experimental observation. The red dots are manually drawn on the flagella (B) Simulated images. The variable "t" is 1/600 s.

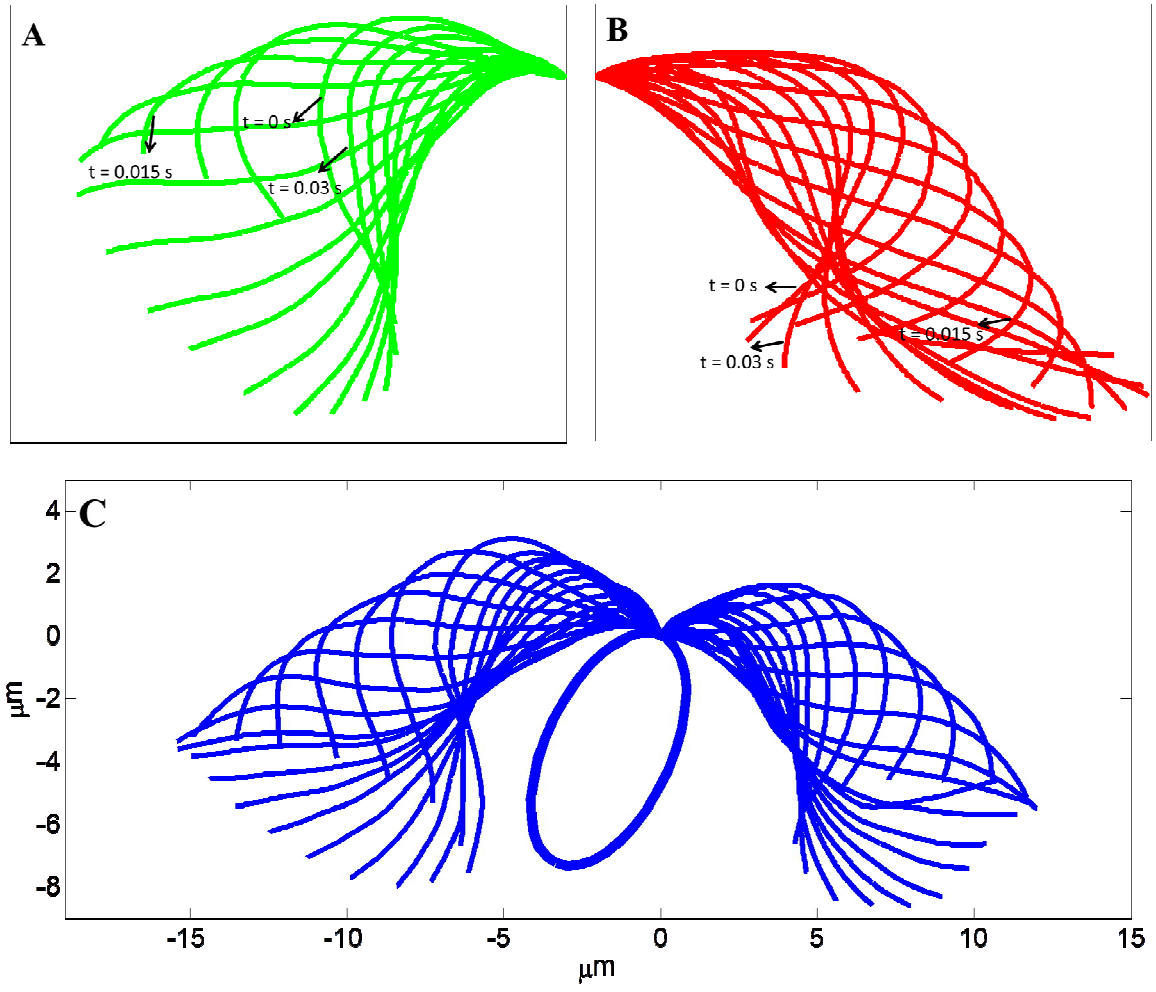

Fig. 5.9. Simulation results detailing the flagellar beating history for a typical asynchronous beat of the flagella while propelling in a shear flow. All flagellar beats are made to originate from the same point. (A) *Cis* flagellum; (B) *Trans*- flagellum; (C) Both flagellums on a representative cell body are shown. The typical flagellar length extends to ~15 µm.

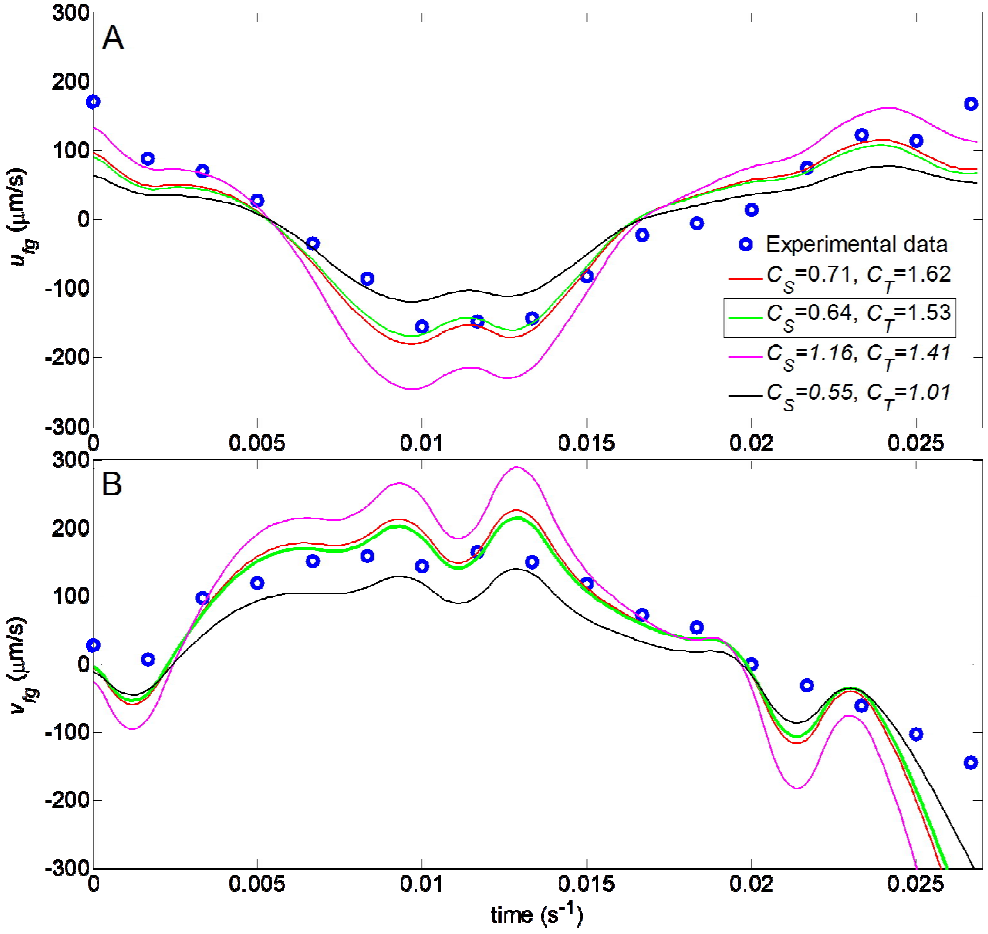

Fig. 5.10. The numerical results of flagellar velocities in the stream wise (u_{fg}) and spanwise direction (v_{fg}) as compared with the experimental observation. The drag coefficients, C_s = 0.64 and C_T = 1.53 closely match with the experimental values.

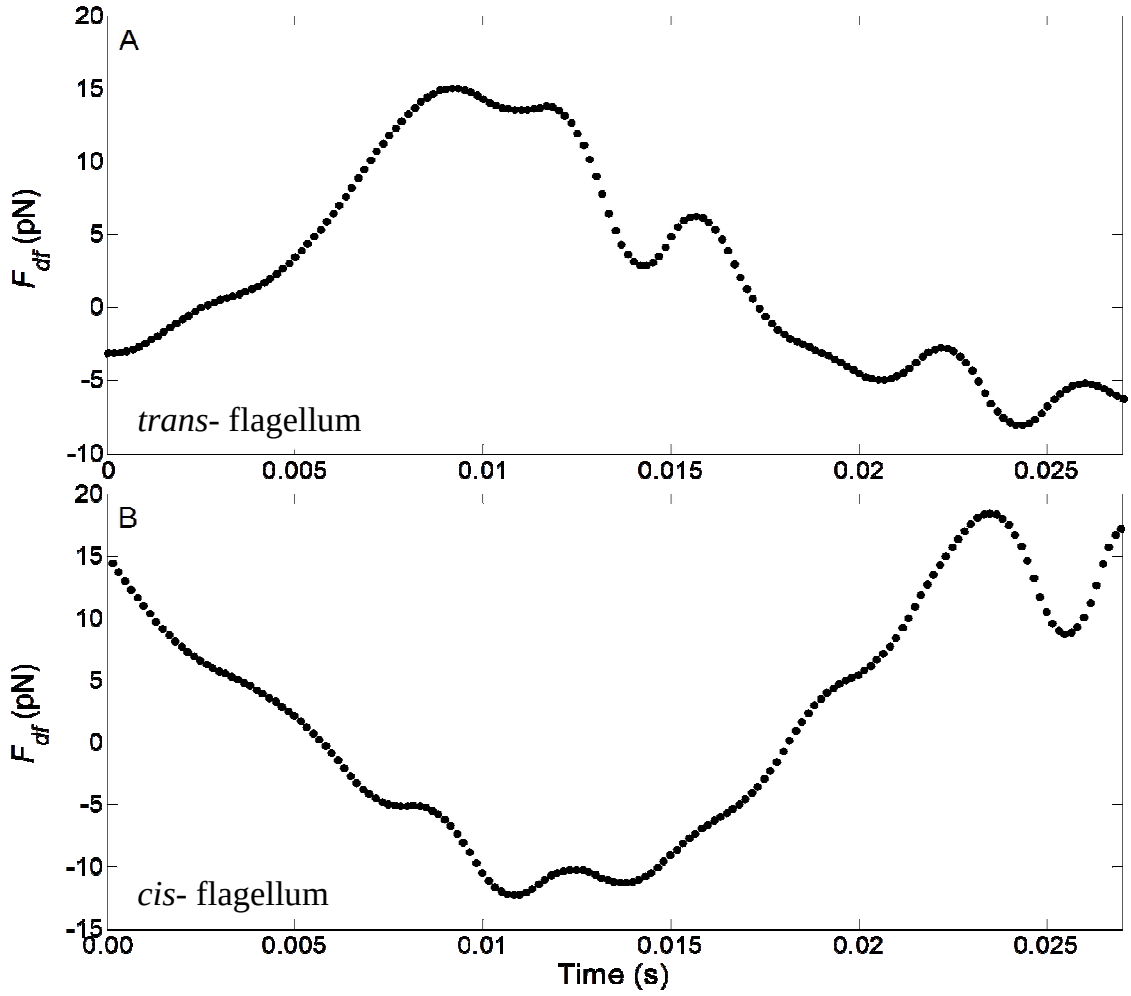

Fig. 5.11. The plot of the total drag force exerted by (A) *cis* and (B) *trans* flagellum in a shear flow (S= 20 s^{-1}) for one complete asynchronous beating cycle of the flagella.

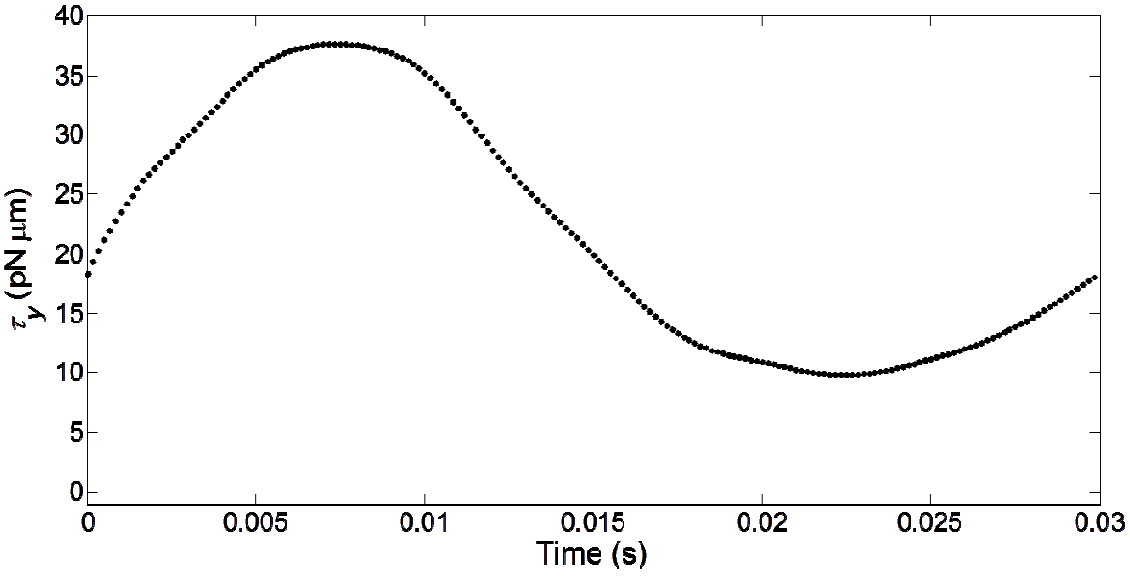

Fig. 5.12. Moment (or torque) produced by the *trans*- flagellum in a shear flow.

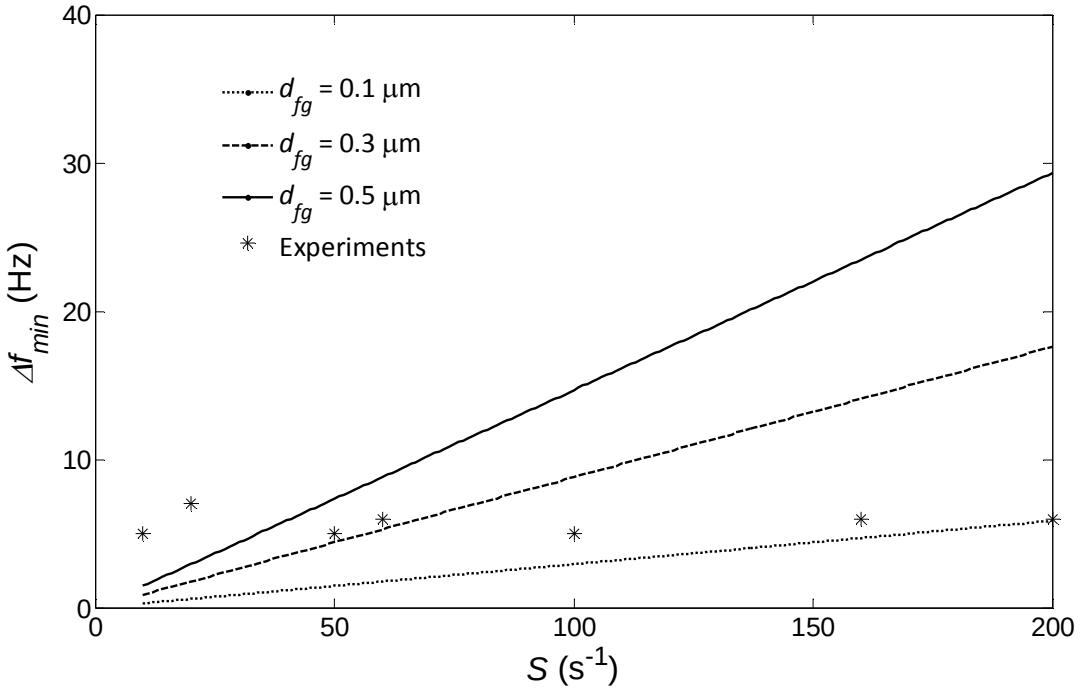

Fig. 5.13. Minimum difference in beating frequencies, Δf_{min}, of *cis*- and *trans*-flagellum vs. flow shear, *S*. Colored lines: model predictions for different offset distance, d_{fg}, i.e. from the plane of beating flagella to the center of rotation. Symbols: experimentally observed frequency difference, Δf, between *cis*- and *trans*- flagellum at different flow rate. Δf must exceed Δf_{min} to produce a CCW torque.

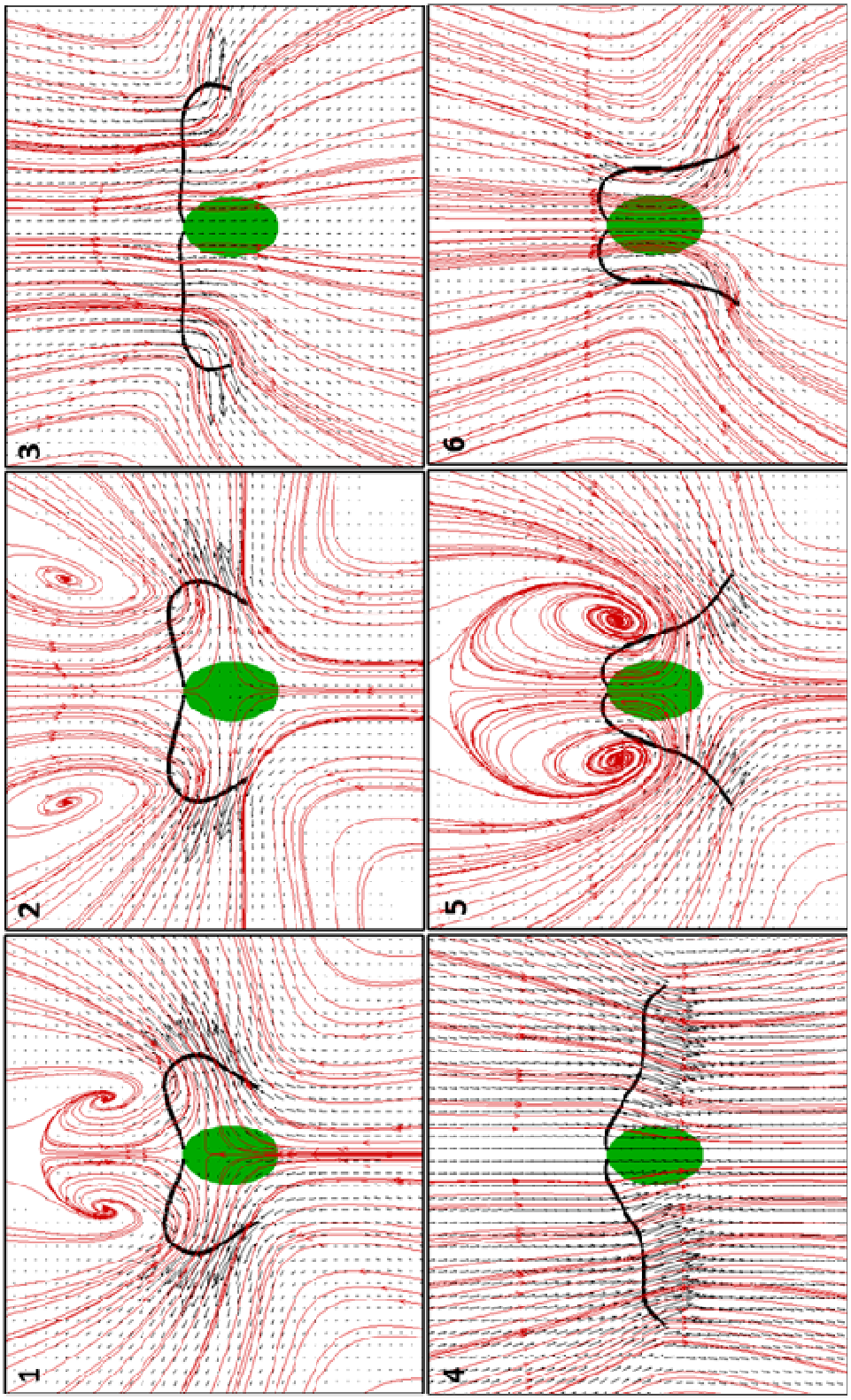

Fig. 5.14. Instantaneous flow field velocity around a flagellum while completing a synchronous beat cycle. The number in each refers to the time. (Real time = Number * 3/600 in seconds).

Bibliography

1. Agarwal, G. P. 1990. Glycerol. *Adv. Biochem. Eng/ Biotechnol.* **41**:95-125, doi: 10.1007/BFb0010229.
2. Aizawa, K., and S. Miyachi. 1992. Photosynthesis: Biochemical and Physiological and adaptation. In: Avron M, Ben-Amotz A, editor. *Dunaliella: Physiology, Biochemistry, and Biotechnology*. Florida: CRC Press. p 45-62.
3. Al-Hasan, R. H., M. A. Ghannoum, A-K. Sallal, K. H. Abu-Elteen, and S. S. Radwan. 1987. Correlative changes of growth, pigmentation and lipid composition of *Dunaliella salina* in response to halostress. *J. Gen. Microbiol.* 1**33**:2607–2616, doi: 10.1099/00221287-133-9-2607.
4. Al-Homoud, A., and M. Hondzo. 2008. Enhanced uptake of dissolved oxygen and glucose by Escherichia coli in a turbulent flow. *Appl. Microbiol. Biotechnol.* **79**:643–655, doi: 10.1007/s00253-008-1446-x.
5. Amaro, H. M., Â. C. Macedo, and F. X. Malcata. 2012. Microalgae: An alternative as sustainable source of biofuels?. *Energy*. **44**:158–166, doi: 10.1016/j.energy.2012.05.006.
6. Avron, M. 1992. Osmoregulation. In: Avron M, Ben-Amotz A, editor. *Dunaliella: Physiology, Biochemistry, and Biotechnology*. Florida: CRC Press. p 135-164.
7. Avron, M., and A. Ben-Amotz. 1992. *Dunaliella*: Physiology, Biochemistry, and Biotechnology. CRC Press.
8. Bearon, R. N., D. Grünbaum, and R. A. Cato´lico. 2004. Relating cell-level swimming behaviors to vertical population distributions in Heterosigma akashiwo (Raphidophyceae), a harmful alga. *Limnol. Oceanogr*. **49**: 607–613.
9. Ben-Amotz, A., 1980. Glycerol, *β*-carotene and dry algal meal production by commercial cultivation of *Dunaliella*. In: Shelef G, Soeder CJ, editor. *Algae biomass, production and use*. Amsterdam: Elsevier. p 603–610.

10. Ben-Amotz, A., A. Shaish, and M. Avron. 1991. The biotechnology of cultivating *Dunaliella* for production of ß -carotene rich algae. *Bioresour. Technol*. **38**:233-235.
11. Ben-Amotz, A., and M. Avron. 1982. Glycerol and β-carotene metabolism in the halotolerant alga *Dunaliella:* a model system for biosolar energy conversion. *Trends Biochem. Sci.* **6**:297-299, doi: 10.1016/0968-0004(81)90106-7.
12. Ben-Amotz, A., I. Sussman, and M. Avron. 1982. Glycerol production by *Dunaliella*. *Experientia.* **38**:49–52, doi: 10.1007/BF01944527.
13. Ben-Amotz, A., T. G. Tornabene, and W. H. Thomas. 1985. Chemical profiles of selected species of microalgae with emphasis on lipids. *J. Phycol.* **21**:72–81, doi:10.1111/j.0022-3646.1985.00072.x.
14. Blackburn, N., T. Fenchel, and J. Mitchell. 1998. Microscale nutrient patches in planktonic habitats shown by chemotactic bacteria. *Science.* **282**:2254-2256, doi: 10.1126/science.282.5397.2254.
15. Blake, J. R. and A. T Chwang. 1974. *J. Eng. Math.* **8**:23–29, doi: 10.1007/BF02353701.
16. Borowitzka, L. J., 1981. The microflora: Adaptations to life in extremely saline lakes. *Hydrobiologia*. **81**: 33–46, doi: 10.1007/BF00048704.
17. Borowitzka, L. J., and M. A. Borowitzka. 1989. Algal Biophysics. In: Vandamme EJ, editor. *Biotechnology of Vitamins, pigments, and growth factors.* Elsevier, NY, USA. p 22, ISBN-13: 978-1851663255.
18. Borowitzka, L. J., M. A. Borowitzka and T. P. Moulton. 1984. The mass-culture of *Dunaliella Salina* for fine chemicals-from laboratory to pilot plant. *Hydrobiologia*. **116**:115–121, doi: 10.1007/BF00027649.
19. Borowitzka. L. J., M. A. Borowitzka, and T. Moulton. 1984. Mass culture of *Dunaliella*: from laboratory to pilot plant. *Hydrobiologia*. **116/117**:115–121, doi: 10.1007/978-94-009-6560-7_18.
20. Brennan, L., and P. Owende. 2013. Biofuels from microalgae: Towards meeting advanced fuel standards. In: Lee JW, editor. *Adv. Biofuels Bioprod*. Springer. p. 553-599, doi: 10.1007/978-1-4614-3348-4_24.

21. Bretherton, F. P., and Lord F. R. S. Rothschild. 1961. Rheotaxis of spermatozoa. *Proc. R. Soc. London.* **153**:490-502, doi: 10.1098/rspb.1961.0014.
22. Chen, H., J. G. Jiang, and G. H. Wu. 2009. Effects of salinity changes on the growth of *Dunaliella salina* and its isozyme activities of glycerol-3-phosphate dehydrogenase. *J. Agric. Food Chem*. **57**: 6178–6182, doi: 10.1021/jf900447r.
23. Chen, H., J. G. Jiang. 2009. Osmotic responses of *Dunaliella* to the changes of salinity. *J. Cell. Physiol*. **219**:251-258, doi: 10.1002/jcp.21715.
24. Chengala, A. A., M. Hondzo, D. Troolin, and P. A. Lefebvre. 2010. Kinetic responses of *Dunaliella* in moving fluids. *Biotechnol. Bioeng*. **107**:65–75, doi: 10.1002/bit.22774.
25. Chengala, A., M. Hondzo, and J. Sheng. 2013. Microalga propels along vorticity direction in a shear flow. *Phys. Rev. E*. **87**:052704, doi: 10.1103/PhysRevE.87.052704.
26. Chisti, Y. 2007. Biodiesel from microalgae. *Biotechnol. Adv*. **25**:294–306, doi: 10.1016/j.biotechadv.2007.02.001.
27. Cohen, Z. 1999. Chemicals from Microalgae. CRC Press.
28. Cowan, A. K., P. D. Rose, and L. G. Horne. 1992. *Dunaliella* salina: A model system for studying the response of plant cells to stress. *J. Exp. Bot*. **43**:1535–1547, doi: 10.1093/jxb/43.12.1535.
29. Csanady, G. T. 1963. Turbulent diffusion of heavy particles in the atmosphere, *J. Atmos. Sci*. **20**:201–208.
30. Day, J. G., S. P. Slocombe, and M. S. Stanley. 2012. Overcoming biological constraints to enable the exploitation of microalgae for biofuels. *Bioresour. Technol.* **109**:245–51, doi: 10.1016/j.biortech.2011.05.033.
31. Dean, A. P., D. C. Sigee, B. Estrada, and J. K. Pittman. 2010. Using FTIR spectroscopy for rapid determination of lipid accumulation in response to nitrogen limitation in freshwater microalgae. *Bioresour. Technol*. **101**:4499–4507, doi: 10.1016/j.biortech.2010.01.065.
32. Dekshenieks, M. M., P. L. Donaghay, J. M. Sullivan, J. E. B. Rines, T. R. Osborn, and M. S. Twardowski. 2001. Temporal and spatial occurrence of thin

phytoplankton layers in relation to physical processes. *Mar. Ecol. Prog. Ser.* **23:**61-71, doi: 10.3354/meps223061.

33. Drescher, K., R. E. Goldstein, N. Michel, M. Polin, and I. Tuval. 2010. Direct Measurement of the Flow Field around Swimming Microorganisms. *Phys. Rev. Lett*. **105**:168101, doi: 10.1103/PhysRevLett.105.168101.
34. Durham, W. M., J. O. Kessler, and R. Stocker. 2009. Disruption of vertical motility by shear triggers formation of thin phytoplankton layers. *Science.* **323**:1067–1070, doi: 10.1126/science.1167334.
35. E. Lauga, W. R. DiLuzio, G. M. Whitesides, and H. A. Stone. 2006. Swimming in circles: motion of bacteria near solid boundaries. *Biophys J.* **90**:400–412, doi: 10.1529/biophysj.105.069401.
36. EIO: (1999). International Energy Outlook, Washington, DC, US Department of Energy, Energy Information Administration, DOE/EIA-0484.
37. EIO: (2008). International Energy Outlook, Washington, DC, US Department of Energy, Energy Information Administration, DOE/EIA-0484.
38. EPA, ESS method 150.1:chlorophyll – spectrophotometric. (http://www.epa.gov/greatlakes/lmmb/methods/methd150.pdf), date accessed: 01/10/2013.
39. Estrada, M. M., and E. Berdalet. 1997. Phytoplankton in a turbulent world. In: Marrase C, Siez E, Redondo JM, editors. *Lectures on plankton and turbulence. Sci Mar* 61 Supl. 1. p 125-140.
40. Fenchel, T. 2002. Microbial behaviour in a heterogenous world. *Science.* **296**:1068-1071, doi: 10.1126/science.1070118.
41. Folch, J., M. Lees, G. H. S. Stanley. 1957. A simple method for the isolation and purification of total lipids from animal tissues. *J. Biol. Chem*. **226**:497–509.
42. Foster, K. W., and R. D. Smyth. 1980. Light antennas in phototactic algae. *Microbiol. Rev*. **44**:572–630.

43. Fried, A., A. Tietz, A. Ben-Amotz, and W. Eichenberger. 1982. Lipid composition of the halotolerant alga *Dunaliella bardawil*. *Biochim. Biophys. Acta*. **713**:419–426, doi: 10.1016/0005-2760(82)90261-2.

44. Gibbs, N., and M. C. Duffus. 1976. Natural protoplast *Dunaliella* as a source of protein. *Appl. Environ. Microbiol*. **31**:602–604.

45. Gordillo, F. J. L., M. Goutx, F. L. Figueroa, and F. X. Niell. 1998. Effects of light intensity, CO_2 and nitrogen supply on lipid class composition of *Dunaliella viridis*. *J. Appl. Phycol.* **10**:135–144, doi: 10.1023/A:1008067022973.

46. Gouveia, L., and A. C. Oliveira. 2009. Microalgae as a raw material for biofuels production. *J. Ind. Microbiol. Biotechnol*. **36**:269-274, doi: 10.1007/s10295-008-0495-6.

47. Gray, J., and G. J. Hancock. 1955. The propulsion of sea urchin spermatozoa. *J. Exp. Biol.* **32**:802-814.

48. Griffiths, M. J., and S. T. L. Harrison. 2009. Lipid productivity as a key characteristic for choosing algal species for biodiesel production. *J. Appl. Phycol.* **21**:493–507, doi: 10.1007/s10811-008-9392-7.

49. Guasto, J. S., R. Rusconi, and R. Stocker. 2012. Fluid mechanics of planktonic microorganisms. *Ann. Rev. Fluid Mech.* **44**:373–400, doi: 10.1146/annurev-fluid-120710-101156.

50. Hadi, M. R., M. Shariati, and S. Afsharzadeh. 2008. Microalgal Biotechnology: Carotenoid and Glycerol Production by the Green Algae *Dunaliella* Isolated from the Gave-Khooni Salt Marsh, Iran. *Biotechnol. Bioprocess Eng*. **13**:540-544, doi: 10.1007/s12257-007-0185-7.

51. Haghjou, M. M., M. Shariati and N. Smirnoff. 2009. The effect of acute high light and low temperature stress on the ascorbate-glutathione cycle and superoxide dismutase activity in two *Dunaliella salina* strains. *Physiol. Plant.* **135**:272-280, doi: 10.1111/j.1399-3054.2008.01193.x.

52. Haider, Z., M. Hondzo, and F. Porte-Agel. 2005. Advective velocity and energy dissipation rate in an oscillatory flow. *Water Res.* **39**:2569–2578, doi: 10.1016/j.watres.2005.04.062.

53. Hansen, T. J., M. Hondzo, M. T. Mashek, D. G. Mashek, and P. A. Lefebvre. 2012. Algal swimming velocities signal fatty acid accumulation. *Biotechnol. Bioeng*. **110**:143–152, doi: 10.1002/bit.24619.

54. Hejazi, M. A., and R. H. Wijffels. 2003. Effect of light intensity on beta-carotene production and extraction by *Dunaliella salina* in two-phase bioreactors. *Biomol. Eng*. **20**:171–175, doi :10.1016/S1389-0344(03)00046-7.

55. Hieber, A. D., T. J. King, S. Morioka, L. H. Fukushima, A. A. Franke, and J. S. Bertram. 2000. Comparative effects of all-trans beta-carotene vs. 9-cis beta-carotene on carcinogen-induced neoplastic transformation and connexin 43 expression in murine 10T1/2 cells and on the differentiation of human keratinocytes. Nut. Cancer. **37**:234–244, doi: 10.1207/S15327914NC372_17.

56. Hill, J., O. Kalkanci, J. L. McMurry, and H. Koser. 2007. Hydrodynamic surface interactions enable *Escherichia Coli* to seek efficient routes to swim upstream. *Phys. Rev. Lett.* **98**:068101, doi: 10.1103/PhysRevLett.98.068101.

57. Hirsch, R.L., Bezdek, R., and R. Wendling. 2005. *Peaking of World Oil Production, Impacts, Mitigation and Risk Management*, National Energy Technology Laboratory, 2005.

58. Hondzo, M. 2012. Microbial and ecological fluid dynamics. In: Fernando HJ, editor. *Handbook of Environmental Fluid Dynamics*. CRC Press.

59. Hondzo, M., and A. Wüest. 2009. Do microscopic organisms feel turbulent flows?. *Environ. Sci. Technol*. **43**:764–768, doi: 10.1021/es801655p.

60. Hondzo, M., and T. A. Warnaars. 2008. Coupled effects of small-scale turbulence and phytoplankton biomass in a small-stratified lake. *J. Environ. Eng*. **134**:954–960, doi: 10.1061/(ASCE)0733-9372(2008)134:12(954).

61. Horwitz, A. R., and T. J. Parsons. 1999. Cell migration--movin'on. *Science*. 286:1102-1103, doi: 10.1126/science.286.5442.1102.

62. Hu, Q., M. Sommerfeld, E. Jarvis, M. Ghirardi, M. Posewitz, M. Seibert, and A. Darzins. 2008. Microalgal triacylglycerols as feedstocks for biofuel production: perspectives and advances. *Plant J.* **54**:621–639, doi: 10.1111/j.1365-313X.2008.03492.x.

63. Hwang, W., and J. K. Eaton. 2004. Creating homogeneous and isotropic turbulence without a mean flow. *Exp. Fluids*. **36**:444–454, doi: 10.1007/s00348-003-0742-6.

64. Ishikawa, T. 2009. Suspension biomechanics of swimming microbes. *J. R Soc. Interface.* 6:815-834, doi: 10.1098/rsif.2009.0223.

65. Jeffery, G. B. 1922. The Motion of Ellipsoidal Particles Immersed in a Viscous Fluid. *Proc. R. Soc. London.* **102**:161–179, doi: 10.1098/rspa.1922.0078.

66. Jiménez, J. 1997. Oceanic turbulence at millimeter scales. *Sci. Mar.* **61**:47–56, doi: 10.1175/JTECH1830.1.

67. Jin, E., and A. Melis. 2003. Microalgal biotechnology: Carotenoid production by the green algae *Dunaliella salina*. *Biotechnol. Bioproc. E.* **8**:331–337, doi: 10.1007/BF02949276.

68. Jones, M. S., L. Le Baron, and T. J. Pedley. 1994. Biflagellate gyrotaxis in a shear flow. *J. Fluid Mech.* 281:137–158.

69. Kessler, J. O. 1985. Hydrodynamic focusing of motile algal cells. *Nature.* **313**:218–220, doi: 10.1038/313218a0.

70. Khozin-Goldberg, I., and Z. Cohen. 2011. Unraveling algal lipid metabolism: Recent advances in gene identification. *Biochimie.* **93**:91–100, doi: 10.1016/j.biochi.2010.07.020.

71. Kim, J. H., J. A. Nemson, and A. Melis. 1993. Photosystem II reaction center damage and repair in *Dunaliella salina* (green alga): analysis under physiological and irradiance-stress conditions. *Plant Physiol*. **103**:181–189, doi: 10.1104/pp.103.1.181.

72. Kiørboe, T., and G. A. Jackson. 2001. Marine snow, organic solute plumes, and optimal chemosensory behavior of bacteria. *Limnol. Oceanogr*. **46**:1309-1318, doi: 10.4319/lo.2001.46.6.1309.

73. Koehl, M. A. R., P. A. Jumars and L. Karp-Boss. 2003. In: Norton AD, editor. *Out of the past*. *Brit. Phycol. Assoc*. Belfast, UK. p 115–130.

74. Lamers, P. P., M. Janssen, R. C. H. De Vos, R. J. Bino, and R. H. Wijffels. 2008. Exploring and exploiting carotenoid accumulation in *Dunaliella salina* for cell-

factory applications. *Trends Biotechnol*. **26**:631–638, doi: 10.1016/j.tibtech.2008.07.002.

75. Langlois, V. J., A. Andersen, T. Bohr, A. W. Visser, and T. Kiørboe. 2009. Significance of swimming and feeding currents for nutrient uptake in osmotrophic and interception feeding flagellates. *Aquat. Microb. Ecol*. **54**:35–44, doi: 10.3354/ame01253.
76. Lauga, E., and T. R. Powers. 2009. The hydrodynamics of swimming microorganisms. *Rep. Prog. Phys.* **72:**096601, doi: 10.1088/0034-4885/72/9/096601.
77. LeBlond, P. H., and L. A. Mysak. 1978. *Waves in the ocean.* Elsevier, Amsterdam, The Netherlands.
78. Loeblich, L. A. 1974. Action spectra and effect of light intensity on growth pigments and photosynthesis in *Dunaliella Salina*. J. Protozool. **21**:420-425.
79. Longhurst, A. R. 1991. Role of the Marine Biosphere in the Global Carbon Cycle. *Limnol. Oceanogr.* **36**:1507–1526.
80. Luznik, L., R. Gurka, W. A. M. Nimmo Smith, W. Zhu, J. Katz, T. R. Osborn. 2007. Distribution of energy spectra, Reynolds stresses, turbulence production and dissipation in a tidally driven bottom boundary layer. *J. Phys. Oceanogr.* **37:**1527–1550, doi: 10.1175/JPO3076.1.
81. Marcos, H. C. Fu, T. R. Powers and R. Stocker. 2012. *Proc. Natl. Acad. Sci. USA.* **109**:4780–4785, doi: 10.1073/pnas.1120955109.
82. Meinhart, C. D., S. T. Wereley, and J. G. Santiago. 1999. PIV measurements of a microchannel flow. *Exp Fluids.* **27**:414– 419.
83. Melkonian, M. 1982. The function analysis of the flagellar apparatus in green algae. *Symp. Soc. Exp. Biol.* **35:**589–606.
84. Miao, X.L., Q. Y. Wu, C. Y. Yang. 2004. Fast pyrolysis of microalgaeto produce renewable fuels. *J. Anal. Appl. Pyrolysis*. **71**:855–863, doi: 10.1016/j.jaap.2003.11.004.

85. Milledge, J. J., and S. Heaven. 2011. Disc stack centrifugation and separation and cell disruption of microalgae: A technical note. *Environ. Nat. Resour. Res*. **1**:17–24, doi: 10.5539/enrr.v1n1p17.

86. Mishra, A., A. Mandoli, and B. Jha. 2008. Physiological characterization and stress-induced metabolic responses of *Dunaliella salina* isolated from salt pan. J. Ind. Microbiol. Biotechnol. **35**:1093–1101, doi: 10.1007/s10295-008-0387-9.

87. Montgomery, J. C., C. F. Baker, and A. G. Carton. 1997. The lateral line can mediate rheotaxis in fish. *Nature.* **389**:960–963, doi: 10.1038/40135.

88. Musielak, M. M., L. Karp-Boss, P. A. Jumars, and L. J. Fauci. 2009. Nutrient transport and acquisition by diatom chains in a moving fluid. *J. Fluid Mech*. **638**: 401–421, doi:10.1017/S0022112009991108.

89. O'Connor, B. L., and M. Hondzo. 2008. Dissolved oxygen transfer to sediments by sweep and eject motions in aquatic environments. *Limnol. Oceanogr*. **53**:566–578, doi: 10.4319/lo.2008.53.2.0566.

90. O'Malley, S. 2011. *Bi-flagellate swimming dynamics.* PhD thesis, University of Glasgow, Scotland, UK.

91. Olmos, J., J. Paniagua, R. Contreras. 2000. Molecular identification of *Dunaliella sp.* utilizing the 18S rDNA gene. *Lett. Appl. Microbiol.* **30**:80–88.

92. Omoto, C. K., I. R. Gibbons, R. Kamiya, K. Takahashi C. Shingyoji, and G. B. Witman. 1999. Rotation of the central pair microtubules in eukaryotic flagella. *Mol. Biol. Cell*. **10**:1–4.

93. Pedley, T. J., and J. O. Kessler. 1992. Hydrodynamic Phenomena in Suspensions of Swimming Microorganisms. *Annu. Rev. Fluid. Mech.* **24:**313–358, doi: 10.1146/annurev.fl.24.010192.001525.

94. Peters, F., and C. Marrasé. 2000. Effects of turbulence on plankton: an overview of experimental evidence and some theoretical considerations. *Mar. Ecol. Prog. Ser.* **205**:291–306, doi:10.3354/meps205291.

95. Pienkos, P. T., and A. Darzins. 2009. The promise and challenges of microalgal-derived biofuels. Biofuels, Bioprod. Bioref. **3**:431–440, doi: 10.1002/bbb.159;

96. Pinton, J. F., and R. Labbe. 1994. Correction to Taylor hypothesis in swirling flows. *J. Phys. II France*. **4**:1461–1468, doi: 10.1051/jp2:1994211.

97. Polin, M., I. Tuval, K. Drescher, J. P. Gollub, and R. E. Goldstein. 2009. Chlamydomonas swims with two "gears" in a eukaryotic version of run-and-tumble locomotion. *Science*. **325**:487-490, doi : 10.1126/science.1172667.

98. Prairie, J. C., K. R. Sutherland, K. J. Nickols, and A. M. Kaltenberg. 2012. Biophysical interactions in the plankton: A cross-scale review. *Limnol. Oceanogr: Fluids & Environ.* **2**:121–145, doi 10.1215/21573689-1964713.

99. Preisig, H. R. 1992. Morphology and Taxonomy. In: Avron M, Ben-Amotz A, editor. *Dunaliella: Physiology, Biochemistry, and Biotechnology*. Florida: CRC Press. p 135-164.

100. Rafaı¨, S., L. Jibuti, P. Peyla. 2010. Effective viscosity of microswimmer suspensions. *Phys. Rev. Lett.* **105**:168102, doi: 10.1103/PhysRevLett.104.098102.

101. Raja, R., S. Hemaiswarya, R. Rengasamy. 2007. Exploitation of *Dunaliella* for β-carotene production. *Appl. Microbiol. Biotechnol*. **74**:517–523, doi: 10.1007/s00253-006-0777-8.

102. Saarenrinne, P., and M. Piirto. 2000. Turbulent kinetic energy dissipation rate estimation from PIV velocity vector fields. *Exp. Fluids.* **29**:S300–S307, doi: 10.1007/s003480070032.

103. Santiago, J. G., S. T. Wereley, C. D. Meinhart, D. J. Beebe, and R. J. Adrian. 1998. A particle image velocimetry system for microfluidics. *Exp. Fluids.* **25**:316–319, doi: 10.1007/s003480050235.

104. Schlagermann, P., G. Göttlicher, R. Dillschneider, R. Rosello-Sastre, and C. Posten. 2012. Composition of algal oil and its potential as biofuel. *J. Combust*. **2012**:1–14, doi: 10.1155/2012/285185.

105. Schlipalius, L. 1991. The extensive commercial cultivation of *Dunaliella salina*. *Bioresour. Technol.* **38**:241–243, doi: 10.1016/0960-8524(91)90162-D.

106. Schoevaert, D., S. Krishnaswamy, M. Couturier, and F. Marano. 1988. Ciliary beat and cell motility of *Dunaliella*: computer analysis of high speed

microcinematography. *Biol. Cell.* **62**:229–240, doi: 10.1111/j.1768-322X.1988.tb00725.x.

107. Schoevaert, D., S. Krishnaswamy, M. Couturier, and F. Marano. 1988. Ciliary beat and cell motility of *Dunaliella* computer analysis of high-speed microcinematography. *Biol. Cell*. **63**:229**–**240.
108. SCOR-UNESCO. 1966. Determination of photosynthetic pigments in seawater. Monographs on Oceanographic Methodology. 1: 11–18, Technical report. UNESCO, Paris.
109. Sheng, J., E. Malkiel, and J. Katz. 2006. Digital holographic microscope for measuring three-dimensional particle distributions and motions. *Appl. Opt.* **45**:3893–3901, doi: 10.1364/AO.45.003893.
110. Sheng, J., E. Malkiel, J. Katz, J. Adolf, and R. Belas. 2007. Digital holographic microscopy reveals prey-induced changes in swimming behavior of predatory dinoflagellates. *Proc. Natl. Acad. Sci.* **104**:17512-17517, doi: 10.1073/pnas.0704658104.
111. Sheng, J., E. Malkiel, and J. Katz. 2008. Using digital holographic microscopy for simultaneous measurements of 3D near wall velocity and wall shear stress in a turbulent boundary layer. *Exp. Fluids.* 45:1023–1035, doi: 10.1007%2Fs00348-008-0524-2.
112. Sheng, J., E. Malkiel, J. Katz, J. E. Adolf, and A. R. Place. 2010. A dinoflagellate exploits toxins to immobilize prey prior to ingestion. *Proc. Natl. Acad. Sci. USA.* **107**:2082–2087, doi: 10.1073/pnas.0912254107.
113. Singh, A., P. S. Nigam, and J. D. Murphy. 2011. Mechanism and challenges in commercialisation of algal biofuels. *Bioresour. Technol*. **102**:26–34, doi: 10.1016/j.biortech.2010.06.057.
114. Siron, R., G. Giusti, and B. Berland. 1989. Changes in the fatty acid composition of *Phaeodactylum tricornutum* and *Dunaliella tertiolecta* during growth and under phosphorus deficiency. *Mar. Ecol. Prog. Ser.* **55**: 95–100.

115. Stephens, E., I. L. Ross, Z. King, J. H. Mussgnug, O. Kruse, C. Posten, M. A. Borowitzka, and B. Hankamer. 2010. An economic and technical evaluation of microalgal biofuels. *Nat. Biotech*. **28**:126–128, doi: 10.1038/nbt0210-126.

116. Sullivan, J. M., E. Swift, P. L. Donaghay, and J. E. Rines. 2003. Small-scale turbulence affects the division rate and morphology of two red-tide dinoflagellates. *Harmful Algae*. **2**:183–199, doi:10.1016/S1568-9883(03)00039-8.

117. Taylor, G. I. 1921. Diffusion by continuous movements. *Proc. London Math. Soc.* **2**:196–212, doi: 10.1112/plms/s2-20.1.196.

118. Thakur, A., and H. D. Kumar. 1998. Glycerol production by *Dunaliella salina* in response to various combinations of organic carbon compounds. *Cytobios.* **93**:129-134.

119. Thakur, A., H. D. Kumar, S. M. Cowsik. 2000. Effect of pH and inorganic carbon concentration on growth, glycerol production, photosynthesis and dark respiration of *Dunaliella salina*. *Cytobios*. **102**:69–74.

120. Tompkins, J., M. M. DeVille. J. G. Day, and M. F. Turner. 1995. Culture Collection of Algae and Protozoa: Catalogue of strains. Kendal, UK: Titus Wilson and Sons Ltd. p 203.

121. Tornabene TG, Holzer G, Peterson SL. 1980. Lipid Profile of the Halophilic alga, *Dunaliella Salina*. Biochem. Biophys. Res. Comm. **96**:1349-1356, doi: 10.1016/0006-291X(80)90099-6.

122. Vanitha, A., M. S. Narayan, K. N. C. Murthy, G. A. Ravishankar. 2007. Comparative study of lipid composition of two halotolerant alga, *Dunaliella bardawil* and *Dunaliella salina*. *Int J Food Sci Nutr*. **58**:373-382, doi: 10.1080/09637480701252252.

123. Vismara, R., F. Verni, L. Barsanti, V. Evangelista, and P. Gualtieri. 2004. A short flagella mutant of *Dunaliella salina* (Chlorophyta, chlorophyceae). *Micron.* **35**:337–344, doi: 10.1016/j.micron.2004.01.001.

124. Warnaars, T. A., and M. Hondzo. 2006. Small-scale fluid motion mediates growth and nutrient uptake of *Selenastrum capricornutum*. Freshwater Biol. 51: 999–1015, doi: 10.1111/j.1365-2427.2006.01546.x.

125. Warnaars, T. A., M. Hondzo, and M. A. Carper. 2006. A desktop apparatus for studying interactions between microorganisms and small-scale fluid motion. *Hydrobiologia*. **563**:431-443, doi: 10.1007/s10750-006-0030-6.
126. Webster, D. R., A. Brathwaite, and J. Yen. 2004. A novel laboratory apparatus for simulating isotropic oceanic turbulence at low Reynolds number. *Limnol. Oceanogr. Methods*. **2**:1–12, doi: 10.4319/lom.2004.2.1.
127. Wijffels, R. H., and M. J. Barbosa. 2010. An outlook on microalgal biofuels. *Science*. **329**:796–799, doi: 10.1126/science.1189003.
128. Williams, P. J. L. B., and L. M. L. Laurens. 2010. Microalgae as biodiesel & biomass feedstocks: Review & analysis of the biochemistry, energetics & economics. *Energy. Environ. Sci*. **3**:554–590, doi: 10.1039/b924978h.
129. Zhu, Y. H., and J. G. Jiang. 2008. Continuous cultivation of *Dunaliella salina* in photobioreactor for the production of beta-carotene. *Euro. Food Res. Technol.* **227**:953-959, doi: 10.1007/s00217-007-0789-3.